Hydrogen, trace, and ultra-trace element distribution in natural olivines

Sylvie Demouchy, Olivier Alard

Hydrogen, trace, and ultra-trace element distribution in natural olivines

Sylvie DEMOUCHY[1,*] & Olivier ALARD[1,2]

[1]Géosciences Montpellier, Université de Montpellier & CNRS, 34095 Montpellier, France.

[2] Department of Earth and Planetary Science, Macquarie University, Sydney NSW 2109, Australia.

* Corresponding author: sylvie.demouchy@umontpellier.fr

Accepted to Contrib. Mineral. Petrol.

– March 2021 –

Cite as: **Demouchy S.** and Alard O. (2021) Hydrogen, minor, trace and ultra-trace elements distribution in natural olivines. Contrib. Mineral. Petrol. 176, 26, https://doi.org/10.1007/s00410-021-01778-5.

Abstract

We investigate the coupling between H, minor, trace, and ultra-trace element incorporations in 17 olivines from ten different locations covering various petrological origins: magmatic, hydrothermal and mantle-derived context. Concentrations in major element are determined by micro X-ray fluorescence. Minor, trace, and ultra-trace element are determined by laser ablation inductively coupled plasma mass spectrometry. Hydrogen concentrations are quantified using unpolarized and polarized Fourier transform infrared spectroscopy (FTIR). Forsterite contents (83.2 to 94.1 %) reflect the petrogenetic diversity. Hydrogen concentrations range from 0 to 54 ppm H_2O wt. Minor element concentrations (Ni + Mn) range from 3072 to 4333 ppm, and impurities are dominated by Ni, Mn, Ca or B. Total trace element concentrations range from 8.2 to 1473 ppm. Total rare Earth and extended ultra-trace elements concentrations are very low (< 0.5 ppm). Magmatic and hydrothermal olivines show the most and least amount of impurities, respectively, and mantle-derived olivines have concentrations between these two extremes. Combined with minor, trace, and ultra-trace element concentrations, the hydrogen concentrations and FTIR OH bands reflect the point defect diversity imposed by different geological settings. Hydrogen concentrations are inversely correlated with divalent impurities, indicating their competition for vacancies. However, a broad positive correlation is also found between OH bands at 3575 and 3525 cm^{-1} and Ti, confirming the existence of Ti-clinohumite-like point defect in mantle olivines. Nonetheless, Ti does not exclusively control hydrogen incorporation in olivine due to the co-existence with other mechanisms, and its effect appears diluted. Our results confirm that hydrogen behaves as a peculiar incompatible element, and furthermore as an opportunistic impurity in olivine.

Key words: Olivine, hydrogen, minor elements, trace elements, FTIR, LA-ICP-MS.

1. Introduction

Above absolute zero temperature, perfect minerals do not exist, all minerals contain assorted atomic-scale defects in various amounts, and mostly ionic vacancies. The concentration and mobility of these defects increases significantly with increasing temperature (e.g., Schmalzried, 1981; Philibert, 1995; Schwartz and Lang, 2016). Furthermore, the vacancies in olivine can incorporate a large range of atomic impurities covering the entire chemical classification from heavy (U, Th) to light elements (H, Li, He) in ppb- to ppm-level concentrations (e.g., Bell and Rossman 1992; Sykes et al. 1994; Ingrin and Skogby 2000; Kent and Rosmann 2002; Burnard et al. 2015; Tollan et al. 2018; Delon et al. 2018, 201; Bussweiler et al. 2019, Rasmussen et al., 2020). The atomic impurities are embedded in the crystalline structure of olivine following the substitution rules from Goldschmidt's (Goldschmidt 1926; Ringwood 1955; Kröger and Vink 1956), and more complex coupled substitutions can occur with increasing nonstoichiometry (e.g., Nakamura and Schmalzried 1983; Jurewicz and Watson 1988a, b; Berry et al., 2007a; Padrón-Navarta et al. 2014; Tollan et al. 2018). Olivine is the most depleted upper mantle mineral in trace elements, thus containing significantly less trace elements than in co-existing pyroxenes or garnets (e.g., Bodinier et al. 1987; Bodinier and Godard 2014; Satsukawa et al. 2017; Garrido et al. 2000), therefore olivine is not the most important trace element reservoir in the Earth's upper mantle. However, olivine is the most abundant (>60%) and the only interconnected mineral in the uppermost mantle, implying that its rheological properties control both the viscosity of lithospheric plates and the underlying convecting asthenosphere. As the viscosity of olivine-rich rock might decrease with increasing incorporation of impurities such as H, Fe or Ti (e.g., Mackwell et al. 1985; Mei and Kohlstedt 2000; Demouchy et al. 2012; Faul et al. 2016; Tielke et al. 2017), the mechanisms of hydrogen incorporation in olivine has been the focus of many experimental studies (e.g., Mackwell and Kohlstedt 1990; Bai and Kohlstedt 1992; Kohlstedt et al. 1996; Kohlstedt and Mackwell 1998;

Mosenfelder et al. 2006; Withers and Hirschmann 2008; Férot and Bolfan-Casanova 2012; Padrón-Navarta and Hermann 2017) for various thermodynamic conditions (e.g., pressure, temperature, $fO2$, fH_2O, $aSiO_2$, e.g., Kohlstedt et al. 1996; Gaetani et al. 2014) and chemical composition (e.g, Ti, Al, Cr, etc; Berry et al. 2007a, Tollan et al. 2019). The most recent experimental approaches include doping olivine with a high amount of atomic impurity before or synkinetic with hydration (e.g., Tollan et al. 2019). While these experiments highlight the individual mechanism of H incorporation, these results are not always directedly applicable to Earth's upper mantle.

The experiments on hydrogen incorporation were completed by studies of natural mantle-derived olivine specimens (e.g., Beran and Zemman 1983; Bell and Rossman 1992; Berry et al. 2005, 2007b; Beran and Libowitzky 2006; Skogby 2006; Peslier 2010; Demouchy and Bolfan-Casanova 2016; Xia et al. 2017) and several seminal publications have provided valuable spectral databases (Miller et al. 1987; Mosenfelder et al. 2006; G.R. Rossmann, http://minerals.gps.caltech.edu, or the PULI database, http://puli.mfgi.hu).

Despite these advances, data available on trace element incorporation in mantle-derived olivine are scarce and hinders our understanding and thus prediction ability on the mobility of trace elements in olivine (e.g., Demouchy et al. 2006; Mosenfelder et al. 2006; Padrón-Navarta et al. 2014; Thoraval and Demouchy 2014; Satsukawa et al. 2017; Thoraval et al. 2019). Indeed, the coupling of co-existing atomic impurities in olivine were often neglected, principally due to technical limitations (e.g., sample preparation and mass spectroscopy detection limits; see Batanova et al. 2015, 2019; Zhang et al. 2016; Bussweiler et al. 2019). However, recent analytical breakthroughs have sparked and renewed interest in coupled interactions between trace elements in olivine (e.g., De Hoog et al. 2010; Spandler and O'Neill 2010; Foley et al. 2013; Bussweiler et al. 2015; 2019; Veter et al. 2017; 2019; Neave et al. 2018). Here we assess the complex point defect diversity in natural olivines by characterizing the coexistence of

hydrogen with minor, trace, and ultra-trace elements. To explore a broad range of chemical compositions, we selected olivines from various geological settings.

2. Materials and Methods

2.1 Olivine specimens and sample preparation

We selected 17 single-crystal olivines from ten different geological settings; most specimens are from peridotite xenoliths that originated in the uppermost mantle (Table 1). Three samples (harzburgite SAS20, high temperature (HT) harzburgite SAS21, lherzolite SAS41) are spinel-bearing peridotites from Malaita (Ontong-Java Plateau; Demouchy et al. 2015) which contain olivines with low Al and different Ca contents. Samples SC and SC2018 are both San Carlos olivines (Arizona, USA), and LAZ is from Lanzarote (Canary Islands); they are all from spinel-bearing peridotites. DMP2 and DMP4 are olivines from spinel-bearing peridotites from Damaping (China). Specimen PA3 was extracted from a garnet-bearing lherzolite from Pali-Aike (Chile; Demouchy, 2004) and OLM is from a very coarse-granular peridotite from Olmani (Tanzania; OL10 from Baptiste et al. 2015). We have selected one magmatic olivine (LR) from La Réunion (Indian Ocean). SAP is a large hydrothermal gem-quality olivine from Sapat (Pakistan; see Göse et al. 2010), and samples HS and PP are from the same locality but were not produced by hydrothermal processes; they are of mantle origin. MYA is a hydrothermal olivine gem from Myanmar (Harlow et al. 2014). We completed the data set with two centimetric gem-quality crystals (NW1 and NW2) from a metamorphosed alpine-type peridotite massif in Norway; based on their chemical compositions, they are hydrothermal specimens from Sandvika (see Medaris 1984) or Almoklovdalen (see Kent and Rosmann 2002; Mosenfelder et al. 2006; Göse et al. 2008; their sample CIT15089 has Fo% =

93.51 – 93.76; Mosenfelder, person. comm. 14/01/2019). Samples NW1, NW2, SAP, and MYA result from hydrothermal recrystallization in dunitic domains.

Samples were optically inspected to discard crystal sections containing macroscopic and mesoscopic imperfections (e.g., spinel inclusions, lily pads, cracks, or milky or brownish zonations; e.g., Mosenfelder et al. 2006). Each olivine was then cut into a millimetric right prism with a rectangular base prior to *in-situ* chemical analyses. All faces of each prism were hand-polished using a polishing jig and diamond-lapping films with grit sizes ranging from 30 to 1 μm. The final prepared size of each olivine prism is reported in Table 1 and photographs are provided in Figure S1.

The distribution of major and a few minor elements were determined by micro X-ray fluorescence (μXRF), hydrogen concentrations by polarized and unpolarized Fourier-transform infrared spectroscopy (FTIR), and minor, trace/ultra-trace element concentrations by laser ablation inductively coupled plasma mass spectrometry (LA-ICP-MS). Since LA-ICP-MS is a destructive method, FTIR analyses were performed first, μXRF mapping second, and LA-ICP-MS last. The analytical procedures are detailed in the same order in the following subsections. The olivine crystals were free of any glue for FTIR analyses, then were fixed on a glass section with crystal bond for both μXRF and LA-ICP-MS measurements.

We emphasize that all analyses per sample were performed on the same olivine prism, and not on different olivine crystals co-existing in the same xenolith/hydrothermal vein, as commonly done in other studies. Past practices were constrained by analytical requirements and sample preparation and lead to none negligible scatter in the data. Our approach is designed to investigate consistently the control of olivine crystal chemistry on hydrogen incorporation.

2.2 Fourier-transform infrared spectroscopy

We analyzed hydroxyl groups in olivine using transmission FTIR spectroscopy at the Laboratoire Charles Coulomb (University of Montpellier, France). Unpolarized and polarized infrared spectra were acquired using a Bruker IFS66v equipped with a liquid nitrogen-cooled MCT detector (Mercatel alloy, HgCdTe), a KBr/Ge beam splitter, and coupled to a Bruker HYPERION microscope. The infrared beam was polarized with a KRS-5 polarizer (thallium-bromide-iodide) placed between the mid-IR source and the sample. Unpolarized IR measurements were performed following the protocol of Denis et al. (2015). Optically clean areas were chosen for analyses, and 256 scans were accumulated at a resolution of 4 cm^{-1} using a square aperture (100 × 100 μm). Each spectrum was baseline corrected and the absorbance normalized to 1 cm thickness. Each sample was washed several times in high purity acetone prior to FTIR analyses and placed on a CaF_2 plate when necessary (i.e., for the smallest samples). A minute amount of Fluorolube (ThermoScientific^{TM}) was used to eliminate thickness fringes if needed. The olivine prisms were not crystallographically oriented (except PA3). Still we acquired polarized and unpolarized FTIR spectra along three orthogonal directions, compiling two triplets of polarized spectra and one triplet of unpolarized spectra for each olivine prism (all spectra triplets are provided in supplementary material in Figure S2). Since NW1 and SAS20 olivine specimens were large, FTIR profile were also acquired and are provided in Figure S3.

Two types of IR calibrations were used to calculate hydrogen concentrations: the frequency-dependent calibration of Paterson (1982) and the mineral-dependent calibration for olivine of Withers et al. (2012). Hydrogen concentrations were calculated by integrating each spectrum over the 3620 – 3050 cm^{-1} wavenumber range. This calibration allows a detection limit of about 1 ppm of H_2O by weight (wt) for a 1mm-thick olivine sample, although the estimated error from the empirical calibration of Paterson (1982) is around 30 % of the resulting H concentration (e.g., Paterson 1982; Rauch 2000). Reported hydrogen concentrations are the

175 average of the three orthogonal unpolarized spectra or the three polarized spectra of each
176 orthogonal triplet from each olivine prism. Following the recommendations of Withers et al.
177 (2012) for unpolarized FTIR measurements of olivine, the maximum linear absorption of non-
178 normalized spectra did not exceed 0.3. Hydrogen concentrations are given in ppm H_2O wt., in
179 ppm of H (equals to molar concentration), and in $H/10^6Si$ to ease comparison with past studies.
180 Finally, the normalized integrated absorption area for use in future mineral-dependent IR
181 calibrations are provided in Table S1. Several spectra necessitated deconvolution to obtain the
182 integrated absorption area per peak. The best deconvolution results (i.e., the lowest residue
183 obtained for input peak positions as listed in Table 1 with ± 20 cm^{-1}, and using a gaussian
184 function) are provided in Figure S4 for samples LR, LAZ, PA3, SAS20 and SAS41.
185 Corresponding results of the deconvolution per mechanism of hydrogen incorporation (i.e.,
186 integrated normalized absorptions and relative % compare to bulk hydrogen) are compiled in
187 Table S2.
188
189 *2.3 X-ray fluorescence*
190 Major and minor element distributions within each olivine prism were measured by
191 μXRF at the Department of Earth and Planetary Sciences (Macquarie University, Australia)
192 using a Bruker M4 Tornado. Because μXRF does not require extensive sample preparation or
193 coating, this technique was preferred over electron microprobe measurements. Furthermore, the
194 polish quality required for FTIR analyses (final mirror polish with <0.5 μm grid) is more than
195 sufficient for such μXRF measurements. Analyses were performed at 50 kV and 200 μA under
196 low vacuum (18 mbar). To detect compositional variability, all maps were acquired over the
197 entire sample with spot and step sizes of 20 μm. Acquisition durations ranged from 4 to 32 min
198 depending on the size of the crystal. Twelve elements were analyzed: Si, Ti, Al, Cr, Fe, Mn,
199 Mg, Ca, Na, Ni, Co and Zn. To obtain quantitative estimates, the spectra were calibrated against

an in-house standard (SCO-2 San Carlos olivine). The μXRF data compare well (i.e., within errors) with electron microprobe measurements (see Table S3).

2.4 Laser ablation inductively coupled plasma mass spectrometry

Trace element analyses were performed on olivine samples by LA-ICP-MS at Macquarie GeoAnalytical (Department of Earth and Planetary Sciences, Macquarie University, Australia) using an Agilent 7700cs quadrupole ICP-MS system. The ICP-MS is coupled with an automated laser ablation platform (Analyte G2, Photon Teledyne) equipped with a 2-volume HelEx cell and housing an ArF 193 nm laser. Measurements were conducted in a He atmosphere (total He flow of ~0.8 L min^{-1}), which enhances sensitivity and reduces inter-element fractionation. Numerous studies have investigated the use of additional trace gases such as H_2, N_2, or CH_4 (e.g., Guillong and Heinrich 2007; Hu et al. 2008; Scheffler and Pozebon 2014). Here, our in-house experiments agree with Guillong and Heinrich (2007) that the addition of a few mL min^{-1} of H_2 (not N_2) increases the sensitivity for most elements by a factor of 2 to 4 (see also Veter et al. 2019). Thus, given the expected low trace element concentrations of olivine, 5 mL min^{-1} of H_2 was added to the central line (i.e., between the ablation cell and the plasma torch). The H-bearing He gas stream and particles from the sample were finally mixed with Ar (~0.90 ± 0.02 L min^{-1}) before entering the plasma with a final 30 mL mixed volume. Signals were measured in time-resolved acquisition mode and each analysis lasted 300 s, separated by 40 s pauses between analyses. Analysis times comprised 220 s for background (i.e., with the laser off), 60 s for mineral analysis (i.e., with the laser on), and 20 s for wash-out monitoring. The laser was fired at an energy density of 7.2 J cm^{-2}, a frequency of 10 Hz, and using a spot size of 110 μm. Oxide levels were kept to a minimum (below 1%) and were monitored using the ThO/Th ratio.

The reference glasses BHVO2-G and BCR2-G from the USGS and an in-house standard SCO-1 (San Carlos olivine) were included during analytical runs to minimize matrix effects (e.g., Bussweiler et al. 2019), and our measurements are within errors of the published values for these international reference materials (see Table S4, e.g., Jochum et al. 2005; Bussweiler et al. 2019). Elemental concentrations were calibrated against the glass standard NIST612 using the values compiled by Jochum et al. (2005). Data were subsequently reduced using the GLITTER software (Griffin et al. 2008) by carefully inspecting the time-resolved analyses to exclude heterogeneity in the analyzed volume. Silica content (SiO_2 wt.% as determined by μXRF) was used as an internal standard for both reference materials and olivine samples.

Local backgrounds were used instead of the interpolated or averaged session background. This yielded variable detection limits for the various analyses, which were occasionally either lower or higher than the typical detection limit; the best, worst, and typical detection limits are provided in Table S4 while standard deviations are given together with the LA-ICP-MS data. Reported trace and ultra-trace elemental concentrations in olivine correspond to averages of at least four ablations per olivine grain. All elements were measured in a single acquisition. Due to the formation of polyatomic interferences during LA-ICP-MS analysis, several isotopes were measured for key elements. Olivine matrices are rich in Mg and the formation of $^{25}Mg^{40}Ar$ overlaps with ^{65}Cu. Therefore, ^{63}Cu was used instead, given that ^{23}Na in olivine is only a trace element. Furthermore, the excess on mass 65 is used to correct the other Mg-argides on mass 64 and 66 corresponding to Zn. Similarly, the effect of oxide formation on ^{45}Sc ($^{16}O^{29}Si$, natural ^{29}Si abundance is ca 4.68%) is corrected by deconvolving the $^{44}M/^{43}M$ ratio ($^{44}M/^{43}M=(^{44}Ca+^{16}O^{28}Si)/^{43}Ca$, ^{27}Al is a trace element in olivine and thus is neglected, ^{28}Si natural abundance is *ca.* 92.23%) and subtracting the weighed excess from ^{45}M. The accuracy of these corrections is ultimately assessed against certified reference glasses (e.g.

BHVO2-G and BCR2-G) and the in-house SCO-1 olivine standard. The measured isotopes selected for this study are given in Table S4.

3. Results

We first present concentration and distribution of the major and minor elements, then hydrogen concentrations followed by the other trace and finally ultra-traces elements. The same color code is used throughout the set of figures and indicates the petrogenetic origin of the olivine specimens: hydrogen-rich hydrothermal olivine (SAP, NW1, NW2) in dark-blue; the hydrogen-poor hydrothermal olivine (MYA) in pale-blue; the magmatic olivine (LR) in black; dark-green for the garnet-bearing peridotitic olivine (PA3); high temperature spinel-bearing peridotitic olivine (SAS21) in brown-green, and at last the spinel-bearing peridotitic olivines (DMP2, DMP4, SC, SC2018, SAS41, SAS20, OLM, PP, HS1, LAZ) in bright green.

3.1 Major and minor element concentrations from X-ray fluorescence

Olivine major and a few minor element concentrations determined by μXRF are reported in Table 2. FeO contents range from 5.77 to a maximum 15.58 wt.% FeO in the magmatic olivine LR. Fo% (= 100 × (Mg/Mg+Fe) a.p.f.u.) range from 83.2 (LR) to 94.1% (MYA) as displayed in Figure 1. Nickel (0.23–0.47 wt.% NiO) and manganese contents (0.09–0.18 wt.% MnO) are typical for olivine. An additional compilation of typical Fo% vs NiO values are reported in Figure S5. Calcium concentrations range from 0.02 to 0.24 wt.% CaO.

NaO, TiO_2, Al_2O_3, and Cr_2O_3 contents are low, and fall mostly below the detection limits of the μXRF. Yet, μXRF permits rapid determination of potential spatial heterogeneous

major element concentrations before FTIR and LA-ICP-MS analyses. We did not observe any major or minor edge-to-edge zonings or micro-mineral inclusions or abnormal composition areas in the μXRF maps of the studied prisms of olivines.

3.2 FTIR spectra and hydrogen concentrations

Unpolarized spectra obtained on crystallographically unoriented olivines are shown in Figure 2. Additional polarized spectra acquired on the crystallographically oriented olivine PA3 are shown in Figure 3. The entire set of unpolarized and polarized FTIR spectra are given in Figure S2. The FTIR spectra display several OH bands of various intensities for only 11 of the 17 olivines analyzed; samples from San Carlos (SC and SC2018), Damaping (DMP2 and DMP4), and two of the gem olivines (HS and PP) are hydrogen-free. The wavenumbers of the OH bands are reported for each sample in Table 1 and as previously reported for iron-bearing olivines, for two ranges of wavenumbers (e.g., Miller et al. 1987; Kohlstedt et al. 1996; Göse et al. 2010; Demouchy and Bolfan-Casanova 2016; Thoraval et al. 2019). Range 1 includes wavenumbers between 3650 and 3500 cm^{-1} and Range 2 from 3500 to 3000 cm^{-1}. The polarized FTIR spectra of PA3 shown in Figure 3 are typical of garnet-bearing mantle peridotites (e.g., Miller et al., 1987).

Hydrogen concentrations derived from FTIR spectra are reported in Table 3. We report hydrogen concentrations determined using the calibration of Paterson (1982) for unpolarized IR spectra and using the more recent mineral-dependent calibration of Withers et al. (2012) for polarized IR spectra acquired along three orthogonal directions of the olivine prisms. The later discussion refers only to hydrogen concentrations obtained using polarized spectra and the calibration of Withers et al. (2012) ('[OH] po W' in Table 3). Hydrogen concentrations in hydrogen-bearing olivines range from 4 (LAZ) to 54 ppm H_2O wt (NW1), spanning a large

range of concentrations typical of olivines in off-craton settings (e.g., Ingrin and Skogby 2000; Peslier 2010; Demouchy and Bolfan-Casanova 2016). We also measured profiles, and they did not reveal special heterogeneous concentrations expect for PA3 (e.g., Figure S3), with very limited edge depletion after removal of the original grain rim as illustrated in Figure 4. This agrees with previous reports for olivine from this locality (Demouchy 2004; Demouchy et al. 2006).

Overall, and despite significant scatter, mantle olivines constitute a broad positive array of hydrogen concentrations as a function of Fo% shown in Figure 5. Hydrothermal MYA, NW1, and NW2 olivines have the highest Fo% (>93.6) but MYA has low hydrogen concentration (~6 ppm H_2O wt, respectively) despite its high Fo%. The high hydrogen concentrations observed at high Fo% contrast strongly with the H-free to low hydrogen concentrations (<10 ppm H_2O wt) of the low-Fo% (<90), which can be called "fertile" olivines (Fig. 5).

3.3 Minor, trace, and ultra-trace element concentrations

As the aim of this study is the decipher atomic impurities as extrinsic defect populations, we have chosen to sort and group the elements first by concentration level, and second by cationic valences.

LA-ICP-MS analyses permit the quantification of a large range of minor, trace, and ultra-trace element concentrations, reported in Table 4 (see Table S4 for detection limits), which vary enormously between 3306 ppm Ni (LAZ) down to 0.04 – 0.05 ppb (e.g., Tb in MYA or Th in DMP4, this is equivalent to $4 - 5 \times 10^{-11}$ g g^{-1}). Here we have considered that a *minor element* has a concentration above 1000 ppm, *trace elements* between 1000 and 10 ppm, and we introduce the *low trace elements* with concentrations between 10 and 0.1 ppm (i.e., two

orders of magnitude for each group) and finally below 0.1 ppm for the *ultra-trace elements*. Several elements have very variable concentrations in olivine (e.g., Al, between 0.9 and 224 ppm, Cu between 0.005 and 4.24 ppm), in agreement with the different petrogeneses. Furthermore, we have summarized in Table S5 the sorting and ranking of the element as a function of their abundance level, which is later used for the sum of concentrations displayed in Figure 6. The rare earth elements (REEs) in olivine all show concentrations below 0.1 ppm and are therefore here referred to as ultra-trace elements.

3.3.1 Minor elements

The only elements present at minor levels within the entire olivine set are Ni and Mn, their sum ranges from 3071 (NW1 and NW2) to 4333 ppm LAZ (Table 4). One sample has also a high Ca concentration (1437 ppm Ca in LR olivine). The sums of minor elements are inversely correlated with hydrogen concentrations (Figure 6a). Ni dominates the sum of the minor elements in each sample, followed by Mn (706 – 1390 ppm) and to some extent Ca (31 – 1437 ppm). Three olivines (NW1, NW2, and SAP) have high B concentrations with values between 61 and 110 ppm (Table 4), thus significantly higher than the relatively constant B concentrations of the other olivines (1.58 ± 0.50 ppm), but not reaching a minor element concentration level. These three relatively B-rich hydrothermal olivines are characterized by lower Ni (1697 – 2676 ppm) and Ca concentrations (30 – 40 ppm) than other olivines and have extremely low Al concentrations (<1 ppm).

The different petrological groups (color coded) are well recognized in Figure 6, but we can further define groups I, II, and III, notably in Figure 6b (i.e., area surrounded by the grey dashed lines). Group-I includes hydrogen-rich hydrothermal olivines (NW1, NW2, and SAP), and poor in minor elements. Group-II comprises the minor-element-rich olivines with moderate

348 to high H contents (PA3, SAS20, SAS21, and LR). Finally, group-III with the H-poor to H-free
349 olivines (DMP, OLM, LAZ, SC, and the H-poor hydrothermal olivine MYA).
350
351 *3.3.2 Trace, low-trace and ultra-trace elements*
352 LA-ICP-MS analyses yield elements at low (ppm level) to very low concentrations (ppb
353 level) in olivine (Table 4). The total combined concentration of trace, low trace and ultra-trace
354 impurities as a function of hydrogen concentration per sample ranges from 312 to 1496 ppm
355 (presented by level of concentration in Fig. 6b, c and d). There is an inverse relationship
356 between the sum of trace element and H concentration in olivine as illustrated in Fig. 6b, within
357 each group.
358 One can notice graphically that groups-I and II are in prolongation of each other and
359 that group III is shifted down in H concentration compared to groups I and II. The low-H
360 hydrothermal olivine (MYA) also aligns with the sp-lherzolite olivine of group III. The olivine
361 most enriched in trace elements is magmatic olivine LR (Table 4), and those with the lowest
362 trace element contents are the hydrothermal samples (SAP, NW1, NW2, MYA). The groups I,
363 II and III are further confirmed by trace to trace element concentrations (H excluded, B versus
364 Li, Cr versus B; Ti versus Cr/Na; Ti versus V; Cr versus V, Cr versus Al, Li versus P) as
365 illustrated in Figures S6 and S7.
366 The total concentration of ultra-trace impurities per sample ranges from 0.07 to 0.45
367 ppm (Table 4) and are shown in Figure 6d. While we previously identified three groups (I, II,
368 and III), the REE concentrations for all samples are extremely low and the distribution
369 according to those groups is not as clear as in Fig. 6b; the sum of REE contents per sample
370 varies between 4 and 140 ppb (Table 4). However, if the four hydrothermal B-rich olivines and
371 the magmatic olivine LR are discarded, this range is reduced to 4 - 31 ppb. Although MYA
372 (highest Fo% = 94.11) shows the lowest REE content and $(Yb)_{PM}$ value (here, the subscript

373 'PM' indicating normalization to the primitive mantle value; McDonough and Sun, 1995).
374 Overall, the summed REE concentrations in the olivines appear uncorrelated to Fo% and other
375 divalent impurities.

376 REE patterns and Th concentrations are reported normalized to primitive mantle values
377 (McDonough and Sun, 1995) in Figure 7. Except for four samples, the olivine REE patterns are
378 broadly similar. These four exceptions are the three H-rich hydrothermal olivines (NW1, NW2,
379 SAP) and the magmatic olivine LR. These peculiar olivines are characterized by much higher
380 heavy-REE contents ($(Yb)_{PM}$ = 0.16 for SAP) than the other olivines (e.g., $(Yb)_{PM}$ = 0.011 for
381 SC2018). Furthermore, the REE patterns of SAP and LAZ are similar in shape, i.e., less
382 depleted in light-REEs (Ce/Yb = 0.778 for LAZ) than the other olivines (on average, Ce/Yb =
383 0.085 ± 0.090). The remaining olivines have REE patterns characterized by a steady, negatively
384 sloped heavy-REEs to middle REE patterns $(Yb/Gd)_{PM}$ = 0.81) and enrichments of Th and La
385 relative to Ce ($(La/Ce)_{PM}$ = 0.387 for SC2018). Large ion lithophile elements (LILEs: Sr, Rb,
386 Ba, U), Ce, and Th show relatively similar patterns and abundances in all olivines, including
387 the four anomalous specimens mentioned above. For instance, U contents are relatively high
388 ($(U/Th)_{PM} > 1$), whereas Rb is systematically enriched relative to Ba ((Rb/Ba) > 1.4 for SAS20).
389 All olivines show negative Sr anomalies relative to Pr or Nd. The behavior of high field strength
390 elements (HFSEs: Ti, Zr, Hf, Nb, Ta) relative to the REEs is much more variable. Overall,
391 HFSEs do not form negative anomalies relative to their neighboring REEs, except occasionally
392 for Zr, and either follow the continuity of the REE pattern or produce marked positive
393 anomalies. Although REEs occur in very low concentrations in olivine, hydrogen is not as
394 depleted as La and Ce. Also seen in Figure 7, the ultra-trace element patterns of mantle-derived
395 olivines (i.e., excluding those of hydrothermal and magmatic origins) are quite similar among
396 the analyzed specimens, and are mostly irrespective of petrological contexts (e.g., melting and
397 metasomatic indexes). The relative consistency of ultra-trace element concentrations and

fractionations in olivine, whatever the geological setting and trace element concentration of the coexisting phases (e.g., pyroxenes), have been previously observed by Bedini and Bodinier (1999) and Garrido et al. (2000). Our results further confirm that the incorporation of these elements (REEs, HFSEs, ± LILEs) into mantle olivine is governed by olivine crystallography. Thus, incorporation is limited by vacancy population and concentrations, and not by the chemical compositions of coexisting phases or past percolating melts and fluids.

3.4 Distribution by valence and relationship with H

Point defect theory accounts for mass conservation, the respect of crystallography (i.e., site balance) and electroneutrality (i.e., charge balance) to minimize defect energy. Therefore, atomic impurities are 'aware' of each other and should further be decrypted as a function of their valence. In the past, mechanisms of hydrogen incorporation were successfully decrypted as a function of the occupied vacancies (V), which is limited to V_{Si}'''' and V_{Mg}'' (using Kröger-Vink notation, Kröger and Vink, 1956), and to possible mere interstitial proton ($h_i^{\cdot}$). In addition, two mechanisms of coupled (or associated) point defect were identified between trivalent and hydrogen (e.g., Fe^{3+}, Cr^{3+}, Mackwell and Kohlstedt 1990; Tollan et al. 2018) and between titanium and hydrogen (the so call Ti-clinohumite-like point defect, e.g., Berry et al. 2005). The established hydrogenated point defect and their matching IR bands are already given in Table 1. Occupancies of H in V_{Si}'''' is attributed to IR bands at 3598, 3562, 3542, and 3485 cm^{-1}, without information on the number of H inside the tetrahedron. Occupancies of H in V_{Mg}'' is attributed to 3230 cm^{-1}, again without information on the number of H inside the octahedron (e.g., Berry et al., 2007). Hydrogen coupled to trivalent impurities yields IR bands at 3355 and 3327 cm^{-1} (e.g., Berry et al. 2007, Blanchard et al. 2017; Tollan et al. 2018). At last, hydrogen in V_{Si}'''' balanced by Ti in V_{Mg}'' yields IR bands at 3572 and 3525 cm^{-1}. Therefore, hydrogen

mechanisms of incorporation can be inferred by 'reading' an infrared spectrum with this framework of four mechanisms. Nevertheless, in the experimental studies, hydrogenation under water saturation was preceded by doping of the olivine lattice with large amount of one type of atomic impurity (Berry et al. 2005, 2007, Padrón-Navarta et al. 2014) and for a given restricted set of thermodynamic conditions (fO_2, fH_2O, $aSiO_2$), which is not necessarily relevant for the entire upper mantle but for a specific context only (e.g., for subduction, Padròn-Navarta and Hermann, 2017).

Below we report the distribution of hydrogen as a function of the valence of co-existing impurities for concentration levels found in natural olivine specimens. From now on, element concentrations are presented in molar concentration (in micromol/g) to better assess associated point defects. The sum of monovalent, divalent, trivalent, tetravalent and pentavalent as a function of hydrogen concentration in ppm of hydrogen by weight are also provided in Figure S8.

Monovalent distribution is dominated by Li and Na, they are presented individually and as a sum in Figure 8. No major Li variation as a function of hydrogen is observed in most of the olivines, except for the hydrogen-rich hydrothermal samples (NW1 or NW2), which display high Li and low Na concentrations. In the contrary, Na distribution is more variable from very poor (0.08 ppm Na in NW2) to high (58.1 ppm Na in LR and 63.7 ppm Na in PA3).

Divalent distribution is dominated by Ni, Mn, Ca and was already identified in Figure 6a and 6b. Since the concentration level of Ni is very high compared to other divalent impurities, the negative correlation observed on Figure 6a is not perturbated by the addition of other metal-like divalent impurities. However, if nickel is excluded, the sum of divalent elements is not strikingly negatively correlated (Fig. S8).

The sum of trace trivalent distribution (B, Al, Cr, Sc and V) is very different if we compare the hydrothermal olivines from the others olivines as shown in Figure 9. The mantle

olivines and LR olivine are presented together in Figure 9a and b and the hydrothermal olivines in Figure 9c. If the IR bands attributed to hydrogen - trivalent complex defects (3355 and 3327 cm^{-1}) are only considered, the mantle-derived olivines display a positive correlation ($R^2 = 0.83$). A similar distribution is observed for most of the trivalent impurities, including the sum of REEs as shown in Figure 9b. Note that B (1.16 – 2.18 ppm or 0.11 – 0.2 micromol/g) and Sc (5.83 – 9.5 ppm or 0.13 – 0.21 micromol/g) do not show such a clear relationship, as they have a limited range of concentrations when compared to other trivalent elements (one or more order of magnitude for Cr, Al and V). The magmatic olivine (LR) is singled out by its high concentration in trivalent elements, which was also observed for the other atomic impurities.

The sum of the concentration of main trivalent elements (B+Al+Sc+Cr+V) as a function of bulk hydrogen concentration for the hydrothermal olivines is shown in Figure 9c and displays positive correlation ($R^2 = 0.98$), which is also visible if only B is considered, even if the correlation is not as good as for the sum of trivalent elements. For the hydrothermal olivines, the mechanism of coupling is likely to involve B siting into V_{Si}'''' and two H in V_{Mg}'' as previously suggested by Sykes and Rossmann (1994) to lead to $\{2H_{Mg}^{\times}B_{Si}'O_O^{\times}\}'$ complex defect, but which is not electronically balanced. It can also lead to a simplified defect suggested by e.g., Christ (1965) with $\{2Mg_{Mg}^{\times}B_{Si}'(OH)_O^{\cdot}\}^{\times}$ even if the complete substitution (for every Si atomic) is not realistic in these olivines. Unfortunately, our hydrothermal olivines do not permit to make a distinction between these two different complex point defects.

Lastly, the quantification of Fe^{3+} in olivine remains a true challenge (below Mössbauer spectroscopy detection limits, e.g., 100 ppm e.g., Duba et al. 1973), and we could regrettably not discuss the distribution of Fe^{3+} as a function of hydrogen in this study.

Tetravalent impurities, and in particular Ti, were the subject of specific attention as Ti is responsible for the striking high intensity bands at 3575 and 3525 cm^{-1} (e.g., Berry et al. 2005), in a majority of mantle-derived olivines (Fig. 2). The titanium clinohumite-like point

defect is defined as a Ti^{4+} ion occupying a Mg vacancy and two H^+ ions occupying a Si vacancy (Berry et al. 2005, 2007b; Walker et al. 2007; Padrón-Navarta et al. 2014; Padrón-Navarta and Hermann 2017). It is noted $\{Ti_{Mg}^{\cdot\cdot}(2H)_{Si}''O_O^{\times}\}^{\times}$ in Kröger-Vink notation or abbreviated as [Ti-2H]. Nevertheless, for our data set there is no striking positive correlation between the bulk mineral hydrogen concentration and Ti concentrations in the studied olivines (Fig. S8). Only six of the analyzed olivine samples (OLM, SAS20, SAS41, Pa3, LR and LAZ, see Table 1) displayed the typical OH bands attributed to the [Ti-2H] defect (3575 and 3525 cm^{-1}). However, if we only consider the hydrogen associated with these IR bands, a slightly positive correlation is seen in Figure 10a (R^2=0.65) (i.e., deconvolution results are given in Fig. S4; integrated normalized absorptions and % relative to bulk hydrogen concentrations are detailed in Table S2). We added in Figure 10b typical Ti range of concentrations reported in mantle-derived olivines (see also Fig. 2 in Foley et al., 2013). We compare our results with FTIR results from doping experiments (Faul et al. 2016; Padròn-Navarta and Hermann 2017, Tollan et al. 2018) and from mantle-derived olivines (Schmaedicke et al. 2013; Demouchy et al. 2015; Denis et al. 2018), which were all reprocessed accordingly to the methodology used here to obtain the normalized integrated absorbance for the [Ti-2H] defect only. We converted the concentration in micromole/g to better evaluate the potential coupling between hydrogen and titanium in Figure 10c. The results are far from the expected 1:2 line (at saturation), but closer to a 1:1 coupling. Note that error bars from Padròn-Navarta et al. (2014) are very large since titanium concentrations were obtained by electron microprobe and not LA-ICP-MS; We also wish to point out the non-negligible impact of the choice of the IR calibration (Bell et al. 2003 versus Withers et al. 2012) as illustrated by Figure 10c. We reiterate that such a positive correlation does not hold when considering the bulk (total) hydrogen contents. This discrepancy shows that even if the [Ti-2H] defect is a significant mechanism for hydrogen incorporation in mantle olivine, it is not dominant enough to overcome the other mechanisms (see Table S2). We thus

conclude that the diversity of hydrogen-decorated point defects dilutes the effect of complex defect with Ti.

To assess how our olivines match current Ti data, we further compare our results with mantle and magmatic compositions from the literature for Ti and Ca in Figure 11 as these trace elements are commonly used together as a petrogenetic indicator (e.g., O'Reilly et al., 1997; Foley et al., 2013). This figure demonstrates that mantle-derived olivines have low Ti (<100 ppm) and Ca concentrations (<1000 ppm). Conversely, Ti- and Ca-rich compositions are typical of magmatic olivines (e.g., sample LR). Hence, Figure 11 provides a framework for further doping experiments to properly assess the potential impact of non-divalent minor elements such as Ti when co-existing with various divalent cations (e.g., Ni, Ca, Mn) in lithospheric olivines.

The most abundant pentavalent impurity (phosphorous, Fig. S8d) has a similar concentration level to monovalent and titanium, but a distribution similar to trivalent elements, except for the high temperature (HT) harzburgitic olivine, which is one of the poorest olivine in P.

4. Discussion

4.1 Potential impact of hydrogen loss

Only one of the selected olivine samples originally displays a heterogeneous hydrogen distribution (PA3, Fig. 4), which was interpreted as resulting from partial dehydration by diffusion during magma ascent towards the surface (Demouchy et al. 2006). Other studies have reported similar dehydration profiles in olivines and pyroxenes (Peslier and Luhr 2006; Wade et al. 2008; Lloyd et al. 2012, 2017; Denis et al. 2013; Peslier et al. 2015; Tian et al. 2017; Denis et al. 2018). However, after more than a decade, we must face the paucity of olivines and

pyroxenes presenting such heterogeneous hydrogen distributions, which are also never coupled with other minor/trace element spatial heterogeneities. Furthermore, despite the fast hydrogen diffusivities obtained experimentally (Mackwell and Kohlstedt 1990; Demouchy and Mackwell 2006), natural olivine crystals ubiquitously contain remnant traces of hydrogen. In this study, we assume that the remnant hydrogen accurately represents the energetically favorable long-term hydrogen-decorated point defects and their diversity. We emphasize that additional hydrogen-decorated defects may be present in the olivine lattice at depth, but not preserved during magma ascent (e.g., Kempf and Hermman 2018; Tollan et al. 2018), hence we do not consider them as reliable long-term mechanisms of hydrogen storage.

4.2 Effects of temperature and pressure

Because the incorporation of minor elements in mantle minerals is a function of thermodynamic parameters (mostly temperature, pressure, and possibly oxygen fugacity) several minor elements have been used as reliable geothermobarometers to estimate equilibrium conditions in upper mantle rocks. For example, Ca exchange between ortho- and clino-pyroxene or Ca in orthopyroxene (Ca-in-opx) is a function of temperature (e.g., Wells 1977; Boyd and Nixon 1978; Ellis and Green 1979; Brey and Kohler 1990) and aluminum incorporation in olivine or pyroxene is a function of pressure (e.g., Stalder 2004; Férot and Bolfan-Casanova 2012; Coogan et al. 2014; Bussweiler et al. 2017; D'Souza et al. 2020). In particular, the Ca-in-opx geothermometer (Brey and Kohler 1990) has been widely used to constrain the equilibrium temperature of mantle xenoliths (based on the fact that Ca concentration increases in orthopyroxenes and decreases in olivine with increasing temperature; e.g., O'Reilly et al. 1997), and to help constrain the pressure/depth of origin. Nevertheless, the uncertainties on pressure remains most of the time very high for spinel-bearing peridotites (± 1 GPa and ± 100 °C; Brey and Kohler 1990). Nonetheless, in the absence of a better (absolute)

548 geothermobarometer, its usage quickly became the norm until recently (e.g., Wan et al. 2008;
549 Bussweiler et al. 2017; D'Souza et al. 2020). Combined with this geothermobarometer, the
550 maximum and minimum hydrogen concentrations in mantle-derived olivines display a striking
551 increase with increasing temperature as seen along a geotherm (Costa et al. 2010; Peslier et al.
552 2010; Demouchy and Bolfan-Casanova 2016; Peslier et al. 2017). This agrees with the
553 experimentally-determined control of water fugacity on hydrogen incorporation with increasing
554 pressure under water-saturation (Kohlstedt et al. 1996; Hirschmann et al. 2005; Mosenfelder et
555 al. 2006; Bali et al. 2008; Férot and Bolfan-Casanova 2012; Gaetani et al. 2014; Padrón-Navarta
556 and Hermann 2017). However, in naturally hydrated mantle olivines, this positive correlation
557 might not be that straightforward and could be indirect. Here, we examine the possible
558 correlation between hydrogen and Ca concentrations from this study and from mantle-derived
559 olivines in Figure 12 (Demouchy 2004; Moselfelder et al. 2006; Grant et al. 2007; Falus et al.
560 2008; Li et al. 2008; Yang et al. 2008; Peslier et al. 2010, 2012; Denis et al. 2013, 2015, 2018;
561 Soustelle et al. 2013; Demouchy et al. 2015, 2019; Satsukawa et al. 2017). Hydrogen
562 concentration broadly increases with decreasing Ca concentration in olivine in group III
563 confirming that the two species compete for M-site vacancies with increasing temperature (or
564 depth). The three hydrothermal olivines of Group I do not show the same trend. The olivines
565 from Group II do not show a well-defined correlation as for group III, and the horizontal spread
566 is dragged by the composition of the magmatic olivine LR. We recall here that magmatic
567 olivines (e.g. LR) are highly defective as the Fe-enrichment, resulting from crystallization in a
568 Fe-rich magma, enhances nonstoichiometry (e.g, Nakamura and Schmalzried 1983), thus
569 vacancy concentration, and consequently incorporation of atomic impurities such as Ca is easier.
570 Nevertheless, if the magma is far to be water-undersaturated (e.g., water-fugacity is low at
571 shallow depth), it cannot lead to a concomitant high incorporation of hydrogen, thus hydrogen
572 will be at odd with the other atomic impurities in magmatic olivines. To resume, while

573 magmatic olivines will have a high capacity to host H, ultimately the concentration of H in
574 these same olivines will depend on the water fugacity in the magmatic system.
575
576 *4.3 Co-existence of complex hydrogenated point defects*
577 The identification of a dominant and unique mechanism of hydrogen incorporation in
578 olivine relevant to Earth's mantle conditions has been the subject of important consideration.
579 Early experimental studies established the important role of M-site vacancies in hydrogen
580 incorporation (Beran and Putnis 1983; Kohlstedt et al. 1996; Bali et al. 2008; Férot and Bolfan-
581 Casanova 2012; Gaetani et al. 2014). Experimental studies have now clearly documented
582 increased hydrogen incorporation in minor- and trace-element-doped crystals. Furthermore, the
583 strategic role of Ti and its association with H incorporation into Si vacancies (the titanium
584 clinohumite-like point defect) is now well established. Here, the Figures 2, 6a, 9, 10 and Table
585 S4 clearly show that the integrated OH bands for [Ti-2H] are the most intense OH bands in
586 FTIR spectra for mantle olivines. Despite this, integrated OH bands for [Ti-2H] do not
587 exclusively control the bulk H concentration and thus cannot be used a distinctive proxy for the
588 bulk hydrogen concentration in olivine for water under-saturated conditions compared to the
589 three other mechanisms of hydrogen incorporation (V_{Si}'''', V_{Mg}'' and coupling with trivalent
590 impurities). Nevertheless, the sum of the hydrogen concentration linked to the four mechanisms
591 of incorporation seem to hold true as shown in Figure 13. Indeed, excluding three olivines from
592 group II (magmatic LR, garnet-bearing lherzolite and the HT harzburgite), olivine forms a
593 linear positive correlation parallel to the 1:1 line. Furthermore, if we take into consideration the
594 entire population of atomic impurities in mole per gram of olivine the sum of trivalent
595 impurities (B+Al+Cr+Sc+V= 1.14 to 17.2 μmol/g) dominates the sum of monovalent
596 (H+Li+Na =1.07 to 6.86 micromol/g), which is above pentavalent (e.g., phosphorous, 0.35 to
597 2.31 micromol/g) and the most abundant tetravalents elements (Ti+Ge = 0.09 to 1.14) as shown

598 in Figure S9. Then, hydrogen would mostly likely form complex associate-defect with trivalent
599 in natural olivines.
600
601

602 5. Conclusions

603 The incorporation of minor, trace, and ultra-trace elements into atomic-scale defects has
604 been used as a petrogenetic indicator of magmatic and mantle processes (e.g., Foley et al. 2013).
605 Here, based on our study of olivine crystals from ten different geological localities, we draw
606 the following conclusions. (1) The diversity of hydrogen-decorated point defects is associated
607 with a large range of minor and trace elements. Nevertheless, no single impurity seems to
608 control the bulk incorporation of hydrogen in olivine. Furthermore, the effect of titanium
609 clinohumite-like point defects appears diluted once bulk hydrogen concentrations are
610 considered in mantle-derived olivines. (2) Incorporation of these elements (REEs, HFSEs, ±
611 LILEs) into mantle olivine appears to be governed by olivine crystallography. This is limited
612 by vacancy population and concentrations for a given temperature, and not by the chemical
613 compositions of coexisting phases or percolating melts and fluids. (3) Although REEs occur in
614 very low concentrations in olivine, olivine is not as depleted in H as in La and Ce, probably due
615 to difference in their valence.

616 The geochemical affinity of hydrogen appears inconsistent, a peculiarity which is
617 probably related to its small ionic radius, the increasing vacancy population in olivine with
618 increasing temperature (and then depth), the diversity of complex defects, and the very fast
619 diffusivity of hydrogen in olivine relative to other minor/trace elements (e.g., fast to reach new
620 equilibrium). This observed behavior could be explained by a late incorporation of hydrogen
621 into olivine, with hydrogen filling all persisting vacancies in the olivine lattice (e.g., post-partial
622 melting, post-metasomatism). Thus, H is offered a large range of sites of storage, and can be

categorized as a versatile and opportunistic atom; H can be seen as a cuckoo element using whatever atomic spaces which remain available.

As a consequence, targeting a single controlling mechanism of hydrogen incorporation into olivine using natural specimens might be in vain. Solubility laws based on high-pressure and high-temperature effects seem to remain the best approach, despite an inclination toward over-doped and over-simplified incorporations of atomic impurities in experimental charges. Furthermore, in 'cold' geological domains (e.g., subducted slabs, crustal and metamorphic settings), the mechanisms of hydrogen incorporation might be overall different and more complex than in mantle-derived contexts. This necessitates new and complex experimental approaches to understand the role of co-existing atomic impurities in the mechanisms of hydrogen incorporation and mobility in olivine as a function of the miscellaneous sites of storage.

Acknowledgements

CNRS supported this study through INSU Tellus program 2019 awarded to S. Demouchy and a Future Fellowship (FT150100115) from Australian Research Council awarded to O. Alard. The authors thank Dr. D. Mainprice and Dr. A. Ishikawa for the re-use of selected olivine crystals. S.D. thanks J.-A. Padròn-Navarta and C. Thoraval for constructive discussions, Dr. T.D. Murphy and Dr. Y. Gréau at Macquarie University for their help and precious time on the Bruker M4 Tornado and L. Gorojovsky who improved the spelling and grammar of this manuscript. The IR-Raman technological Platform of University of Montpellier is acknowledged for the vibrational experiments. This is publication XXX of CCFS - Macquarie University.

Availability of data and material

All raw data are available upon request to the corresponding author.

References

Aines R. D. and Rossman G. R. (1984) Water in minerals? A peak in the infrared. *J. Geophys. Res.* **89** (B6), 4059–4071.

Bai Q. and Kohlstedt D. L. (1992) Substantial hydrogen solubility in olivine and implications for water storage in the mantle. *Nature* **357**, 672–674.

Bali E., Bolfan-Casanova N. and Koga, K. (2008) Pressure and temperature dependence of H solubility in forsterite: an implication to water activity in the Earth interior. *Earth Planet. Sci. Lett.* **268**, 354–363.

Baptiste V., Tommasi A., Vauchez A., Demouchy S. and Rudnick, R.L., (2015) Deformation, hydration, and anisotropy of the lithospheric mantle in an active rift: constraints from mantle xenoliths from the North Tanzanian Divergence of the East African Rift. *Tectonophysics* **639**, 34–55.

Basch V., Rampone E., Crispini L., Ferrando C., Ildefonse, B. and Godard, M., (2018). From mantle peridotites to hybrid troctolites: Textural and chemical evolution during melt-rock interaction history (Mt. Maggiore, Corsica, France). *Lithos* **323**, 4–23. doi:10.1016/j.lithos.2018.02.025

Batanova V.G., Sobolev A.V. and Kuzmin D.V., (2015) Trace element analysis of olivine: High precision analytical method for JEOL JXA-8230 electron probe microanalyser, *Chem. Geol*. **419**, 149-157.

Batanova, V.G., Thompson, J.M., Danyushevsky, L.V., Portnyagin, M.V., Garbe Schönberg, D., Hauri, E., Kimura, J.I., Chang, Q., Senda, R., Goemann, K., Chauvel, C., Campillo, S., Ionov, D.A. and Sobolev, A.V. (2019). New Olivine Reference Material for In SituMicroanalysis. *Geostand Geoanal Res* **419**, 149–21. doi:10.1111/ggr.12266

Bell D.R. and Rossman G.R., (1992) Water in Earth's mantle: The role of nominally anhydrous minerals. *Science* **255**, 1391–1397.

674 Bell D.R., Rossman G.R., Maldener J., Endisch D. and Rauch, F. (2003) Hydroxide in olivine: a
675 quantitative determination of the absolute amount and calibration of the IR spectrum. *J.*
676 *Geophys. Res.* **108**.
677 Bell D.R., Rossman G.R., and Moore R.O. (2004) Abundance and Partitioning of OH in a High-
678 pressure Magmatic System: Megacrysts from the Monastery Kimberlite, South Africa. *J. Petrol*
679 **45**, 1539–1564.
680 Bedini M.R. and Bodinier J.L., 1999. Distribution of incompatible trace elements between the
681 constituents of spinel peridotite xenoliths: ICP-MS data from the East African Rift. *Geochim.*
682 *Cosmochim. Acta* **63**, 3883–3900.
683 Beran A. and Libowitzky E. (2006) Water in Natural Mantle Minerals II: Olivine, Garnet and
684 Accessory Minerals. *Reviews in Mineralogy and Geochemistry* **62**, 169–191.
685 Beran A. and Putnis A., (1983) A model of the OH position in olivine, derived from infrared-
686 spectroscopy investigations. *Phys. Chem. Min.* **9**, 57–60.
687 Beran A. and Zemman J., (1969) Üder OH-gruppen in Olivin. *Österreich Akademie des*
688 *Wissenschaften* **3**, 73–74.
689 Berry A., Hermann, J., O'Neill, H.S.C. and Foran G.J., (2005) Fringerprinting the water site in mantle
690 olivine. *Geology* **33**, 869–872.
691 Berry A., O'Neill H.S. Hermann and J., Scott, D.R., (2007a) The infrared signature of water associated
692 with trivalent cations in olivine. *Earth Planet. Sci. Lett.* **1-2**, 134–142.
693 Berry A., Walker A.M. ,Hermann J., O'Neill H.S., Foran, G.J. and Gale, J., (2007b) Titanium
694 substitution mechanisms in forsterite. *Chem. Geol.* **242**, 176–186.
695 Bodinier J.-L., and Godard M. (2014) Orogenic, Ophiolitic, and Abyssal Peridotites. In: Holland H.D.
696 and Turekian K.K. (eds.) Treatise on Geochemistry, 2nd Edition, v3, **103-167**. Oxford: Elsevier.
697 Bodinier J-L, Guiraud M, Fabrie`s J, Dostal J, and Dupuy C (1987) Petrogenesis of layered
698 pyroxenites from the Lherz, Freychinède and Prades ultramafic bodies (Ariège, French
699 Pyrénées). *Geochim. Cosmochim Acta* **51**, 279–290
700 Boyd F. R., and Nixon P. H., (1978) Ultramafic nodules from the Kimberley pipes, South Africa.
701 *Geochim. Cosmochim. Acta* **42**, 1367-82.

Brett R.C., Russell J.K. and Moss, S., (2009) Origin of olivine in kimberlite: Phenocryst or impostor? *Lithos* **112**, 201–212.

Brey G.P. and Köhler, T., (1990) Geothermobarometery in four-phase lherzolith II. New thermobarometrers, and practical assessment of existing thremobarometers. *J. Petrol* **31**, 1353–1378.

Burnard P.G., Demouchy S., Delon R., Arnaud N.O., Marrocchi Y., Cordier P. and Addad, A. (2015) The role of grain boundaries in the storage and transport of noble gases in the mantle. *Earth Planet. Sci. Lett* **430**, 260–270.

Bussweiler Y., Foley S.F., Prelevic D. and Jacob D.E. (2015) The olivine macrocryst problem: New insights from minor and trace element compositions of olivine from Lac de Gras kimberlites, Canada. *Lithos*, **220-223**, 238–252.

Bussweiler Y., Brey G.P., Pearson D.G., Stachel T., Stern R.A., Hardman M.F., Kjarsgaard B.A. and Jackson, S.E.,(2017). The aluminum-in-olivine thermometer for mantle peridotites — Experimental versus empirical calibration and potential applications. *Lithos,* **272-273**, 301–314. doi:10.1016/j.lithos.2016.12.015

Bussweiler Y., Giuliani A., Greig A., Kjarsgaard B.A., Petts D., Jackson S.E., Barrett N., Luo Y., Pearson D.G. (2019) Trace element analysis of high-Mg olivine by LA-ICP-MS – Characterization of natural olivine standards for matrix-matched calibration and application to mantle peridotites. *Chemical Geology* **524**, 136–157.

Coogan L.A., Saunders A.D. and Wilson, R.N. (2014) Aluminum-in-olivine thermometry of primitive basalts: Evidence of an anomalously hot mantle source for large igneous provinces. *Chemical Geology* **368**, 1–10. doi:10.1016/j.chemgeo.2014.01.004

Costa Rodriguez F., Dohmen R. and Demouchy S. (2010) Modeling the dehydrogenation of mantle olivine with implications for the water content of the Earth's upper mantle, and ascent rates of kimberlite and alkali basaltic magmas *Eos Trans*. *AGU, Fall Meet.* Abstract V24C-06.

De Hoog J.C.M., Gall L. and Cornell D.H. (2010) Trace-element geochemistry of mantle olivine and application to mantle petrogenesis and geothermobarometry. *Chem. Geol.* **270**, 196–215.

De Hoog J.C.M., Hattori K and Jung H. (2014) Titanium- and water-rich metamorphic olivine in high-pressure serpentinites from the Voltri Massif (Ligurian Alps, Italy): evidence for deep subduction of high-field strength and fluid-mobile elements. *Contrib. Mineral. Petrol.* **167**, 990.

Delon R., Demouchy S., Marrocchi Y., Bouhifd M.A., Barou F., Cordier P., Addad A. and Burnard, P.G. (2018) Helium incorporation and diffusion in polycrystalline olivine. *Chem. Geol.* **488**, 105–124.

Delon R.M., Demouchy S., Marrocchi Y., Bouhifd M.A., Cordier P., Addad A. and Burnard P.G. (2019) Argon storage and diffusion in Earth's upper mantle. *Geochim. Cosmochim. Acta* **253**, 1–18.

Demouchy S., (2004) Thermodynamics and kinetics of hydrogen incorporation in olivine and wadsleyite, PhD thesis, Bayerisches Geoinstitut, Universität Bayreuth, Bayreuth, Germany. 130 p.

Demouchy S. and Bolfan-Casanova N. (2016) Distribution and transport of hydrogen in the lithospheric mantle: A review. *Lithos* **240-243**, 402–425.

Demouchy S., and Mackwell, S. (2006). Mechanisms of hydrogen incorporation and diffusion in iron-bearing olivine. *Phys. Chem. Minerals.* **33**, 347–355.

Demouchy S., Jacobsen S.D., Gaillard F. and Stern, C.R. (2006) Rapid magma ascent recorded by water diffusion profiles in mantle olivine. *Geology* **34**, 429–432.

Demouchy S., Tommasi A., Barou F., Mainprice D. and Cordier, P. (2012) Deformation of olivine in torsion under hydrous conditions. *Phys. Earth Planet. Int.* **202-203**, 57–70.

Demouchy S., Ishikawa A., Tommasi A., Alard O., and Keshav, S. (2015) Characterization of hydration in the mantle lithosphere: Peridotite xenoliths from the Ontong Java Plateau as an example. *Lithos*, **212-215,** 189–201.

Demouchy S., Tommasi A., Ionov D., Higgie K. and Carlson R.W. (2019) Microstructures, Water Contents, and Seismic Properties of the Mantle Lithosphere beneath the Northern limit of the Hangay Dome, Mongolia. *Geochem. Geophys. Geosyst*. 2018GC007931.

Denis C.M.M., Demouchy S. and Shaw C. (2013) Evidence of dehydration in peridotites from Eifel Volcanic Field and estimates of magma ascent rates. *J. Volc. Geoth. Res.* **258**, 85–99.

Denis C.M.M, Alard O., and Demouchy, S. (2015) Water content and hydrogen behavior during metasomatism in the uppermost mantle beneath Ray Pic volcano (Massif Central, France). *Lithos*. **237**, 256-274.

Denis C.M.M., Demouchy S. and Alard O., (2018) Heterogeneous hydrogen distribution in orthopyroxene from veined mantle peridotite (San Carlos, Arizona): Impact of melt-rock interactions. *Lithos* **302-303**, 298–311.

D'Souza, R.J., Canil, D., Coogan, L.A., 2020. Geobarometry for spinel peridotites using Ca and Al in olivine. *Contrib. Miner. Petrol.* **175**, 241–13. doi:10.1007/s00410-019-1647-6

Ellis D. J., and Green D. H., (1979) An experimental study of the effect of Ca upon garnet-clinopyroxene Fe-Mg exchange equilibria. *Contrib. Miner. Petrol.* **71**, 13-22

Falus G., Tommasi A., Ingrin J. and Szabo, C. (2008) Deformation and seismic anisotropy of the lithospheric mantle in the Southeastern Carpathians inferred from the study of mantle xenoliths. *Earth Planet. Sci. Lett.* 272, **50**–64.

Faul U.H., Cline C.J., II, David E.C., Berry A.J. and Jackson I. (2016) Titanium-hydroxyl defect-controlled rheology of the Earth's upper mantle. *Earth Planet. Sci. Lett.* **452**, 227–237.

Férot A. and Bolfan-Casanova N. (2012) Water storage capacity in olivine and pyroxene to 14 GPa: Implications for the water content of the Earth'supper mantle and nature of seismic discontinuities. *Earth Planet. Sci. Lett.* **349**-350, 218–230.

Foley S.F., Prelevic D. Rehfeldt, T. and Jacob, D.E. (2013) Minor and trace elements in olivine as probe into early igneous and mantle melting processes. *Earth Planet. Sci. Lett.* **363**, 181–191.

Gaetani G.A., O'Leary J.A., Koga K.T., Hauri E.H., Rose-Koga E.F. and Monteleone B.D. (2014). Hydration of mantle olivine under variable water and oxygen fugacity conditions. *Contrib Mineral Petrol* **167**, 965. Doi:10.1007/s00410-014-0965-y

Garrido C.J., Bodinier, J.L. and Alard, O. (2000) Incompatible trace element partitioning and residence in anhydrous spinel peridotites and websterites from Ronda orogenic peridotite. *Earth Planet. Sci. Lett.* 181, 314–358.

Goldschmidt V.M. (1926) The laws of crystal chemistry. *Naturewissenschaften* 1', 477–485.

784 Göse J., Reichart P., Dollinger G. and Schmädicke, E. (2008) Water in natural olivine--determined by
785 proton-proton scattering analysis. *Am. Min.* **93**, 1613–1619.
786 Göse J., Schmädicke E., Markowitz M. and Beran, A. (2010) OH point defects in olivine from
787 Pakistan. *Miner Petrol* **99**, 105–111. doi:10.1007/s00710-009-0095-9
788 Grant K., Ingrin J., Lorand J.P., and Dumas P. (2007) Water partitioning betweenmantle minerals
789 from peridotite xenoliths. *Contrib. Miner. Petrol.* **154**, 15–34.
790 Griffin W.L., Powell W., Pearson N.J. and O'Reilly S.Y., (2008) GLITTER: data reduction software
791 for laser ablation ICP-MS. Laser Ablation-ICP-MS in the Earth Sciences vol. 40. Mineralogical
792 Association of Canada Short Course Series, pp. 204–207 (Appendix 2).
793 Guillong M. and Heinrich C.A. (2007) Sensitivity enhancement in laser ablation ICP-MS using small
794 amounts of hydrogen in the carrier gas. *J. Anal. At. Spectrom.* **22**, 1488.
795 Harlow G.E., Kyaw T., Silbert Z., and Martin al., C. (2014) Hydrothermal re-crystalisation of dunitic
796 olivine: Peridot from Pyaung-Gaung, Myanmar and other examples. 21rst General Meeting of
797 the International Mineralogical Association, abs volume 1-5, 198.
798 Hirschmann M., Aubaud C. and Withers A.C. (2005) Storage capacity of H2O in nominally anhydrous
799 minerals in the upper mantle. *Earth Planet. Sci. Lett.* **236**, 167–181.
800 Hu Z., Gao S., Liu Y., Hu S., Chen H. and Yuan H. (2008) Signal enhancement in laser ablation ICP-
801 MS by addition of nitrogen in the central channel gas. *J. Anal. At. Spectrom*. **23**, 1093.
802 Ingrin J. and Skogby H. (2000) Hydrogen in nominally anhydrous upper-mantle minerals:
803 concentration levels and implications. *Eur. J. Minerals* **12**, 543–570.
804 Jacquet E., Alard O. and Gounelle, M. (2012) Chondrule trace element geochemistry at the mineral
805 scale. *Meteoritics & Planet. Sci.* **47**, 1695–1714.
806 Jean M.M., Taylor L.A., Howarth G.H., Peslier A.H., Fedele L., Bodnar R.J., Guan Y., Doucet L.S.,
807 Ionov D.A., Logvinova A.M., Golovin A.V. and Sobolev N.V. (2016) Olivine inclusions in
808 Siberian diamonds and mantle xenoliths: Contrasting water and trace-element contents. *Lithos*
809 **265**, 31–41.
810 Jochum K.P., Nohl U., Herwig K., Lammel E., Stoll B. and Hofmann A.W. (2005) GeoReM: A New
811 *Geochemical Database for Reference Materials and Isotopic Standards,* **29** (3), 333-338.

812 Jollands M.C., Padrón-Navarta J.A., Hermann J., and O'Neill A.H.S.C. (2016) Hydrogen diffusion in
813 Ti-doped forsterite and the preservation of metastable point defects, *J. Petrol*. doi:10.2138/am-
814 2016-5568
815 Jurewicz A.J.G. and Watson E.B. (1988a) Cations in olivine, Part 1: Calcium partitioning and
816 calcium-magnesium distribution between olivines and coexisting melts, with petrologic
817 applications, *Contrib Mineral Petrol* **99**, 176-85
818 Jurewicz A.J.G., and Watson, E.B. (1988b) Cations in olivine, Part 2: Diffusion in olivine xenocrysts,
819 with application to petrology and mineral physics. *Contrib. Miner. Petrol*. **99**, 186–201.
820 Kelle, J., Zaitsev A.N. and Wiedenmann, D. (2006) Primary magmas at Oldoinyo Lengai: the role of
821 olivine melilitites. *Lithos* **91**, 150–172.
822 Kempf E.D. and Hermann J., (2018) Hydrogen incorporation and retention in metamorphic olivine
823 during subduction: Implications for the deep water cycle. *Geology* **46**, 571–574.
824 Kent A.J.R and Rossman G.R. (2002) Hydrogen, lithium, and boron in mantle-derived olivine: the
825 role of coupled subtitutions. *Am. Min.* **87**, 1432–1436.
826 Kohlstedt D.L. and Mackwell S.J. (1998) Diffusion of hydrogen and intrinsic point defects in olivine.
827 *Z. Phys. Chem.* **207**, 147–162.
828 Kohlstedt D.L., Keppler H. and Rubie, D.C. (1996) Solubility of water in the α, β and γ phases of
829 $(Mg,Fe)_2SiO_4$. *Contrib Mineral Petrol* **123**, 345–357.
830 Kröger F.A. and Vink H.J. (1956) Relation between the concentration of imperfections in crystalline
831 solids. In: *Solid State Physics* **3**, eds. F. Seitz, D. Turnhall, Academic Press, New York, pp 367-
832 435.
833 Le Roux V, Bodinier J.L., Tommasi A., Alard O., Dautria J.M., Vauchez A. and Riches A.J.V. (2007)
834 The Lherz spinel lherzolite: refertilized rather than pristine mantle. *Earth Planet. Sci. Lett.* **259**,
835 599–612.
836 Li Z.X.A., Lee C.T.A., Peslier A., Lenardic A. and Mackwell S.J. (2008) Water contents in mantle
837 xenoliths from the Colorado Plateau and vicinity: implications for the mantle rheology and
838 hydration-induced thining of continental lithosphere. *J. Geophys. Res*. **113**, doi: 10.1029–
839 2007JB005540.

840 Lloyd A.S., Plank T., Ruprecht P., Hauri E.H. and Rose, W. (2012) Volatile loss from melt inclusions
841 in pyroclasts of differing sizes. *Contrib Mineral Petrol* **165**, 129–153.
842 Lloyd A.S., Ferriss E., Ruprecht P., Hauri E.H., Jicha B.R. and Plank, T. (2017) An Assessment of
843 Clinopyroxene as a Recorder of Magmatic Water and Magma Ascent Rate. *J. Petrol.* **57**, 1865–
844 1886.
845 Mackwell S.J. and Kohlstedt D.L. (1990) Diffusion of hydrogen in olivine: Implications for water in
846 the mantle. *J. Geophys. Res.* **95**, 5079–5088.
847 Mackwell, S.J., and Kohlstedt D.L. and Paterson M.S. (1985) The role of water in the deformation of
848 olivine single crystals. *J. Geophys. Res*. **90**, 11–319–11–333.
849 McDonough W.F. and Sun, S.-s. (1995) The composition of the Earth. *Chem. Geol.* **120**, 223–253.
850 Medaris L.G. Jr. (1984) A geothermobarometry investigation of garnet peridotites in the western
851 Gneiss Ragion of Norway. *Contrib Mineral Petrol* **87**, 72-86.
852 Mei S., and Kohlstedt D.L. (2000) Influence of water on plastic deformation of olivine aggregates: 2.
853 Dislocation creep regime. *J Geophys Res* **105**, 21471-21481
854 Miller G.H., Rossman G.R. and Harlow G.E. (1987) The Natural Occurrence of Hydroxide in Olivine.
855 *Phys Chem Minerals* **14**, 461–472.
856 Mosenfelder J.L., Sharp T.G. Asimow, P.D. and Rossman, G.R. (2006) Hydrogen incorporation in
857 natural olivine, in: Earth's Deep Water Cycle. AGU, Washington DC, pp. 45–56.
858 Nakamura A. and Schmalzried H. (1983) On the nonstoichiometry and point defects of olivine. *Phys*
859 *Chem Minerals* **10**, 27–37.
860 Neave D.A., Shorttle O., Oeser M., Weyer S. and Kobayashi K. (2018) Mantle-derived trace element
861 variability in olivines and their melt inclusions. *Earth Planet. Sci. Lett.* **483**, 90–104.
862 O'Reilly S.Y., Chen D., Griffin W.L. and Ryan C. G. (1997) Minor elements in olivine from spinel
863 lherzolite xenoliths: Implication for thermobarometry. *Min. Mag.,* **61**, 257-269.
864 Padrón-Navarta J.A., and Hermann J., (2017) A Subsolidus Olivine Water Solubility Equation for the
865 Earth's Upper Mantle. *J. Geophys. Res. Solid Earth* 122, 9862–9880.
866 Padrón-Navarta J.A., Hermann J., and O'Neill H.S.C., (2014) Site-specific hydrogen diffusion rates in
867 forsterite. *Earth Planet. Sci. Lett* **392**, 100–112. Paterson, M.S., (1982) The determination of

868 hydroxyl by infrared absorption in quartz, silicate glasses and similar materials. *Bull. Minéral,*
869 **105**, 20–29.
870 Peslier A.H. (2010) A review of water contents of nominally anhydrous minerals in the mantles of
871 Earth, Mars and the Moon. *J. Volc. Geoth. Res.* **197**, 239–258.
872 Peslier A. and Luhr, J.F., (2006) Hydrogen loss form olivines in mantle xenoliths from Simcoe (USA)
873 and Mexico: mafic alkalic magma ascent rate and water budget of the sub-continental
874 lithosphere. Earth Planet. Sci. Lett. **242**, 302–314.
875 Peslier, A.H., Woodland, A.B., Bell, D.R., and Lazarov, M., (2010) Olivine water contents in the
876 continental lithosphere and the longevity of cratons. *Nature* **467**, 78–83.
877 Peslier A.H., Woodland A.B., Bell D.R., Lazarote M. and Lapen, T.J. (2012) Metasomatic control of
878 water contents in the kaapvaal cratonic mantle. *Geochim. Cosmochim. Acta* **97**, 213–246.
879 Peslier A.H., Bizimis M. and Matney M. (2015). Water disequilibrium in olivines from Hawaiian
880 peridotites: Recent metasomatism, H diffusion and magma ascent rates. *Geochim. Cosmochim.*
881 *Acta* **154**, 98-117.
882 Peslier A.H., Schönbächler M., Busemann H. and Karato S.-I. (2017) Water in the Earth's Interior:
883 Distribution and Origin. *Space Sci Rev*, DOI 10.1007/s11214-017-0387-z
884 Philibert J. (1995) Atom movement, diffusion and mass transport in solids. Eds. *Editions de physique*
885 *Sciences*. **602** ISBN: 978-2-86883-161-3
886 Prelevic D. and Foley S. (2007) Accretion of arc-oceanic lithospheric mantle in the Mediterranean:
887 Evidence from extremely high-Mg olivines and Cr-rich spinel inclusions in lamproites. *Earth*
888 *Planet. Sci. Lett.***256**, 120–135.
889 Rasmussen, M.B., Halldórsson, S.A., Gibson, S.A., and Guðfinnsson, G.H., 2020. Olivine chemistry
890 reveals compositional source heterogeneities within a tilted mantle plume beneath Iceland.
891 *Earth Planet. Sci. Lett.* **531**, 116008. doi:10.1016/j.epsl.2019.116008
892 Rauch M., (2000) Der Einbau von Wasser in Pyroxene. PhD thesis, Bayerisches Geoinstitut.
893 Universität Bayreuth, Bayreuth, Germany. 141 p.
894 Ringwood A. E. (1955) the principle governing trace element distribution during magmatic
895 crystallization, *Geochim. Cosmochim. Acta* **7**, 189-202.

896 Satsukawa T., Godard M., Demouchy S., Michibayashi K. and Ildefonse B. (2017) Chemical
897 interactions in the subduction factory: New insights from an *in situ* trace element and hydrogen
898 study of the Ichinomegata and Oki-Dogo mantle xenoliths (Japan). *Geochim. Cosmochim. Acta*
899 **208**, 234–267.
900 Scheffler G.L. and Pozebon D. (2014) Advantages, drawbacks and applications of mixed Ar–N
901 2sources in inductively coupled plasma-based techniques: an overview. Anal. Methods 6, 6170–
902 6182.
903 Schmalzried H., (1981) Solid State Reactions, 2nd ed. Verlag Chemie, Weinheim.
904 Schwartz K. and Lang M. (2016) Mineral Defects. In: White W. (eds) Encyclopedia of Geochemistry.
905 Encyclopedia of Earth Sciences Series. Springer.
906 Skogby, H., 2006. Water in Natural Mantle Minerals I: Pyroxenes. *Reviews in Mineralogy and*
907 *Geochemistry* **62**, 154-167
908 Sobolev A.V., Kuzmin D.V., Yaxley G.M., Arndt N.T., Chung S.L., Danyushevsky L.V., Elliott
909 T., Frey F.A., Garcia M.O., Gurenko A.A., Kamenetsky V.S., Kerr A.C., Krivolutskaya
910 N.A., Matvienkov V.V., Nikogosian I.K., Rocholl A., Sigurdsson I.A., Sushchevskaya
911 N.M., and Teklay M., (2007) The Amount of Recycled Crust in Sources of Mantle-Derived
912 Melts, *Science*, **5823**, 412-417.
913 Soustelle V., Tommasi A., Demouchy S. and Franz L., (2013) Melt-rock interactions, deformation,
914 hydration and seismic properties in the sub-arc lithospheric mantle inferred from xenoliths from
915 seamounts near Lihir, Papua New Guinea. *Tectonophysics* **608**, 330–345.
916 Spandler C. and O'Neill H.S.C. (2010) Diffusion and partition coefficients of minor and traces
917 elements in San carlos olivine at 1,300°C with some geochemical implications. *Contrib Mineral*
918 *Petrol* doi: 10.1007/s00410-009-0456-8.
919 Stalder R. (2004) Influence of Fe, Cr, and Al on hydrogen incorporation in orthopyroxene. *Eur. J.*
920 *Mineral.* **16**, 703–711.
921 Sykes D., Rossman G.R., Veblen D.R. and Grew E.S. (1994) Enhanced H and F incorporation in
922 borian olivine. *Am. Min.* **79**, 904–908.

923 Tian Z.-Z., Liu J., Xia Q.-K., Ingrin J., Hao Y.-T., and Depecker C. (2017) Water concentration
924 profiles in natural mantle orthopyroxenes: A geochronometer for long annealing of xenoliths
925 within magma. *Geology*, doi:10.1130/G38620.1
926 Thoraval C. and Demouchy S., (2014) Numerical models of ionic diffusion in one and three
927 dimensions: application to dehydration of mantle olivine. *Phys. Chem. Minerals* **41**, 709–723.
928 Thoraval C., Demouchy S. and Padrón-Navarta, J.-A. (2019) Relative diffusivities of hydrous defects
929 from a partially dehydrated natural olivine. *Phys Chem Minerals*,
930 https://doi.org/10.1007/s00269-018-0982-x
931 Tielke J.A., Zimmerman,M.E. and Kohlstedt, D.L., (2017) Hydrolytic weakening in olivine single
932 crystals. *J Geophys. Res.* **122**, 3465–3479. http://dx.doi.org/10.1002/2017JB014004.
933 Tollan P.M.E., O'Neill H., S., C., and Hermann J., (2018) The role of trace elements in controlling H
934 incorporation in San Carlos olivine. *Contrib Mineral Petrol* doi: 10.1007/s00410-018-1517-7
935 Veter M., Foley S.F., Mertz-Kraus, R. and Groschopf, N., (2017) Trace elements in olivine of
936 ultramafic lamprophyres controlled by phlogopite-rich mineral assemblages in the mantle
937 source. *Lithos* **292-293**, 81–95.
938 Veter M., Foley and Alard, O. (2019) Improved LA-ICP-MS Analytical Routine for Low-
939 Concentration Chalcophile and Siderophile Elements in Olivine and Orthopyroxene,
940 *Goldschmidt Abstracts* (03e/50/We).
941 https://goldschmidt.info/2019/abstracts/abstractView?id=2019002975
942 Wade J., Plank T., Hauri E.H., Roggensack K. and Zimmer M. (2008) Prediction of magmatic water
943 contents measurements of H_2O in clinopyroxene phenocryst. *Geology* **36**, 799–802.
944 Walker A.M., Hermann J., Berry A. and O'neill, H.S. (2007) Three water sites in the upper mantle
945 olivine and the role of titanium in the water weakening mechanism. *J. Geophys. Res.*
946 doi:10.1029–2006JB004620.
947 Wan Z., Coogan L.A., and Canil D. (2008) Experimental calibration of aluminum partitioning
948 between olivine and spinel as a geothermometer. *Am. Min.* **93**, 1142–1147.
949 Wells P. R. A. (1977) Pyroxene thermometry in simple and complex systems. *Contrib. Miner. Petrol.*
950 **62**, 129-39.

951 Withers A.C. and Hirschmann M.M., (2008) Influence of Temperature, composition, slica activity and
952 oxygen fugacity on the H_2O storage capacity of olivine at 8 GPa. *Contrib Mineral Petrol,* doi–
953 10:007–s00410–008–0303–3.
954 Withers A.C., Bureau H., Raepsaet C. and Hirschmann M.M. (2012) Calibration of infrared
955 spectroscopy by elastic recoil detection analysis of H in synthetic olivine. *Chem. Geol*. **334**, 92–
956 98.
957 Xia Q.-K., Liu J., Kovács I., Hao Y.-T., Li P., Yang X.-Z., Chen H. and Sheng, Y.-M. (2019) Water in
958 the upper mantle and deep crust of eastern China: concentration, distribution and implications.
959 *National Science Review*. doi: 10.1093/nsr/nwx016
960 Yang X.-Z., Xia Q.-K., Deloule E., Dallai L., Fan Q.-C., and Feng, M. (2008) Water in minerals of the
961 continental lithospheric mantle and overlying lower crust: A comparative study of peridotite and
962 granulite xenoliths from the North China Craton. *Chem. Geol.* **256**, 33–45.
963 Zamboni D., Trela J., Gazel E., Sobolev A.V., Cannatelli C., Lucchi F., Batanova V.G. and De Vivo
964 B., (2017) New insights into the Aeolian Islands and other arc source compositions from high-
965 precision olivine chemistry. *Lithos* **272-273**, 185–191. doi:10.1016/j.lithos.2016.12.004
966 Zhang LY., Li N. and Prelevic D., (2016) The research of olivine trances in-situ analyses and
967 perspectives of its application. *Acta Petrol. Sinica*, **32**(6), 1877-1890.
968

969 **Figure captions**

970 **Fig. 1** Forsterite contents (Fo% = 100 × Mg/(Mg+Fe)) of each analyzed olivine. Color coding:
971 Dark-blue for the hydrogen-rich hydrothermal olivine (SAP, NW1, NW2); pale-blue for
972 the hydrogen-poor hydrothermal olivine (MYA); black for the magmatic olivine (LR);
973 dark-green for the garnet-bearing peridotitic olivine (PA3); brown-green for high
974 temperature spinel-bearing peridotitic olivine (SAS21), and green for the spinel-bearing
975 peridotitic olivines (DMP2, DMP4, SC, SC2018, SAS41, SAS20, OLM, PP, HS1, LAZ).

Fig. 2 Representative unpolarized infrared spectra for each olivine. All spectra are normalized to 1 cm thickness, and off-set vertically for clarity. Polarized IR spectra triplets for each sample are provided in Fig. S2. Color coding identical to Fig. 1 caption.

Fig. 3 Representative polarized IR spectra for olivine PA3. All spectra are normalized to 1 cm thickness, and off-set vertically for clarity.

Fig. 4 Variations of the integrated absorbance (normalized to 1 cm of thickness and proportional to hydrogen concentration) from polarized FTIR profiles of olivine PA3 along the different crystallographic directions and for the three directions of polarization for the di-electric vector.

Fig. 5 Variations of hydrogen concentration as a function of forsterite content (Fo% = 100 × Mg/(Mg+Fe) a.p.f.u.). The primitive mantle value is ca. Fo% = 89.0 (McDonough and Sun, 1995). Color coding identical to Fig. 1 caption.

Fig. 6 Variations of (a) hydrogen concentration in ppm H as a function of the sums of (a) minor, elements, solid symbol Ni+Mn, hollow symbols Ni+Mn+Ca ; (b) Relationships between the sum of trace elements contents and H concentration., with the three groups I, II, III, (c) low trace elements and (d) ultra-trace element concentrations in ppm. Minor (ME), Trace (TE), low -trace (LTE) and ultra-trace (UTE) elements are defined as follow: [ME] ≥1000 ppm, 10 ≤[TE]<1000 ppm, 0.1≤[LTE]<10, [UTE]<0.1 ppm, see text for further detail and Table S5 for the listing of elements belonging to each set. Color coding identical to Fig. 1 caption.

Fig. 7 Selected trace and ultra-trace element concentration patterns normalized to the primitive mantle composition (McDonough and Sun, 1995) for the studied olivines. For clarity, the patterns are separated in two panels: (a) hydrothermal olivines (SAP, NW1, NW2, MYA) and the magmatic olivine (LR). (b) all mantle derived olivines (OLM, SC, SC2018, PA3, SAS20, SAS21, SAS41, LAZ, HS1, PP, DMP2, DMP4). We added the in-house standard

SCO1 as well. Note that the arrows are indicating that the concentrations for these elements are below detection limits (See Table S4 for detection limits).

Fig. 8 Variations of hydrogen concentrations as a function of monovalent elements: Li (cross symbol), Na (multiplication symbol) and both the sum of Li+Na (circle symbol). Color coding identical to Fig. 1 caption.

Fig. 9 (a) Variations of hydrogen concentration linked to the 3355 and 3327 cm^{-1} IR bands as a function of the sums of trivalent element in all olivines. (b) Variations of hydrogen concentration as a function of Cr, Al, B, Sc, V and sum of REE in mantle-derived olivine and magmatic olivine displaying the 3355 and 3327 cm^{-1} IR bands. (c) Variations of bulk hydrogen concentration in the hydrothermal olivines (SAP, NMW1, NW2, MYA) as a function of the sum of trivalent elements (B+Al+Sc+Cr+V) and of B concentration (all in $\mu mol \bullet g^{-1}$). Color coding identical to Fig. 1 caption.

Fig. 10 (a) Ti concentrations in ppm determined by LA-ICP-MS as a function of the normalized integrated absorbance from the two IR bands attributed to the titanium clinohumite-like point defects (3575 and 3525 cm^{-1}). Only samples displaying these OH bands are included here (see Table 1). For comparison, results from other studies are also reported (Demouchy et al., 2015; Faul et al., 2016; Padrón-Navarta and Hermann, 2017; Denis et al., 2018; Tollan et al., 2018). (b) Histogram of Ti concentrations observed in mantle-derived spinel-bearing and garnet-bearing peridotites (data from O'Reilly et al., 1997; De Hoog et al., 2010; Peslier, 2010; Peslier et al., 2012; Satsukawa et al., 2017). (c) Ti molar concentration as a function of H molar concentration in olivine from this study and from Padrón-Navarta and Hermann (2017) and Tollan et al., (2018) calculated from two different IR calibrations (B03: Bell et al., 2003) and W12 (Withers et al., 2012).

Fig. 11 Ti concentrations in ppm (logarithmic scale) as a function of Ca concentration in ppm in olivine from this study and from various lithology and/or geological settings:

chondrules (Jacquet et al., 2012), megacrysts (Bell et al., 2004), kimberlites (Brett et al., 2009; De Hoog et al., 2010), picrites from Baffin (De Hoog, et al., 2010), lamprophyre (Prelevic and Foley, 2007; Foley et al., 2013), rift volcanics (Keller et al., 2006; Foley et al., 2013), metaserpentinites (De Hoog et al., 2014), and mantle xenoliths (O'Reilly et al., 1997; De Hoog et al., 2010; Peslier, 2010;, Peslier et al., 2012; Satsukawa et al., 2017).

Fig. 12 Hydrogen concentrations as a function of Ca concentration in olivines from this study and from various studies on spinel-bearing and garnet-bearing mantle-derived peridotites (Demouchy, 2004; Grant et al., 2007; Falus et al., 2008; Li et al., 2008; Yang et al., 2008; Peslier et al., 2010, 2012; Denis et al., 2013, 2015, 2018; Soustelle et al., 2013; Demouchy et al., 2015, 2019; Satsukawa et al., 2017). Color coding identical to Fig. 1 caption.

Fig. 13 Variation of hydrogen molar concentrations against the sum of key atomic impurities all concentrations are in $\mu mol \bullet g^{-1}$. Key atomic impurities here presented are, (excluding divalent ions): solid symbols = the sum of the trace+low trace+ ultra-elements, and open symbols = the sum of Ti+B+Al+Cr+Sr+V. Color coding identical to Fig. 1 caption.

Table captions

Table 1 Olivine prism sizes after sample preparation and OH band positions for each olivine specimen as identified by unpolarized FTIR spectroscopy.

Table 2 Major and minor element concentrations determined by semi-quantitative μXRF for each olivine.

Table 3 Hydrogen concentrations (ppm H_2O wt) in olivine specimens obtained by unpolarized ('unpo') and polarized ('po') FTIR using the frequency-dependent calibration of Paterson (1982; 'Pat') and the mineral-dependent calibration of Withers et al. (2012; 'W')

1051 respectively. Concentrations are given in ppm H (equals to molar concentration), ppm of
1052 H_2O by weight and $H/10^6Si$. The average integrated absorbances normalized to sample
1053 thickness are compiled in Table S1, and integrations were performed in the 3650–3050
1054 cm^{-1} wavenumber range.

1055 **Table 4** Minor, trace, and ultra-trace element concentrations (ppm) measured by LA-ICP-MS
1056 analyses of the olivine specimens (*n* is the number of the measurements and ±1SD the
1057 standard deviation; typical detection limits for each element are given in Table S3).

1058

1059 **Supplementary material - Figure captions**

1060 **Fig. S1** (a) Photography of olivine specimens during cutting and polishing preparations step,
1061 from left to right, Norway, Sapat, San Carlos#1, #2, #3, La Réunion ; (b) Olivine
1062 specimens glue on glass section prior to X-ray fluorescence mapping and Laser ablation-
1063 inductively coupled plasma-mass spectrometry. One square is 5 mm.

1064 **Fig. S2** Sets of FTIR spectra of olivines not presented in the main text: (a) SAP, (b) MYA, (c)
1065 LR, (d) OLM, (e) NW1 and NW2, (f) SAS41, SAS20, and SAS21, (g) LAZ, (h) SC2018
1066 and SC, and (i) HS1, PP, and DMP. All spectra are normalized to 1 cm thickness.

1067 **Fig. S3** Integrated absorbance distributions across (a) SAS20 and (b) NW1 as representative of
1068 the homogeneous distributions observed across all olivine specimens except PA3

1069 **Fig. S4** Deconvolution details for the samples LR, LAZ, PA3, SAS20, SAS41, performed
1070 with the multipeak fitting package of IGOR PRO™
1071 (https://www.wavemetrics.com/products/igorpro)

1072 **Fig. S5** Variations of Ni content (at. ppm) as a function of forsterite content (Fo% = 100 ×
1073 Mg/(Mg+Fe) a.p.f.u.) in the olivines studied herein and in previous studies: garnet
1074 peridotites (Peslier et al., 2010, 2012), spinel-bearing peridotites (O'Reilly et al., 1997;
1075 Satsukawa et al., 2017), olivine phenocrysts from Aeolian island arc lavas (Zamboni et

al., 2017; *NB*, the field of arc lavas extends down to 200 ppm Ni and Fo% = 60), olivine in various types of troctolites (Basch et al., 2018), and MORBs, OIBs (Hawaii), and Komatiites (Sobolev et al., 2007)

Fig. S6 Selected plots of trace elements as a function of trace element concentrations in $\mu mol \bullet g^{-1}$ (B vs Li; Ti vs Cr/Na; Cr vs B; B vs H)

Fig. S7 Selected plots of trace elements as a function of trace element concentrations in $\mu mol \bullet g^{-1}$ (Ti vs V; Cr vs V; Cr vs Al; Li vs B)

Fig. S8 Sum of mono-, di-, tri-, tetra and penta-valent elements as a function of hydrogen concentration in ppm by weight.

Fig. S9. (a) Sum of trivalent elements vs. sum of the monovalent elements; (b) Sum of trivalent elements vs. sum of the tetravalent elements; (c) Sum of tetravalent elements vs. sum of the monovalent elements; (d) Sum of pentavalent elements vs. sum of the monovalent elements.

Supplementary material – Table captions

Table S1 Average integrated absorbances normalized to sample thickness in the studied olivines from unpolarized and polarized FTIR analyses in the 3650–3100 cm^{-1} wavenumber range

Table S2 Summary of the deconvolution results for unpolarized average spectra of olivines LR, LAZ, PA3, SAS20, SAS41, performed with the multipeak fitting package of IGOR PRO (https://www.wavemetrics.com/products/igorpro)

Table S3 Major and selected minor element concentrations for in-house standard SCO-1 as determined by µXRF, electron microprobe, and LA-ICP-MS analyses

Table S4 Minor, trace, and ultra-trace element concentrations determined by LA-ICP-MS for the standards used in this study (BCR2-G and BHVO2-G). Typical, best, and worst detection limits per element are also listed.

Table S5 Abundance and thus classification of the atomic impurities in each olivine used in the main text.

Demouchy and Alard, Fig. 1 Revised

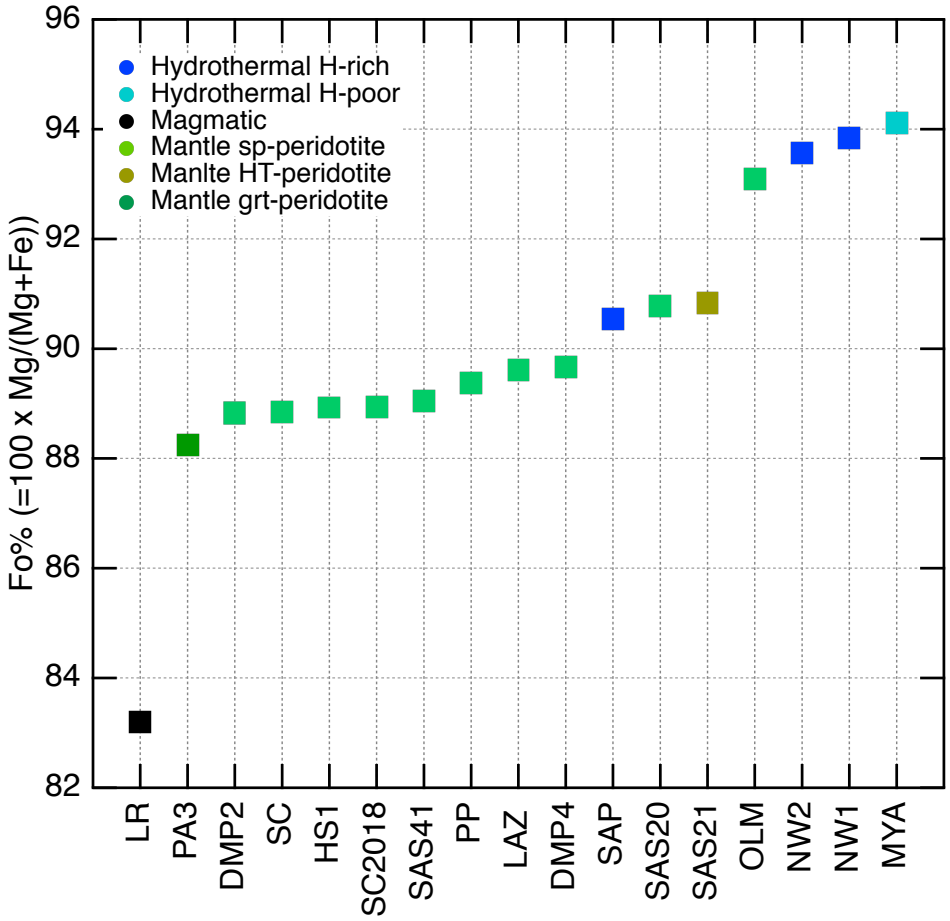

Demouchy and Alard, Fig. 2, Revised

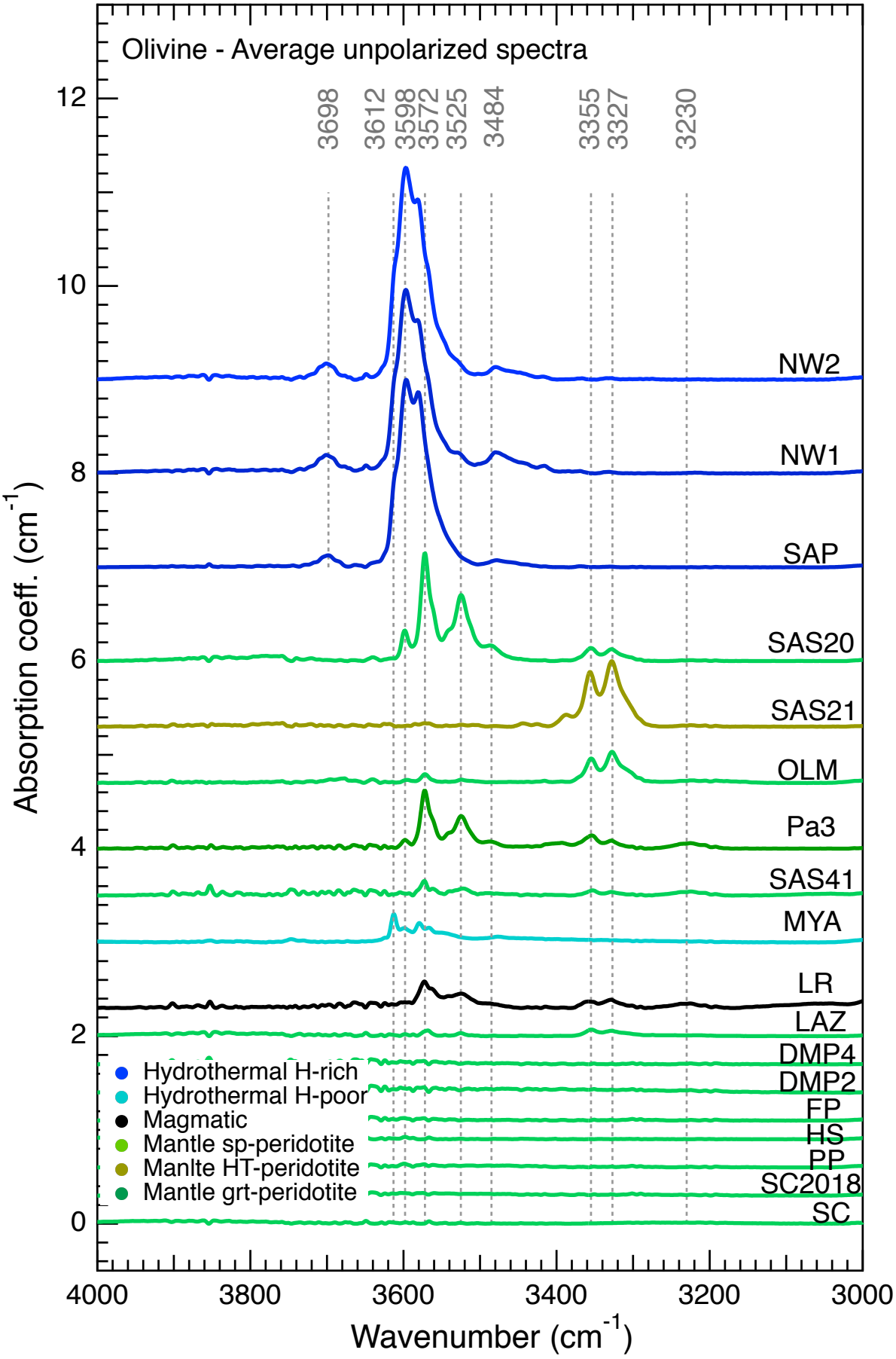

Demouchy and Alard, Fig. 3

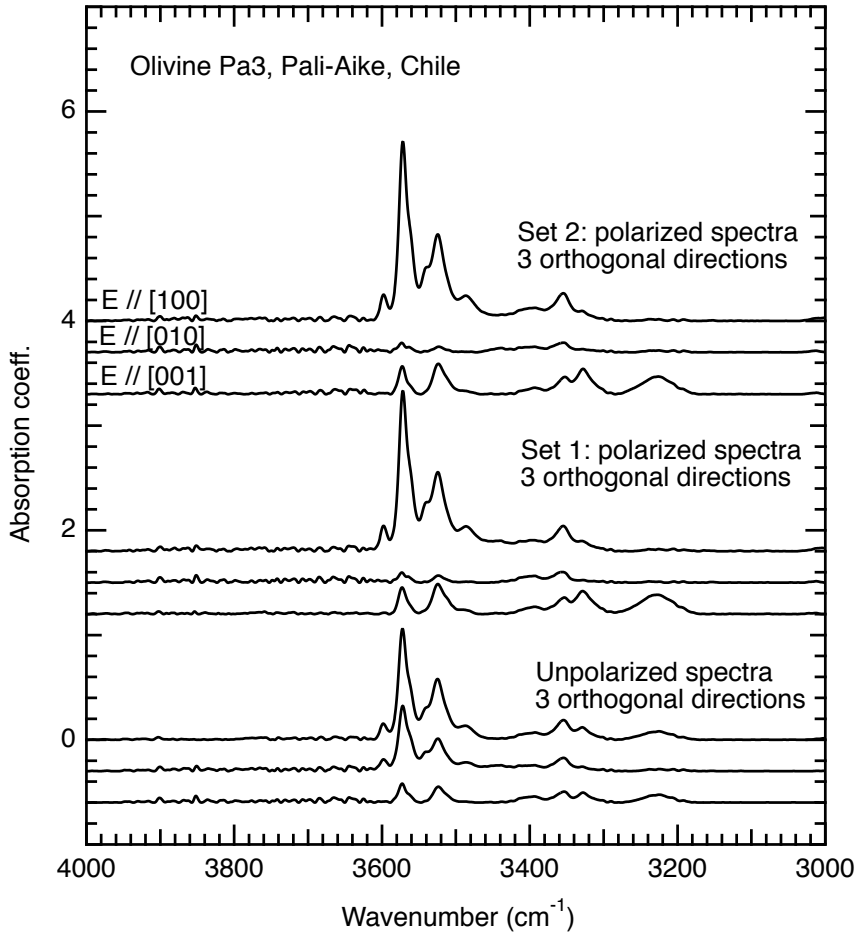

Demouchy and Alard, Fig. 4

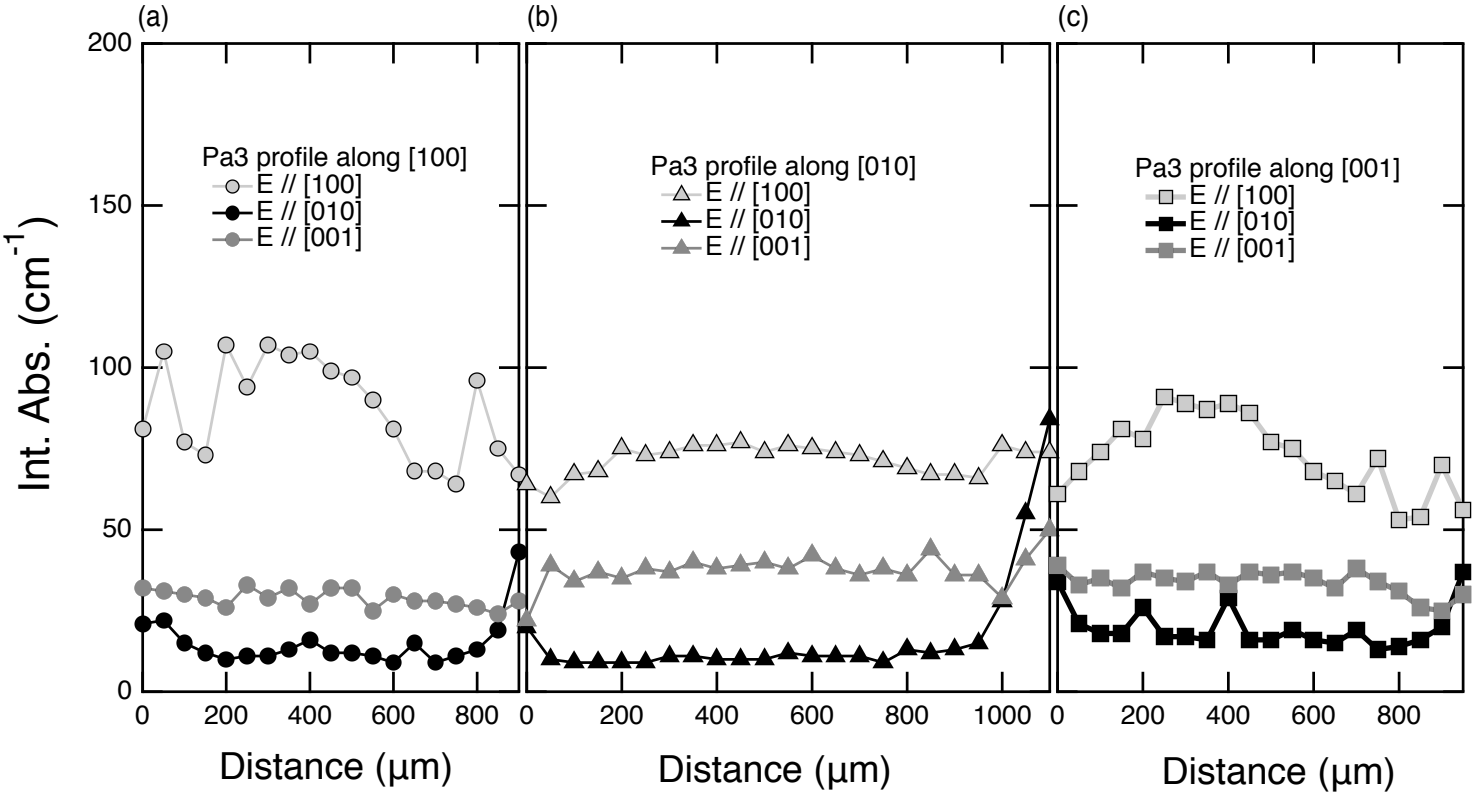

Demouchy and Alard, Fig. 5

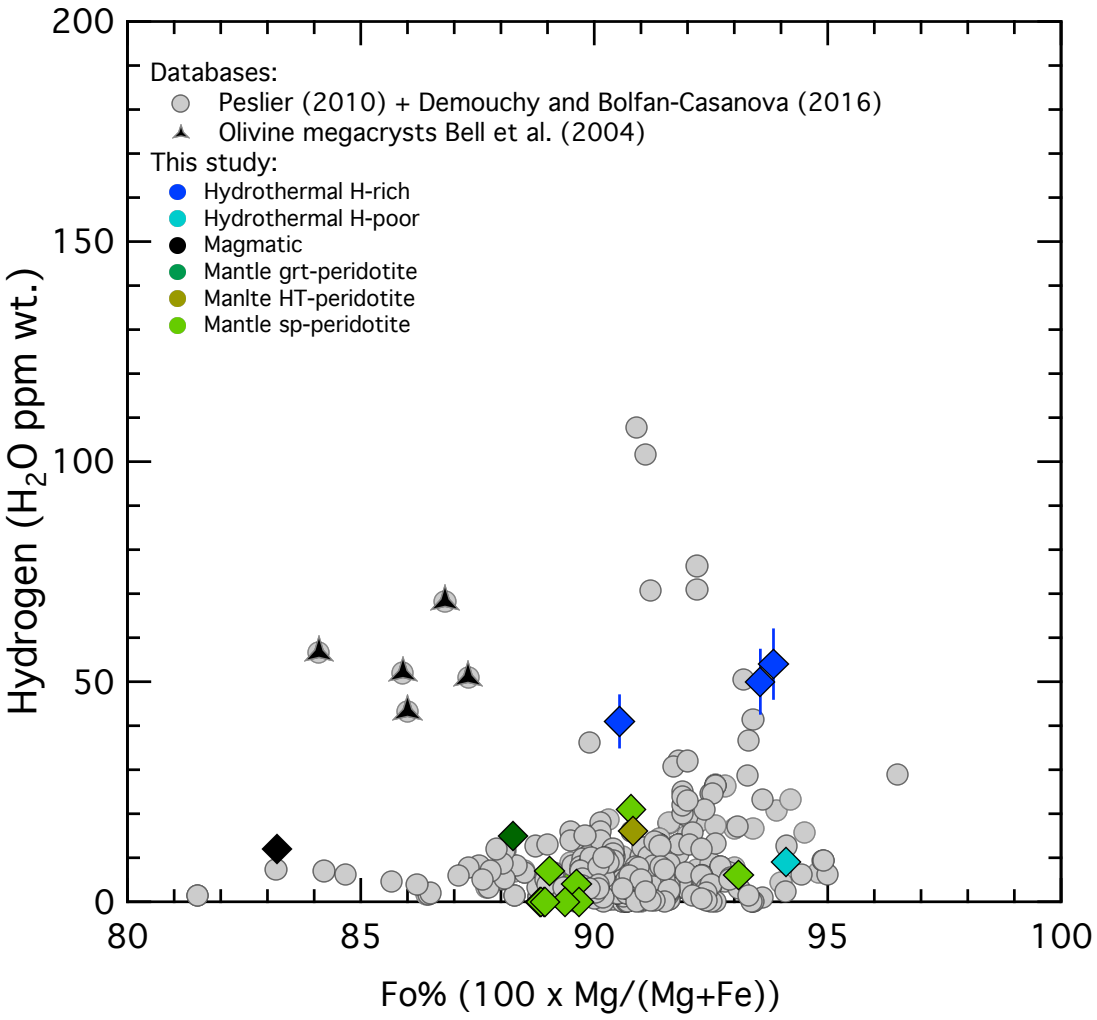

Demouchy and Alard, Fig. 6

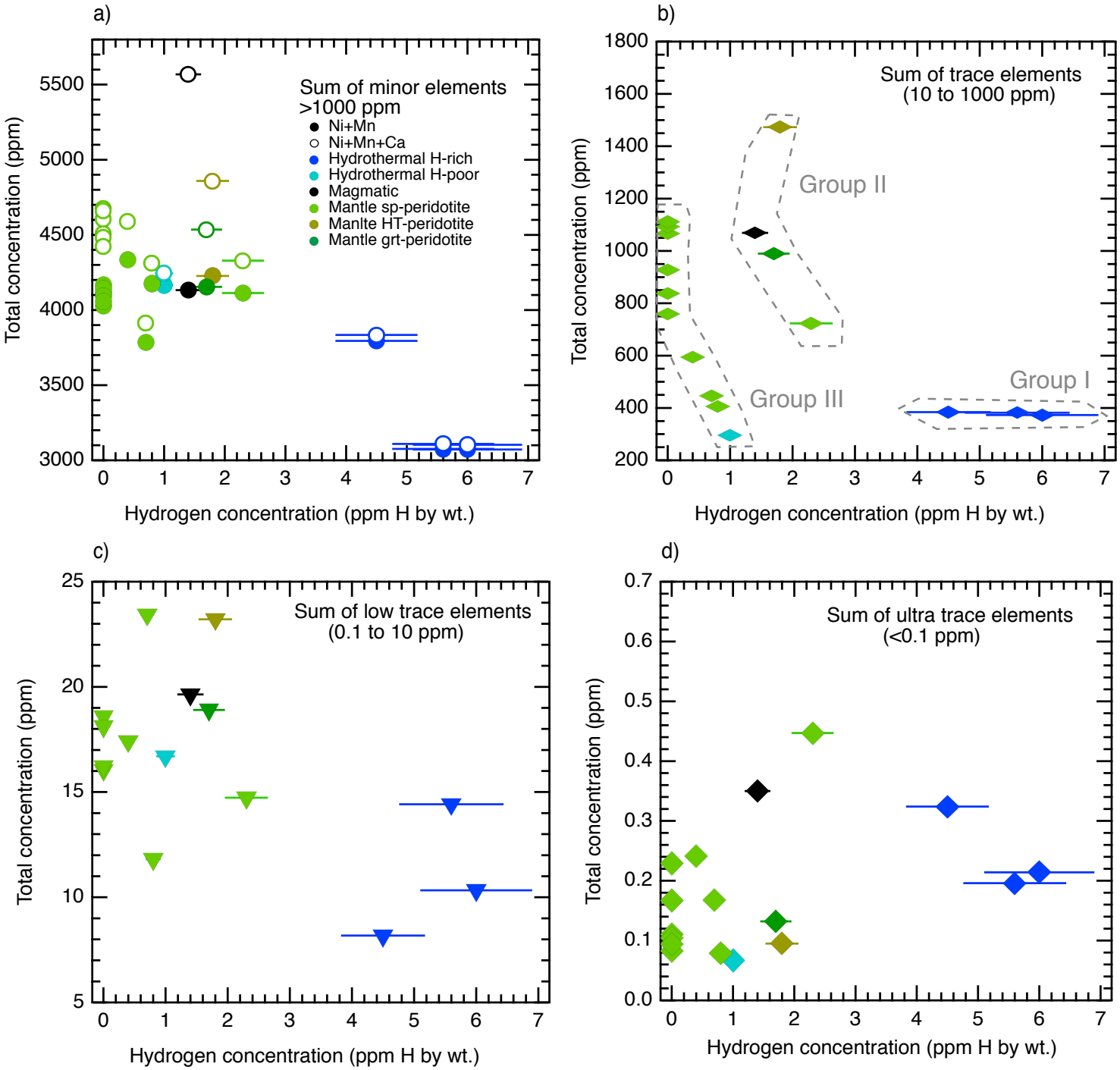

Demouchy and Alard, Fig. 7 Revised

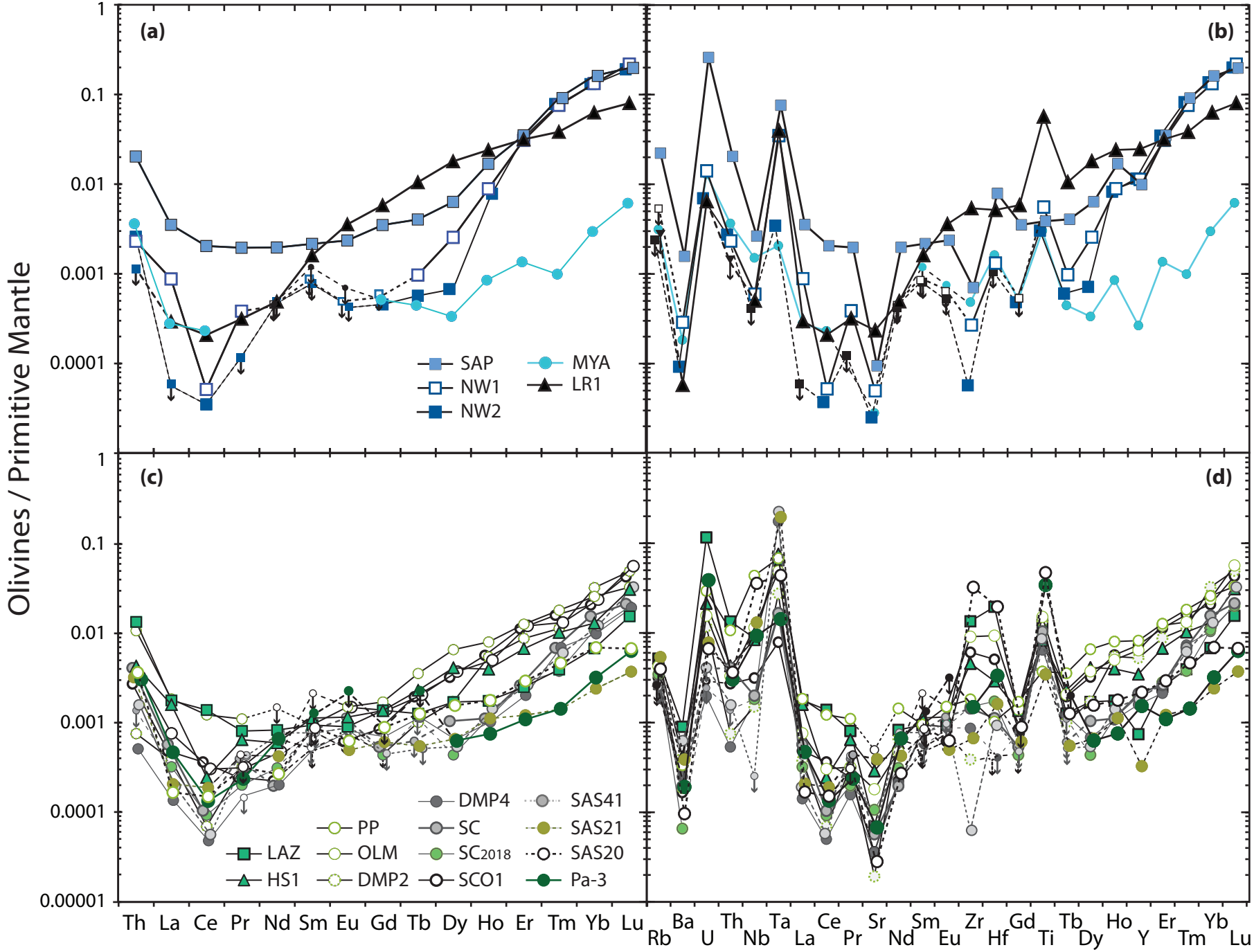

Demouchy and Alard, Fig. 8, Revised

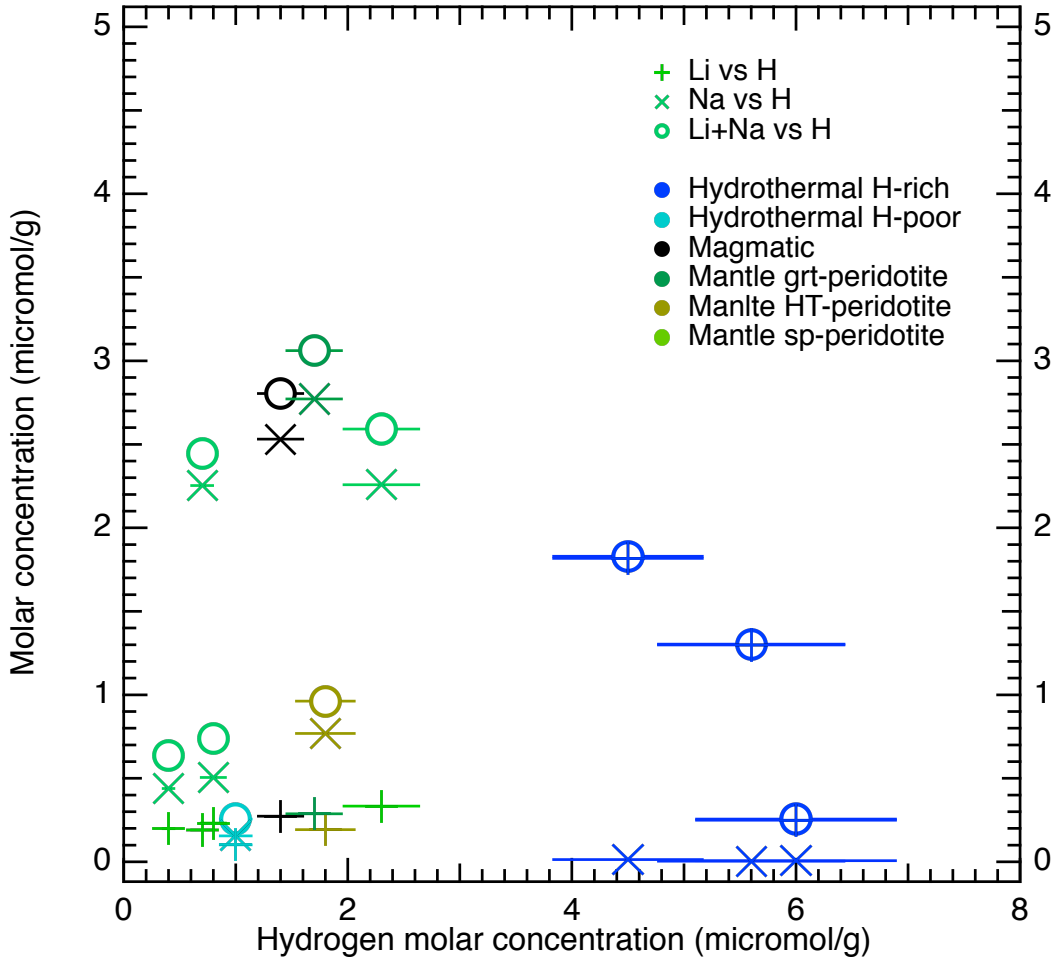

Demouchy and Alard, Fig. 9, Revised

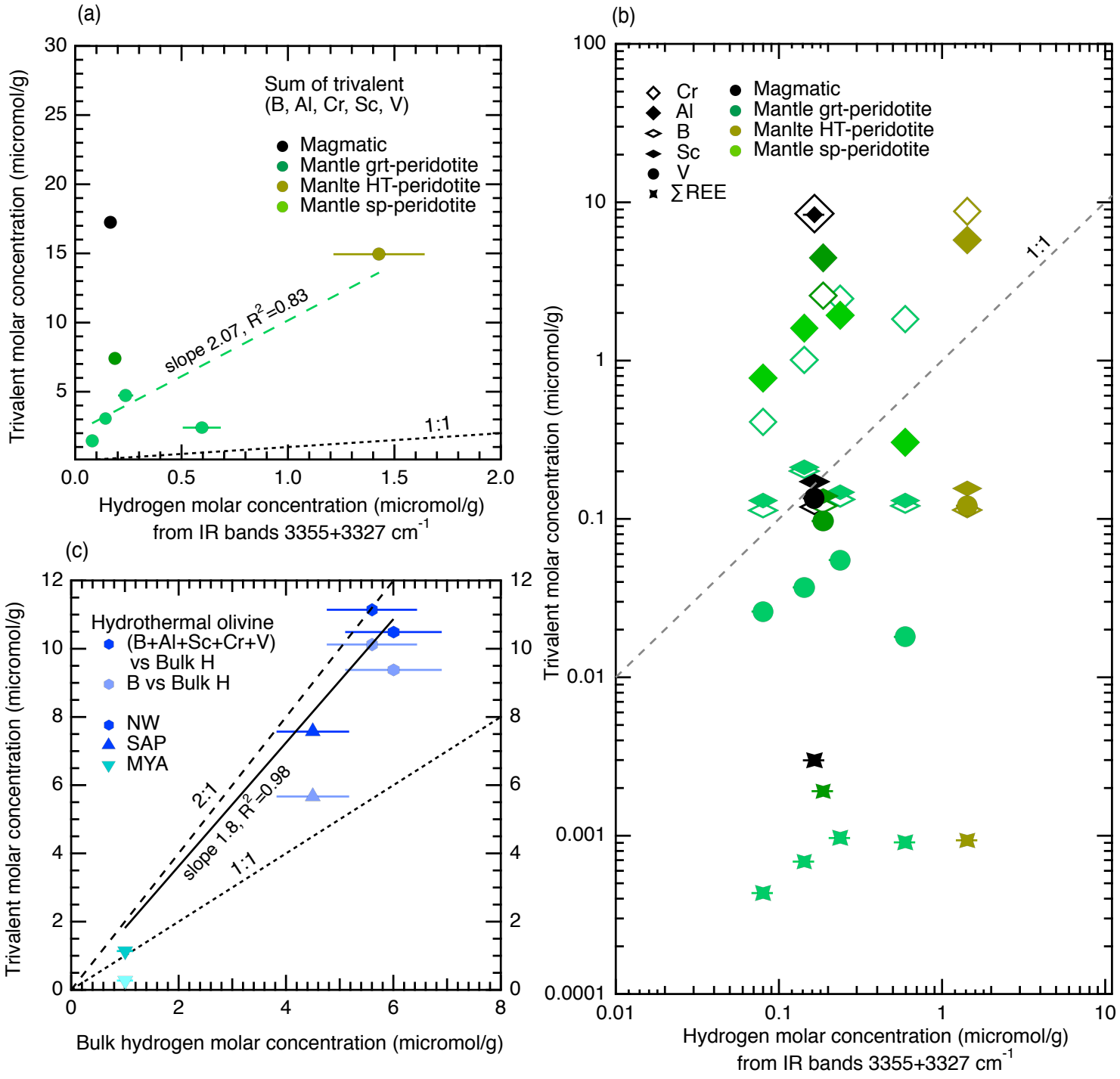

Demouchy and Alard, Fig. 10, Revised

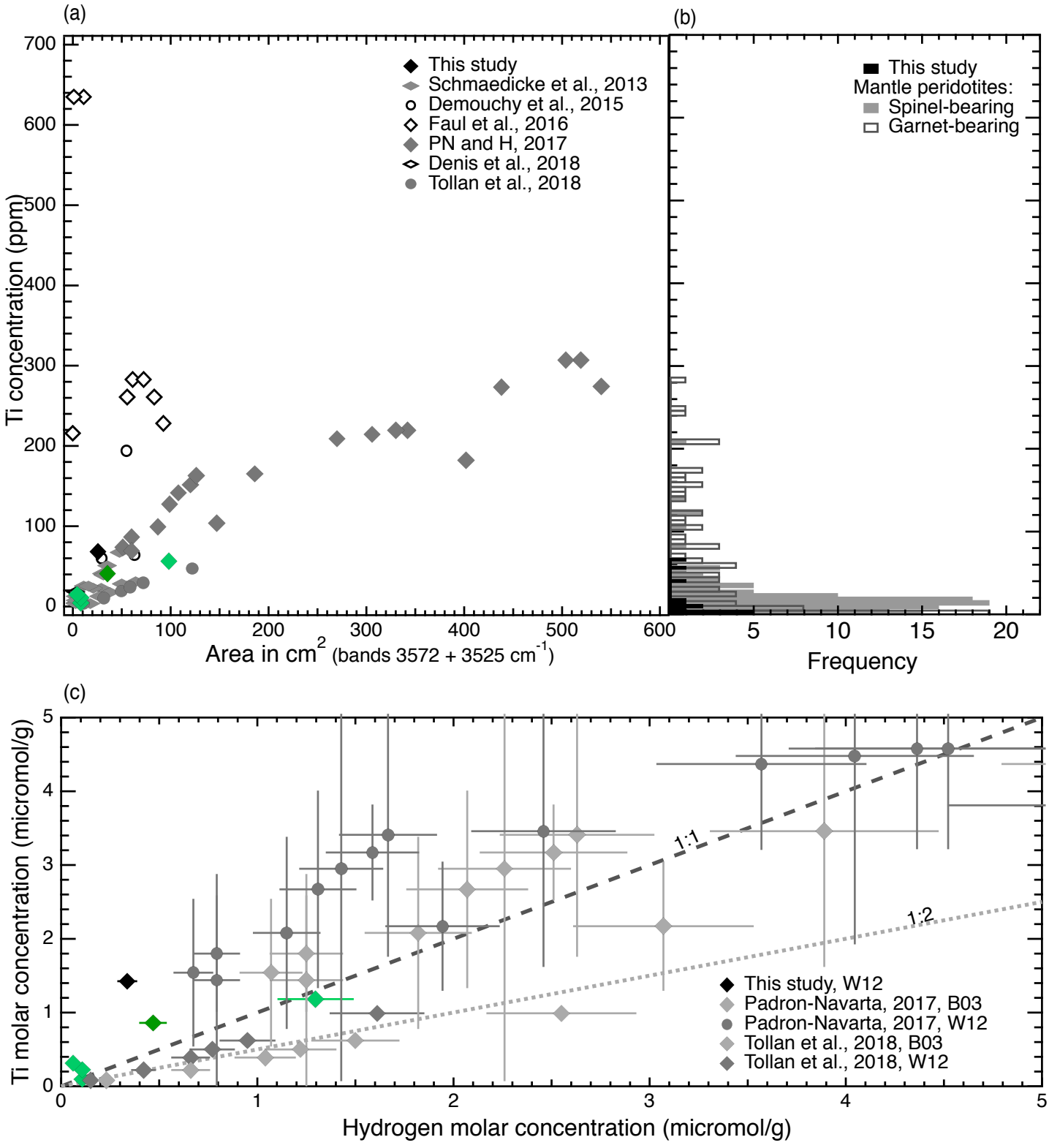

Demouchy and Alard, Fig. 11

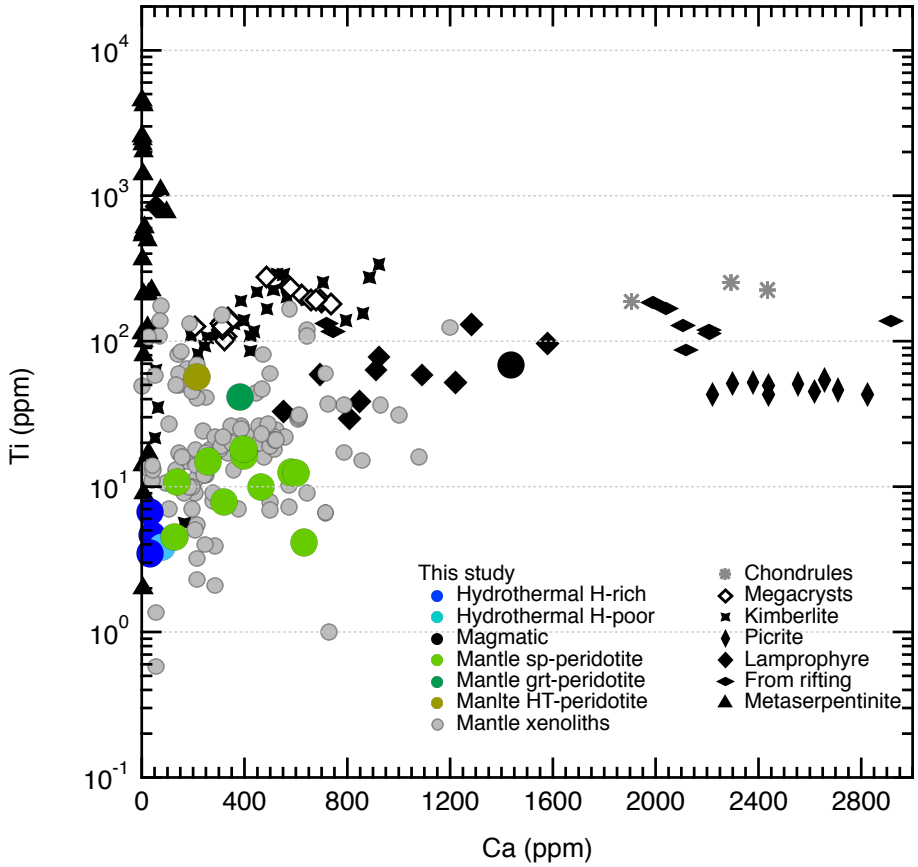

Demouchy and Alard, Fig. 12, Revised

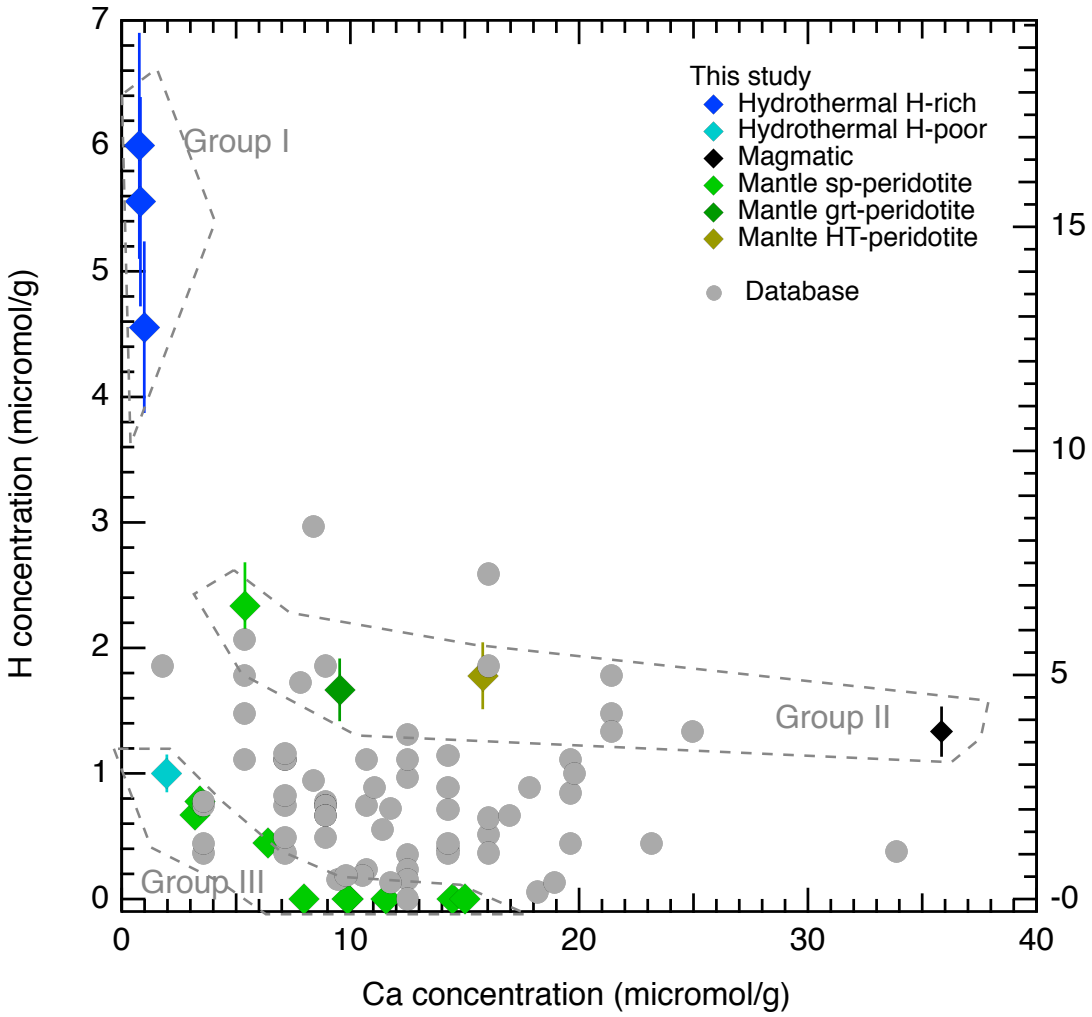

Demouchy and Alard, Fig. 13, Revised

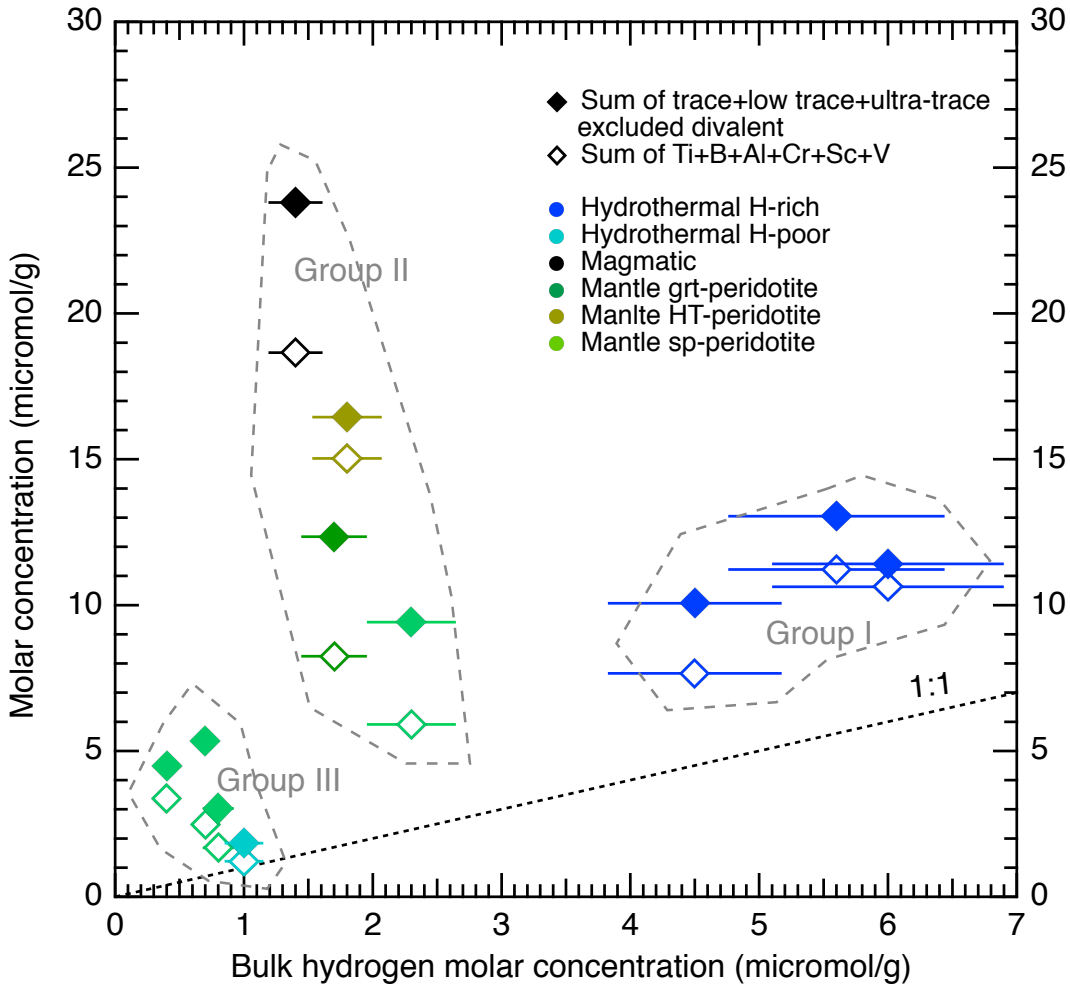

Table 1. Olivine prism sizes after sample preparation and OH band positions for each olivine specimen as identified by unpolarized FTIR.

		SAP	MYA	LR	OLM	NW1	NW2	SAS41	SAS20	SAS21	LAZ	PA3	DMP2	DMP4	HS1	PP	SC	SC2018	
Petrogenesis		Hydrothermal	Hydrothermal	Magmatic	Peridotite	Hydrothermal	Hydrothermal	HT Peridotite	Peridotite	Peridotite	Peridotite	Grt Peridotite	Peridotite	Peridotite	Peridotite	Peridotite	Peridotite	Peridotite	
Sample size		*Samples with detectable OH*											*No detectable OH*						
Length 1	(mm)	1.865	1.164	0.738	1.01	1.176	1.16	1.116	1.336	0.722	1.178	0.883	0.646	1.054	1.599	1.328	1.035	0.476	
Length 2	(mm)	3.154	1.565	1.17	1.411	1.482	1.485	1.794	1.485	0.803	1.731	0.98	1.126	1.91	1.627	1.398	1.825	2.457	
Length 3	(mm)	4.542	1.979	1.267	1.919	1.764	1.755	2.835	1.541	1.592	1.913	1.09	1.138	2.032	1.686	1.72	2.26	2.505	
Wavenumber[1,2] (cm^{-1})																			Band assignment[3]
Range I	3698	x	o	o	o	x	x	o	o	o	o	o	o	o	o	o	o	o	*Serpentine lamellae*
	3650	o	o	o	o	w	w	o	o	o	o	o	o	o	o	o	o	o	*Serpentine lamellae*
	3598	x	x	o	o	x	x	o	x	o	3612	x	o	o	o	o	o	o	Si vacancies
	3572	o	o	o	w	o	o	x	x	o	o	x	o	o	o	o	o	o	TiChu point defect
	3562	o	x	x	o	o	o	o	o	o	3568	o	o	o	o	o	o	o	Si vacancies[4]
	3542	o	x	o	o	o	o	o	x	o	x	x	o	o	o	o	o	o	Si vacancies
	3525	o	o	x	o	o	o	w	x	o	x	x	o	o	o	o	o	o	TiChu point defect
Range II	3485	x	3477	x	o	x	x	o	x	o	o	x	o	o	o	o	o	o	Si vacancies
	3402	o	o	o	o	o	o	o	o	o	o	o	o	o	o	o	o	o	*TiChu lamellae*
	3387	o	o	o	o	o	o	o	o	x	o	o	o	o	o	o	o	o	
	3355	o	o	x	x	o	o	w	x	x	x	x	o	o	o	o	o	o	Trivalent defects
	3327	o	o	x	x	o	o	w	x	x	x	x	o	o	o	o	o	o	Trivalent defects
	3230	o	o	w	o	o	o	w	o	o	o	x	o	o	o	o	o	o	Mg vacancies

[1] Wavenumber resolution ±4 cm^{-1}.

[2] OH band presence is indicated as x = present, w = weak, or o = absent. When the expected band is offset but corresponds to the same defect, the wavenumber is indicated directly.

[3] This compilation of OH band assignments in olivine is identical to Thoraval et al. (2019), and was previously established by Beran and Libowitzky (2006), Padrón-Navarta et al. (2014), and Jollands et al. (2015). Trivalent defect bands occur at 3353 cm^{-1} for Fe^{3+}, and 3358, 3328, and 3323 cm^{-1} for Cr^{3+} (Jollands et al., 2016). 'TiChu point defect' indicates the Ti and H associated defect $\{Ti_{Mg}^{\bullet\bullet}, (2H)_{Si}''\}^{\times}$, also called the titanium clinohumite-like point defect (Berry et al., 2005). TiChu lamellae = titanium clinohumite lamellae.

[4] Overlapping with 3553 cm^{-1} from TiChu point defects.

Table 2. Average major and minor element concentrations determined by semi-quantitative µXRF for each olivine.

wt%	SAP	MYA	LR	OLM	NW1	NW2	SAS41	SAS20	SAS21	LAZ	PA3	DMP2	DMP4	HS1	PP	SC	SC2018	SCO-2 (n=5)[1]
SiO_2	40.47	41.40	37.90	41.13	41.30	41.29	40.22	40.51	40.52	40.31	40.09	40.03	40.10	40.04	39.96	39.90	40.02	40.62
TiO_2	-	-	0.01	-	-	-	-	0.01	-	-	0.01	-	-	-	0.00	-	-	0.00
Al_2O_3	-	-	-	-	-	-	-	-	-	-	-	-	-	-	-	-	-	0.00
Cr_2O_3	-	-	-	-	-	-	-	-	-	0.02	-	0.01	0.02	-	-	-	-	-
FeO	9.11	5.77	15.58	6.74	6.03	6.30	10.44	8.88	8.82	9.93	11.14	10.65	9.93	10.55	10.20	10.64	10.55	9.83
MnO	0.14	0.13	0.17	0.09	0.17	0.18	0.13	0.13	0.12	0.13	0.13	0.14	0.12	0.14	0.18	0.15	0.15	0.11
MgO	48.94	51.64	43.28	50.90	51.53	51.33	47.57	49.07	49.04	48.09	46.91	47.53	48.33	47.54	48.10	47.56	47.59	48.76
CaO	0.02	0.07	0.24	0.05	0.13	0.02	0.11	0.04	0.13	0.07	0.08	0.10	0.07	0.19	0.09	0.20	0.14	0.11
Na_2O	-	-	-	-	-	-	-	-	-	-	-	-	-	-	-	-	-	-
NiO	0.36	0.42	0.38	0.42	0.23	0.24	0.43	0.43	0.45	0.43	0.47	0.42	0.41	0.43	0.38	0.43	0.44	0.43
Total	99.05	99.43	97.56	99.32	99.40	99.37	98.90	99.08	99.09	98.97	98.83	98.89	98.97	98.89	98.93	98.88	98.89	99.96*
O	4.000	4.000	4.000	4.000	4.000	4.000	4.000	4.000	4.000	4.000	4.000	4.000	4.000	4.000	4.000	4.000	4.000	4.000
Si	1.000	1.003	0.979	1.002	1.002	1.003	1.001	1.000	1.000	1.000	1.002	0.998	0.996	0.998	0.995	0.996	0.998	0.998
Ti	0.000	0.000	0.000	0.000	0.000	0.000	0.000	0.000	0.000	0.000	0.000	0.000	0.000	0.000	0.000	0.000	0.000	0.000
Al	0.000	0.000	0.000	0.000	0.000	0.000	0.000	0.000	0.000	0.000	0.000	0.000	0.000	0.000	0.000	0.000	0.000	0.001
Cr	0.000	0.000	0.000	0.000	0.000	0.000	0.000	0.000	0.000	0.000	0.000	0.000	0.000	0.000	0.000	0.000	0.000	0.000
Fe	0.188	0.117	0.337	0.137	0.122	0.128	0.217	0.183	0.182	0.206	0.233	0.222	0.206	0.220	0.212	0.222	0.220	0.204
Mn	0.003	0.003	0.004	0.002	0.004	0.004	0.003	0.003	0.003	0.003	0.003	0.003	0.002	0.003	0.004	0.003	0.003	0.002
Mg	1.802	1.865	1.667	1.848	1.863	1.858	1.766	1.805	1.804	1.779	1.748	1.767	1.789	1.767	1.785	1.769	1.769	1.786
Ca	0.001	0.002	0.007	0.001	0.003	0.001	0.003	0.001	0.003	0.002	0.002	0.003	0.002	0.005	0.002	0.005	0.004	0.003
Na	0.000	0.000	0.019	0.000	0.000	0.000	0.000	0.000	0.000	0.000	0.000	0.000	0.000	0.000	0.000	0.000	0.000	0.000
Ni	0.007	0.008	0.008	0.008	0.004	0.005	0.009	0.008	0.009	0.009	0.009	0.009	0.008	0.009	0.008	0.009	0.009	0.009
Sum cations	3.000	2.997	3.021	2.998	2.998	2.997	2.999	3.000	3.000	2.999	2.998	3.002	3.004	3.002	3.005	3.004	3.002	3.002
Fo%[2]	90.54	94.11	83.20	93.09	93.84	93.56	89.04	90.78	90.83	89.62	88.25	88.83	89.67	88.93	89.37	88.85	88.94	89.75

[1] In-house Standard, San Carlos Olivine, Mcquarie University (see Table S1).

[2] Fo% = 100 x Mg/(Fe+Mg).

* average of the 5 totals

Table 3. Hydrogen concentration in olivine specimens with detectable O-H only, and obtained by unpolarized ('unpo') and polarized ('po') FTIR using the frequency-dependent calibration of Paterson (1982; 'Pat') and the mineral-dependent calibration of Withers et al. (2012; 'W'). The average integrated absorbances normalized to sample thickness are compiled in Table S3, and integrations were performed in the 3650–3050 cm–1 wavenumber range.

Sample #	[OH] unpo1Pat	[OH] po2Pat	[OH] po 3W	[OH] po triplet_1 4W	[OH] po triplet_2 5W
	Concentration in ppm H by weight (= molar concentration in micro mole / g of olivine)*				
SAP	**3.1**	**3.3**	**4.5**	**4.5**	**4.5**
MYA	**0.6**	**0.7**	**1.0**	**1.2**	**1.2**
LR	**0.6**	**0.7**	**1.4**	**1.5**	**1.3**
OLM	**0.3**	**0.3**	**0.7**	**0.9**	**0.6**
NW1	**3.2**	**4.3**	**6.0**	**5.5**	**6.4**
NW2	**3.6**	**4.0**	**5.6**	**5.5**	**5.6**
SAS41	**0.2**	**0.3**	**0.8**	**0.8**	**0.8**
SAS20	**1.4**	**1.3**	**2.3**	**2.5**	**2.5**
SAS21	**0.6**	**0.7**	**1.8**	**1.9**	**1.7**
LAZ	**0.1**	**0.3**	**0.4**	**0.5**	**0.4**
PA3	**0.8**	**1.0**	**1.7**	**1.7**	**1.7**
	Concentration in ppm H_2O by weight				
SAP	28	30	41	41	40
MYA	5	6	9	10	10
LR1	5	6	12	13	12
OLM	3	3	6	8	6
NW1	29	39	54	49	58
NW2	32	36	50	50	51
SAS41	2	3	7	7	7
SAS20	13	12	21	22	22
SAS21	5	6	16	17	15
LAZ	1	3	4	4	3
Pa3	7	9	15	15	15
	Concentration in $H/10^6$ Si (= ppm H/Si)				
SAP	456	489	663	667	659
MYA	80	96	137	168	168
LR1	84	101	210	224	198
OLM	48	48	98	125	92
NW1	466	627	860	793	927
NW2	515	579	804	796	813
SAS41	33	49	117	113	123
SAS20	212	195	343	364	366
SAS21	81	98	267	279	252
LAZ	16	49	64	72	56
Pa3	115	148	253	249	255

1: Calculated from the average of 3 perpendicular unpolarized spectra, and the application of the calibration of Paterson (1982).

2: Calculated from the average of all six polarized spectra, acquired from 3 faces perpendicular to each other, and then times by a factor 3, followed by the application of the Paterson's calibration (1982)

3: Calculated from the average of all six polarized spectra, acquired from 3 faces perpendicular to each other, and then times by a factor 3, followed by the application of the calibration of Withers et al., (2012

4: Calculated from the summ of 3 polarized spectra perpendicular to each other (triplet 1) followed by the application of the calibration of Withers et al., (2012)

5: Calculated from the summ of 3 polarized spectra perpendicular to each other (triplet 2) followed by the application of the calibration of Withers et al., (2012)

* Since the molar weight of hydrogen equals 1, this is also giving the molar weight

Table 4. Minor, trace, and ultra-trace element concentrations (ppm) measured by LA-ICP-MS analyses of the olivine specimens (*n* is the number of the measurements and ±1SD the standard deviation; typical detection limits for each element are given in Table S2).

	SAP	***n* = 5**	**MYA**	***n* = 5**	**LR**	***n* = 5**	**OLM**	***n* = 5**	**NW1**	***n* = 5**	**NW2**	***n* = 5**	**SAS41**	***n* = 5**	**SAS20**	***n* = 5**	**SAS21**	***n* = 5**
ppm	*Avg*	*±1SD*	*Avg*	*±1SD*	*Avg*	*±1SD*	*Avg*	*±1SD*	*Avg*	*±1SD*	*Avg*	*±1SD*	*Avg*	*±1SD*	*Avg*	*±1SD*	*Avg*	*±1SD*
Li	12.61	*1.06*	0.71	*0.06*	1.89	*0.05*	1.32	*0.11*	1.73	*0.39*	9.02	*0.45*	1.61	*0.05*	2.32	*0.08*	1.34	*0.04*
Be	0.0067	*0.0069*	0.0015	*0.0007*	BDL	*BDL*	0.0037	*0.0000*	0.0030	-	BDL	*BDL*	BDL	*BDL*	BDL	*BDL*	0.0018	*0.0002*
B	61.26	*6.64*	2.96	*0.18*	1.29	*0.06*	1.31	*0.07*	101.38	*3.95*	109.45	*7.89*	1.22	*0.04*	1.44	*0.09*	1.24	*0.03*
Na	0.30	*0.22*	3.55	*0.48*	58.19	*0.99*	51.79	*4.56*	0.16	*0.11*	0.08	*0.04*	11.61	*0.12*	51.91	*0.67*	17.68	*0.37*
Al	0.92	*0.33*	13.00	*0.61*	224.90	*8.70*	8.24	*0.34*	0.66	*0.03*	0.66	*0.03*	21.00	*0.34*	52.22	*0.71*	155.92	*4.85*
P	17.09	*1.20*	10.72	*1.04*	71.52	*1.26*	12.22	*0.98*	15.92	*0.87*	16.00	*2.08*	18.29	*0.48*	27.62	*1.41*	13.65	*0.60*
Ca	40	*3*	79	*7*	1437	*61*	128	*15*	31	*2*	33	*2*	137	*10*	216	*6*	633	*37*
Sc	6.38	*0.60*	2.39	*0.01*	2.58	*0.05*	1.96	*0.03*	8.71	*0.93*	6.00	*0.99*	1.94	*0.02*	2.20	*0.02*	2.34	*0.03*
Ti	4.63	*0.23*	3.83	*0.11*	68.21	*1.37*	4.48	*0.29*	6.66	*0.29*	3.46	*0.29*	10.80	*0.29*	56.60	*0.29*	4.14	*0.29*
V	0.81	*0.08*	0.55	*0.02*	6.86	*0.10*	0.92	*0.06*	0.14	*0.01*	0.15	*0.04*	1.33	*0.03*	2.79	*0.05*	6.16	*0.10*
Cr	74.0	*12.6*	11.3	*0.3*	440.8	*6.4*	94.8	*14.4*	26.0	*1.2*	30.7	*8.6*	21.3	*0.3*	127.8	*1.1*	456.1	*6.0*
Mn	1119	*16*	937	*16*	1390	*20*	706	*2*	1375	*22*	1377	*50*	1084	*16*	979	*8*	997	*8*
Co	139.6	*1.9*	138.4	*3.2*	170.6	*3.0*	124.7	*1.0*	157.3	*2.0*	159.1	*2.4*	146.8	*1.2*	139.9	*2.5*	144.4	*2.4*
Ni	2676	*16*	3228	*76*	2742	*52*	3078	*26*	1697	*30*	1699	*37*	3091	*12*	3133	*26*	3229	*40*
Cu	0.13	*0.07*	0.54	*0.01*	4.24	*0.11*	0.39	*0.02*	0.011	*0.007*	0.005	*0.002*	0.47	*0.01*	0.46	*0.05*	2.13	*0.02*
Zn	21.00	*0.54*	38.88	*0.96*	91.51	*2.19*	34.68	*0.40*	15.52	*0.35*	16.08	*0.26*	38.86	*0.44*	50.80	*0.63*	48.73	*0.66*
Ga	0.0102	*0.0031*	0.0075	*0.0012*	0.1708	*0.0131*	0.0117	*0.0019*	0.0095	*0.0019*	0.0096	*0.0021*	0.0146	*0.0028*	0.0343	*0.0066*	0.0446	*0.0046*
Ge	1.38	*0.05*	0.96	*0.07*	1.75	*0.06*	0.91	*0.03*	0.98	*0.06*	1.04	*0.05*	1.35	*0.05*	1.13	*0.03*	1.17	*0.05*
Rb	0.0133	*0.0080*	0.0020	*0.0004*	BDL	*BDL*	0.0024	*0.0004*	0.0034	BDL	BDL	*BDL*	BDL	*BDL*	0.0024	*0.0006*	0.0032	*0.0011*
Sr	0.0019	*0.0016*	0.0006	*0.0003*	0.0046	*0.0015*	0.0100	*0.0072*	0.0010	*0.0013*	0.0005	BDL	0.0013	*0.0009*	0.0006	*0.0004*	0.0474	*0.0011*
Y	0.0424	*0.0050*	0.0012	*0.0004*	0.1055	*0.0056*	0.0353	*0.0043*	0.0484	*0.0019*	0.0472	*0.0180*	0.0080	*0.0011*	0.0093	*0.0014*	0.0014	*0.0003*
Zr	0.0073	*0.0025*	0.0053	*0.0023*	0.0562	*0.0036*	0.0191	*0.0049*	0.0028	*0.0010*	0.0006	*0.0003*	0.0007	*0.0004*	0.3390	*0.0210*	0.0070	*0.0009*
Nb	0.0017	*0.0010*	0.0010	*0.0007*	0.0003	*0.0002*	0.0286	*0.0156*	0.0004	*0.0002*	BDL	*BDL*	0.0002	-	0.0235	*0.0032*	0.0086	*0.0022*
Mo	0.0216	*0.0079*	0.0107	*0.0021*	0.0156	*0.0031*	0.0065	*0.0034*	0.0158	*0.0035*	0.0158	*0.0049*	0.0156	*0.0074*	0.0149	*0.0043*	0.0126	*0.0024*
Cs	0.0056	*0.0042*	BDL	*BDL*	BDL	*BDL*	0.0007	*0.0001*	BDL	*BDL*	BDL	*BDL*	BDL	*BDL*	BDL	*BDL*	BDL	*BDL*
Ba	0.0156	*0.0099*	0.0023	*0.0013*	0.0004	*0.0001*	0.0039	*0.0035*	0.0019	*0.0015*	0.0015	*0.0006*	0.0035	*0.0034*	0.0017	*0.0013*	0.0028	*0.0014*
La	0.00125	*0.00095*	0.00019	*0.00017*	0.00019	*0.00009*	0.00119	*0.00120*	0.00057	*0.00060*	BDL	*BDL*	0.00013	*0.00008*	0.00011	*0.00004*	0.00013	*0.00012*
Ce	0.0034	*0.0010*	0.0004	*0.0003*	0.0003	*0.0002*	0.0020	*0.0021*	0.0001	*0.0000*	0.0001	*0.0000*	0.0001	*0.0001*	0.0003	*0.0001*	0.0003	*0.0001*
Pr	0.00943	*0.00912*	BDL	*BDL*	0.00008	*0.00002*	0.00028	*0.00025*	0.00010	*0.00009*	BDL	*BDL*	BDL	*BDL*	BDL	*BDL*	BDL	*BDL*
Nd	0.00560	*0.00315*	BDL	*BDL*	0.00061	*0.00023*	BDL	*BDL*	BDL	*BDL*	BDL	*BDL*	BDL	*BDL*	0.00034	*0.00014*	0.00053	*0.00039*
Sm	0.00133	*0.00064*	BDL	*BDL*	0.00065	*0.00022*	0.00039	*0.00026*	BDL	*BDL*	BDL	*BDL*	BDL	*BDL*	BDL	*BDL*	BDL	*BDL*
Eu	0.00169	*0.00184*	BDL	*BDL*	0.00055	*0.00021*	0.00023	*0.00015*	BDL	*BDL*	BDL	*BDL*	BDL	*BDL*	0.00010	*0.00003*	0.00008	*0.00003*
Gd	0.00397	*0.00263*	0.00029	*0.00011*	0.00316	*0.00030*	0.00093	*0.00042*	BDL	*BDL*	0.00025	*0.00008*	BDL	*BDL*	0.00048	*0.00029*	0.00033	*0.00017*
Tb	0.00040	*0.00009*	0.00005	*0.00003*	0.00104	*0.00028*	0.00035	*0.00016*	0.00010	*0.00007*	0.00006	*0.00003*	BDL	*BDL*	0.00012	*0.00004*	0.00005	*0.00003*
Dy	0.00428	*0.00117*	0.00024	*0.00008*	0.01210	*0.00202*	0.00443	*0.00069*	0.00172	*0.00073*	0.00046	*0.00016*	0.00036	*0.00022*	0.00105	*0.00055*	0.00044	*0.00040*
Ho	0.00251	*0.00066*	0.00013	*0.00010*	0.00358	*0.00042*	0.00119	*0.00050*	0.00132	*0.00028*	0.00117	*0.00023*	0.00021	*0.00014*	0.00026	*0.00008*	0.00017	*0.00011*
Er	0.0153	*0.0023*	0.0006	*0.0006*	0.0138	*0.0020*	0.0055	*0.0009*	0.0135	*0.0030*	0.0145	*0.0046*	0.0012	*0.0003*	0.0013	*0.0003*	0.0005	*0.0004*
Tm	0.00620	*0.00085*	0.00007	*0.00002*	0.00260	*0.00049*	0.00124	*0.00013*	0.00515	*0.00068*	0.00532	*0.00117*	0.00041	*0.00005*	0.00031	*0.00016*	0.00010	*0.00005*
Yb	0.0710	*0.0130*	0.0014	*0.0010*	0.0277	*0.0039*	0.0114	*0.0019*	0.0583	*0.0076*	0.0576	*0.0057*	0.0054	*0.0015*	0.0030	*0.0004*	0.0011	*0.0003*
Lu	0.01333	*0.00356*	0.00044	*0.00014*	0.00540	*0.00111*	0.00222	*0.00024*	0.01473	*0.00362*	0.01288	*0.00149*	0.00223	*0.00050*	0.00045	*0.00012*	0.00025	*0.00009*
Hf	0.00222	*0.00214*	0.00048	*0.00026*	0.00145	*0.00089*	0.00029	*0.00016*	0.00037	*0.00027*	BDL	*BDL*	0.00027	*0.00015*	0.00553	*0.00159*	0.00045	*0.00043*
Ta	0.00280	*0.00180*	0.00008	*0.00008*	0.00146	*0.00049*	0.00252	*0.00219*	0.00128	*0.00104*	0.00037	*0.00025*	0.00835	*0.00766*	0.00162	*0.00064*	0.00727	*0.00658*
Pb	0.0313	*0.0395*	0.0130	*0.0137*	0.0039	*0.0017*	0.0032	*0.0014*	0.0041	*0.0018*	0.0087	*0.0071*	0.0061	*0.0033*	0.0043	*0.0019*	0.0044	*0.0031*
Bi	0.01501	*0.00789*	0.00067	*0.00031*	0.00060	*0.00024*	0.00199	*0.00154*	0.00180	*0.00104*	0.00140	*0.00052*	0.00127	*0.00117*	0.00157	*0.00137*	0.00042	*0.00041*
Th	0.00162	*0.00129*	0.00030	*0.00010*	BDL	*BDL*	0.00085	*0.00105*	0.00018	*0.00018*	0.00021	*0.00023*	0.00013	*0.00007*	0.00029	*0.00029*	0.00025	*0.00018*
U	0.00526	*0.00408*	0.00028	*0.00023*	0.00013	*0.00006*	0.00060	*0.00077*	0.00028	*0.00043*	0.00013	*0.00009*	0.00009	*0.00002*	0.00014	*0.00008*	0.00016	*0.00011*

Table 4 (continued)

	LAZ	***n = 5***	**Pa3**	***n = 5***	**DMP2**	***n = 5***	**DMP4**	***n = 5***	**HS1**	***n = 5***	**PP**	***n = 5***	**SC**	***n = 5***	**SC2018**	***n = 5***	**SCO-1**	***n = 6***
ppm	Avg	*±1SD*	Avg	*±1SD*	Avg	*±1SD*	Avg	*±1SD*	Avg	*±1SD*	Avg	*±1SD*	Avg	*±1SD*	Avg	*±1SD*	Avg	*±1SD*
Li	1.37	*0.05*	2.00	*0.11*	1.57	*0.10*	1.77	*0.05*	3.72	*0.10*	1.78	*0.04*	1.59	*0.05*	1.62	*0.06*	1.77	*0.10*
Be	BDL	*BDL*	0.0027	*0.0019*	BDL	*BDL*	BDL	*BDL*	0.0036	*0.0021*	0.0021	*0.0010*	0.0022	*0.0019*	BDL	*BDL*	BDL	*BDL*
B	2.18	*0.19*	1.30	*0.10*	1.89	*0.16*	1.38	*0.10*	1.84	*0.11*	1.56	*0.13*	1.16	*0.11*	1.34	*0.06*	1.36	*0.11*
Na	10.09	*0.34*	63.74	*1.79*	28.51	*0.71*	30.41	*0.90*	74.61	*1.92*	55.77	*1.13*	19.41	*0.63*	19.36	*0.32*	41.58	*3.13*
Al	43.15	*1.31*	120.39	*4.78*	96.46	*7.30*	59.13	*1.26*	84.88	*4.28*	96.94	*2.90*	93.09	*1.35*	94.69	*1.99*	72.95	*1.26*
P	13.68	*1.28*	31.56	*3.32*	19.03	*1.08*	11.41	*0.60*	12.81	*0.32*	37.01	*1.41*	21.67	*0.69*	22.23	*0.70*	11.14	*0.87*
Ca	257	*14*	382	*7*	397	*22*	319	*14*	464	*23*	396	*28*	580	*26*	601	*31*	436	*31*
Sc	3.17	*0.10*	2.10	*0.03*	3.03	*0.04*	3.09	*0.07*	3.00	*0.07*	2.62	*0.04*	2.40	*0.03*	2.42	*0.02*	2.53	*0.16*
Ti	14.92	*0.44*	41.16	*1.04*	16.39	*0.65*	7.79	*0.25*	9.97	*0.25*	18.20	*0.25*	12.51	*0.25*	12.39	*0.25*	9.30	*0.46*
V	1.91	*0.06*	4.95	*0.05*	3.42	*0.10*	3.27	*0.05*	4.07	*0.04*	3.42	*0.05*	3.00	*0.06*	2.93	*0.06*	3.07	*0.04*
Cr	52.6	*0.9*	133.4	*0.8*	80.4	*2.5*	132.3	*3.7*	223.3	*5.9*	132.6	*1.0*	163.4	*2.6*	160.8	*1.7*	136.7	*1.6*
Mn	1027	*6*	985	*12*	1065	*28*	1071	*26*	1070	*31*	1068	*14*	1145	*12*	1133	*7*	1017	*17*
Co	149.2	*1.1*	150.0	*2.9*	144.2	*3.2*	149.2	*4.9*	143.2	*3.3*	142.1	*2.1*	151.6	*1.3*	150.7	*2.4*	145.6	*1.6*
Ni	3306	*9*	3169	*55*	3049	*60*	3093	*84*	3070	*98*	2960	*33*	2949	*36*	2924	*28*	3112	*42*
Cu	1.05	*0.01*	3.03	*0.09*	1.35	*0.09*	1.39	*0.05*	0.33	*0.01*	2.11	*0.05*	1.50	*0.03*	1.49	*0.02*	0.85	*0.02*
Zn	1.05	*0.01*	67.50	*1.66*	1.35	*0.09*	1.39	*0.05*	0.33	*0.01*	48.70	*1.13*	50.61	*1.31*	50.42	*0.68*	50.38	*0.47*
Ga	0.0270	*0.0042*	0.1193	*0.0080*	0.0398	*0.0025*	0.0301	*0.0026*	0.0472	*0.0068*	0.0466	*0.0039*	0.0402	*0.0052*	0.0430	*0.0043*	0.0338	*0.0030*
Ge	1.38	*0.03*	1.25	*0.03*	1.27	*0.05*	1.44	*0.07*	1.60	*0.04*	1.38	*0.05*	1.61	*0.08*	1.59	*0.04*	1.34	*0.04*
Rb	0.0031	*0.0024*	BDL	*BDL*	BDL	*BDL*	BDL	*BDL*	0.0031	*0.0022*	0.0025	*0.0013*	0.0016	*0.0004*	0.0021	*0.0006*	0.0019	*0.0003*
Sr	0.0014	*0.0006*	0.0013	*0.0012*	0.0004	*0.0003*	0.0007	*0.0004*	0.0058	*0.0005*	0.0036	*0.0015*	0.0011	*0.0005*	0.0021	*0.0012*	0.0007	*0.0003*
Y	0.0032	*0.0013*	0.0066	*0.0012*	0.0226	*0.0019*	0.0068	*0.0010*	0.0149	*0.0026*	0.0276	*0.0027*	0.0091	*0.0017*	0.0084	*0.0024*	0.0315	*0.0016*
Zr	0.1415	*0.0746*	0.0156	*0.0020*	0.0041	*0.0006*	0.0091	*0.0009*	0.0480	*0.0117*	0.0953	*0.0876*	0.0151	*0.0042*	0.0158	*0.0045*	0.0638	*0.0039*
Nb	0.0058	*0.0019*	0.0061	*0.0011*	0.0010	*0.0004*	0.0012	*0.0002*	0.0055	*0.0016*	0.0076	*0.0010*	0.0013	*0.0003*	0.0012	*0.0003*	0.0021	*0.0010*
Mo	0.0212	*0.0126*	0.0118	*0.0035*	0.0113	*0.0028*	0.0134	*0.0016*	0.0158	*0.0033*	0.0137	*0.0028*	0.0129	*0.0063*	0.0136	*0.0015*	0.0094	*0.0020*
Cs	0.0010	*0.0006*	BDL	*BDL*	BDL	*BDL*	BDL	*BDL*	0.0012	*0.0007*	0.0013	*0.0001*	0.0010	*BDL*	BDL	*BDL*	BDL	*BDL*
Ba	0.0044	*0.0022*	0.0017	*0.0010*	0.0020	*0.0020*	0.0081	*0.0082*	0.0023	*0.0017*	0.0018	*0.0010*	0.0023	*0.0015*	0.0012	*0.0005*	0.0032	*0.0012*
La	0.00115	*0.00181*	0.00030	*0.00018*	0.00025	*0.00015*	0.00009	*0.00004*	0.00103	*0.00149*	0.00049	*0.00033*	0.00037	*0.00037*	0.00021	*0.00018*	0.00031	*0.00041*
Ce	0.0023	*0.0021*	0.0002	*0.0001*	0.0001	*0.0000*	0.0001	*0.0000*	0.0004	*0.0003*	0.0005	*0.0003*	0.0002	*0.0001*	0.0002	*0.0001*	0.0006	*0.0007*
Pr	0.00021	*0.00017*	0.00006	*0.00002*	0.00008	*0.00004*	BDL	*BDL*	0.00016	*0.00013*	0.00008	*0.00002*	BDL	*BDL*	0.00005	*0.00002*	0.00006	*0.00003*
Nd	0.0010	*0.0006*	0.00083	*0.00105*	0.0008	*0.0001*	0.0003	*0.0001*	0.00074	*0.00064*	0.00059	*0.00044*	0.00025	*0.00011*	0.00039	*0.00012*	0.0003	*0.0001*
Sm	0.00038	*0.00026*	BDL	*BDL*	BDL	*BDL*	BDL	*BDL*	0.00046	*0.00027*	BDL	*BDL*	BDL	*BDL*	BDL	*BDL*	BDL	*BDL*
Eu	0.00014	*0.00006*	BDL	*BDL*	BDL	*BDL*	BDL	*BDL*	0.00018	*0.00010*	0.00023	*0.00015*	BDL	*BDL*	BDL	*BDL*	0.00010	*0.00004*
Gd	0.00075	*0.00069*	BDL	*BDL*	BDL	*BDL*	BDL	*BDL*	0.00074	*0.00019*	0.00077	*0.00068*	0.00029	*0.00014*	0.00024	*0.00015*	0.00046	*0.00040*
Tb	0.00013	*0.00007*	BDL	*BDL*	0.00010	*0.00005*	0.00012	*0.00010*	0.00023	*0.00006*	0.00020	*0.00020*	BDL	*BDL*	BDL	*BDL*	0.00019	*0.00015*
Dy	0.00115	*0.00082*	0.00042	*0.00023*	0.00116	*0.00029*	0.00046	*0.00019*	0.00278	*0.00189*	0.00252	*0.00112*	0.00070	*0.00054*	0.00029	*0.00021*	0.00217	*0.00096*
Ho	0.00026	*0.00011*	0.00011	*0.00005*	0.00081	*0.00026*	0.00016	*0.00010*	0.00059	*0.00010*	0.00075	*0.00021*	0.00017	*0.00009*	0.00017	*0.00008*	0.00085	*0.00033*
Er	0.0011	*0.0007*	0.0005	*0.0002*	0.0038	*0.0008*	0.0009	*0.0002*	0.0030	*0.0008*	0.0053	*0.0014*	0.0011	*0.0002*	0.0012	*0.0006*	0.0049	*0.0014*
Tm	0.00027	*0.00022*	0.00010	*0.00004*	0.00077	*0.00021*	0.00050	*0.00014*	0.00070	*0.00037*	0.00090	*0.00018*	0.00047	*0.00010*	0.00026	*0.00016*	0.00109	*0.00018*
Yb	0.0030	*0.0010*	0.0014	*0.0011*	0.0143	*0.0025*	0.0046	*0.0013*	0.0058	*0.0017*	0.0105	*0.0029*	0.0069	*0.0007*	0.0048	*0.0019*	0.0092	*0.0020*
Lu	0.00105	*0.00035*	0.00042	*0.00033*	0.00335	*0.00059*	0.00138	*0.00024*	0.00209	*0.00051*	0.00382	*0.00090*	0.00144	*0.00012*	0.00135	*0.00027*	0.00291	*0.00097*
Hf	0.00553	*0.00441*	0.00094	*0.00126*	BDL	*BDL*	BDL	*BDL*	0.00082	*0.00026*	0.00264	*0.00291*	0.00032	*0.00013*	0.00049	*0.00035*	0.00144	*0.00095*
Ta	0.00239	*0.00138*	0.00053	*0.00022*	0.00101	*0.00080*	0.00651	*0.00409*	0.00280	*0.00184*	0.00180	*0.00090*	0.00062	*0.00057*	0.00057	*0.00050*	0.00029	*0.00022*
Pb	0.0047	*0.0017*	0.0064	*0.0029*	0.0042	*0.0021*	0.0031	*0.0016*	0.0059	*0.0044*	0.0032	*0.0012*	0.0052	*0.0049*	0.0029	*0.0004*	0.0251	*0.0095*
Bi	0.00146	*0.00106*	0.00182	*0.00135*	0.00090	*0.00042*	0.00035	*0.00021*	0.00389	*0.00258*	0.00134	*0.00056*	0.00145	*0.00125*	0.00074	*0.00046*	0.00057	*0.00039*
Th	0.00107	*0.00103*	0.00024	*0.00023*	0.00006	*0.00005*	0.00004	*0.00004*	0.00034	*0.00022*	0.00026	*0.00032*	0.00033	*0.00031*	BDL	*BDL*	0.00022	*0.00021*
U	0.00236	*0.00261*	0.00079	*0.00050*	0.00024	*0.00021*	BDL	*BDL*	0.00043	*0.00038*	0.00032	*0.00030*	BDL	*BDL*	BDL	*BDL*	BDL	*BDL*

Hydrogen, trace and ultra-trace elements distribution in natural olivines

Sylvie DEMOUCHY[1,*] & Olivier ALARD[1,2]

[1]Géosciences Montpellier, Université de Montpellier & CNRS, 34095 Montpellier, France.

[2] Department of Earth and Planetary Science, Macquarie University, Sydney NSW 2109, Australia.

Supplementary materials

Fig. 1S. (a) Photography of olivine specimens during cutting and polishing preparations step, from left to right, Norway, Sapat, San Carlos#1, #2, #3, La Réunion ; (b) Olivine specimens glue on glass section prior to X-ray fluorescence mapping and Laser ablation inductively coupled plasma mass spectrometry. One square is 5 mm.

(a)

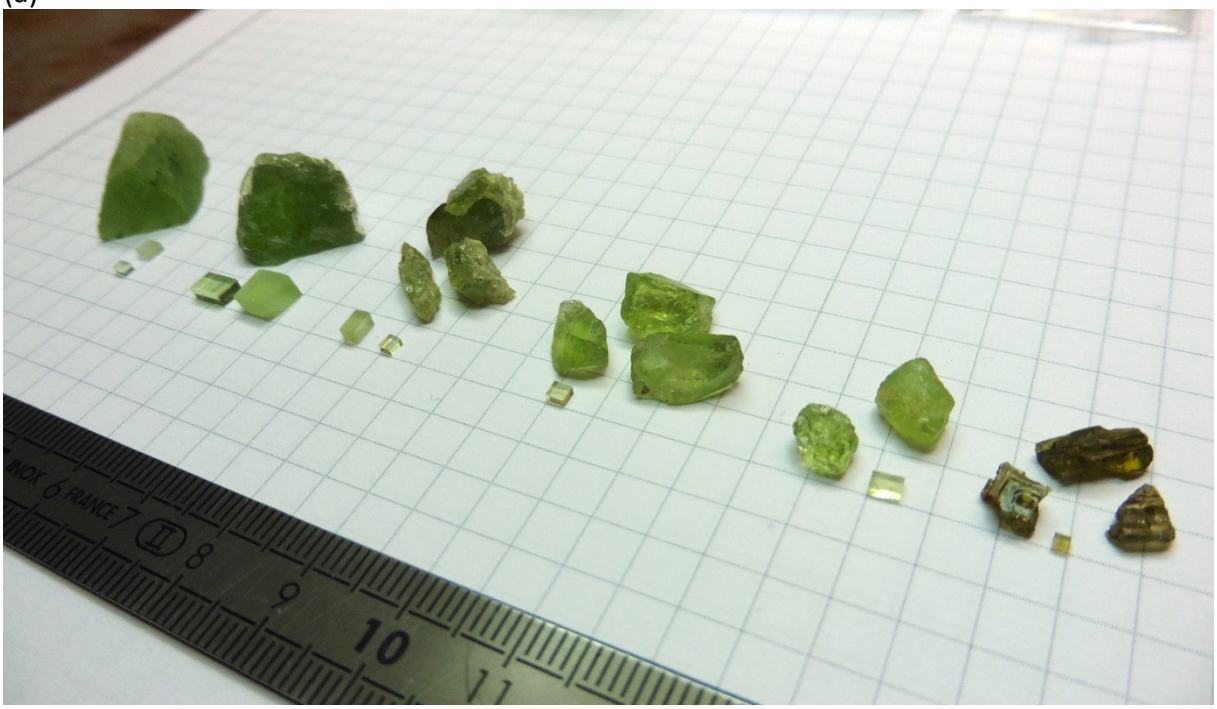

(b)

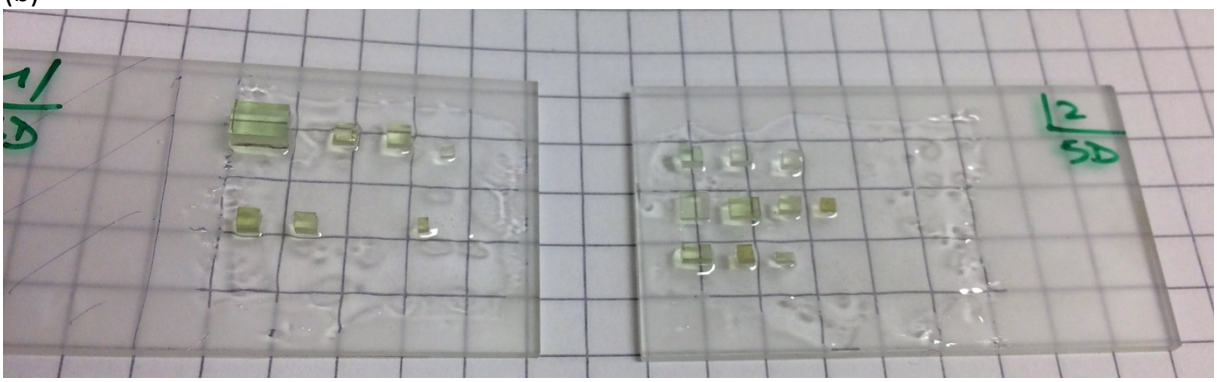

Fig. S2. Sets of FTIR spectra of olivines not presented in the main text: (a) SAP, (b) MYA, (c) LR, (d) OLM, (e) NW1 and NW2, (f) SAS41, SAS20, and SAS21, (g) LAZ, (h) SC2018 and SC, and (i) HS1, PP, and DMP. All spectra are normalized to 1 cm thickness.

Demouchy and Alard
Figure S1

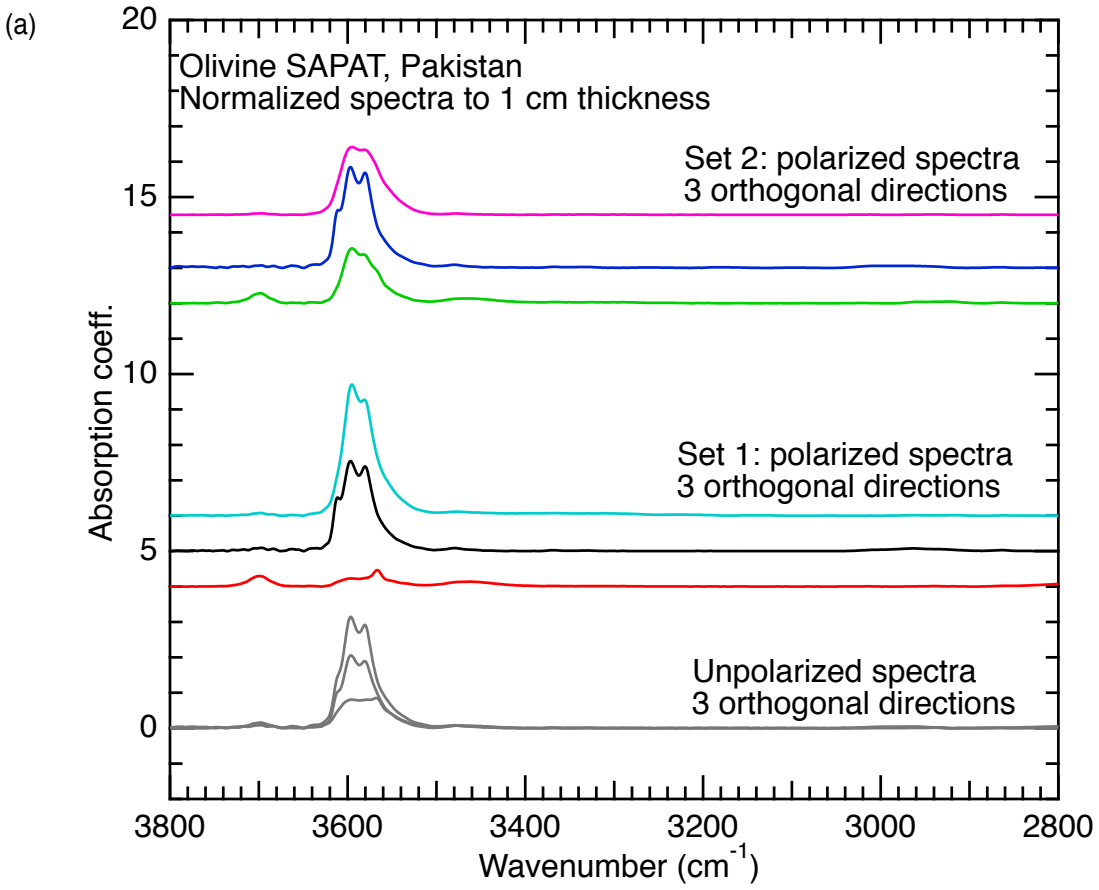

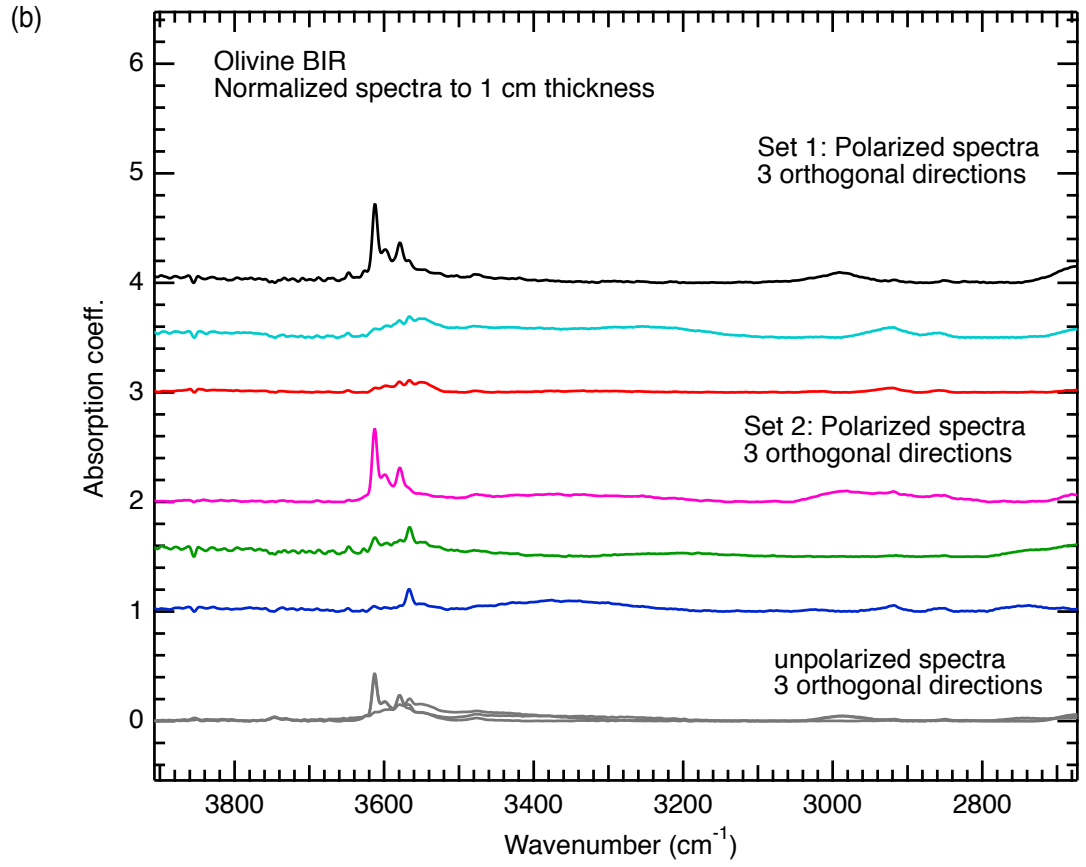

Demouchy and Alard
Fig. S1 (conitnued)

(c)

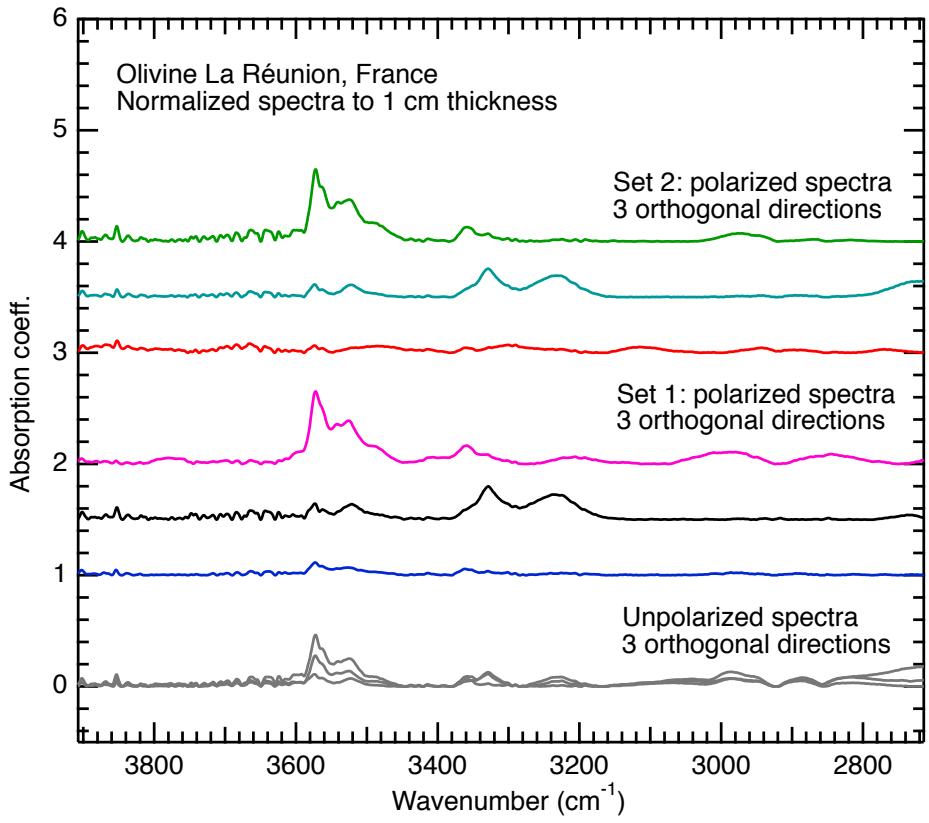

(d)

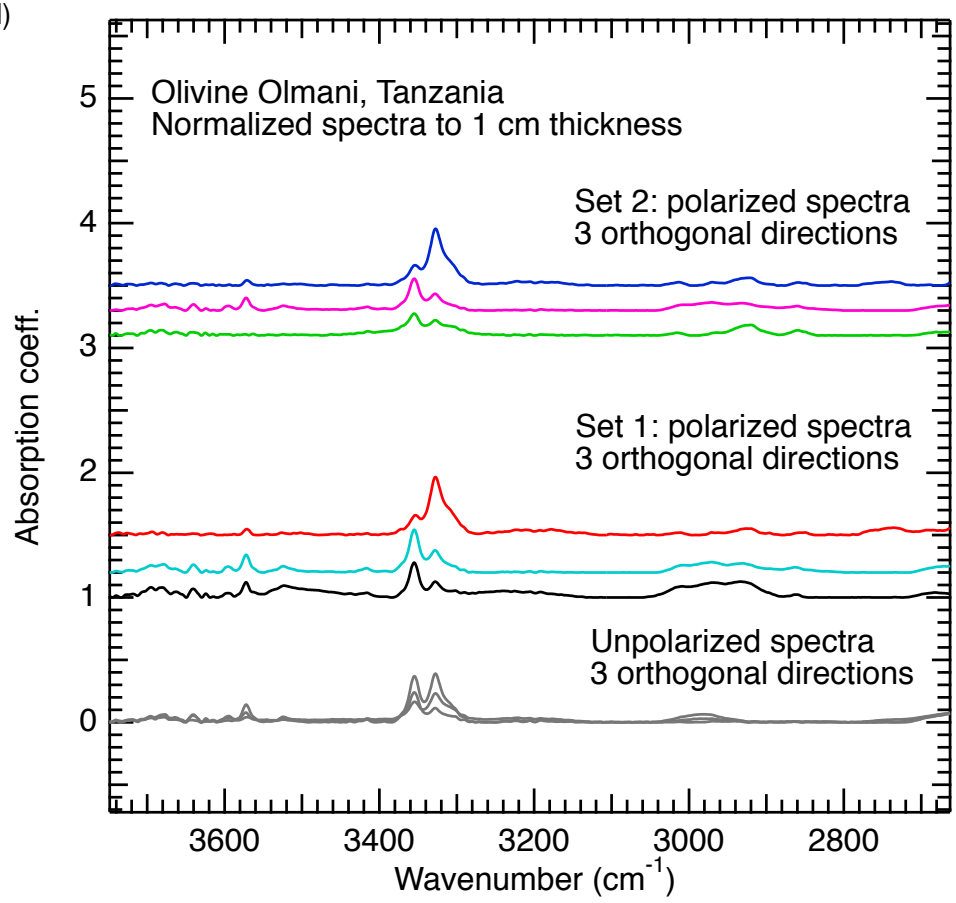

Demouchy and Alard
Fig. S1 (continued)

(e)

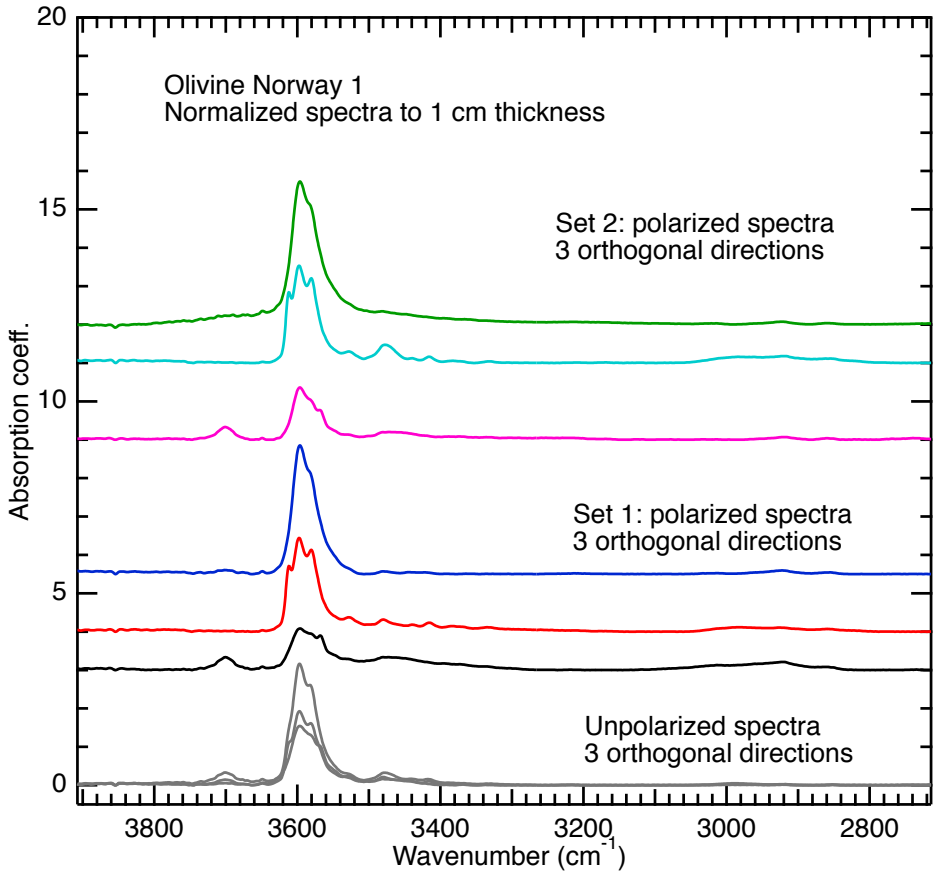

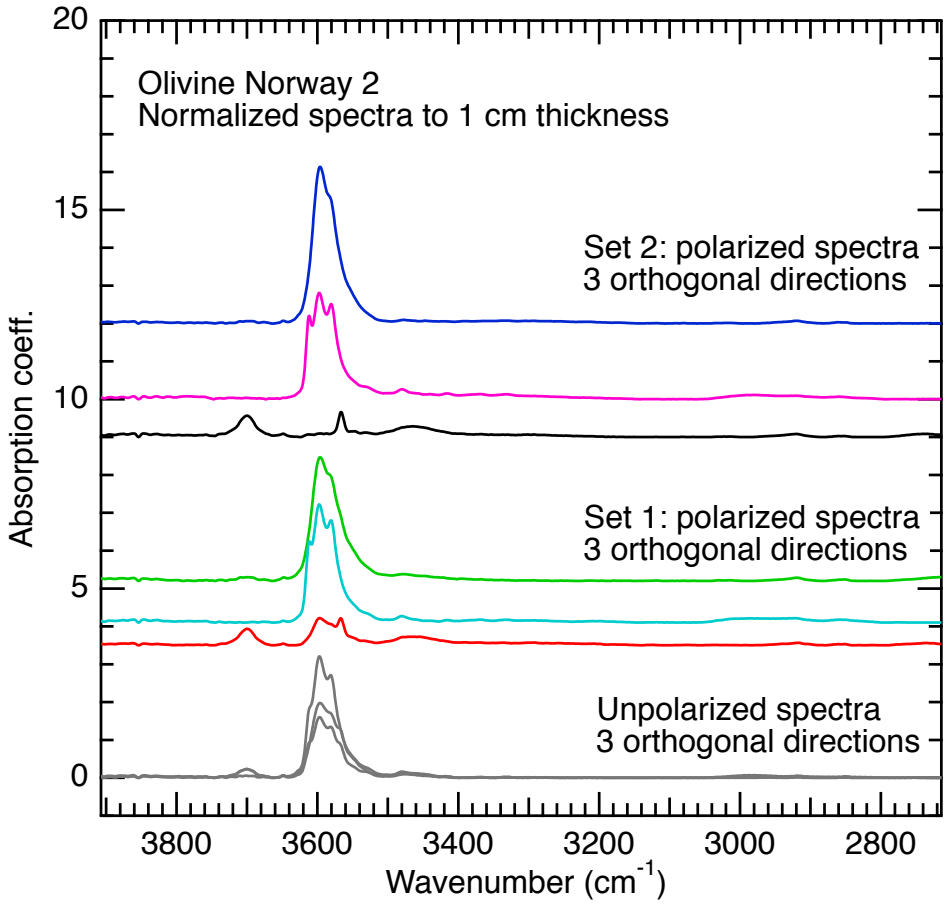

Demouchy and Alard
Fig. S1 (continued)

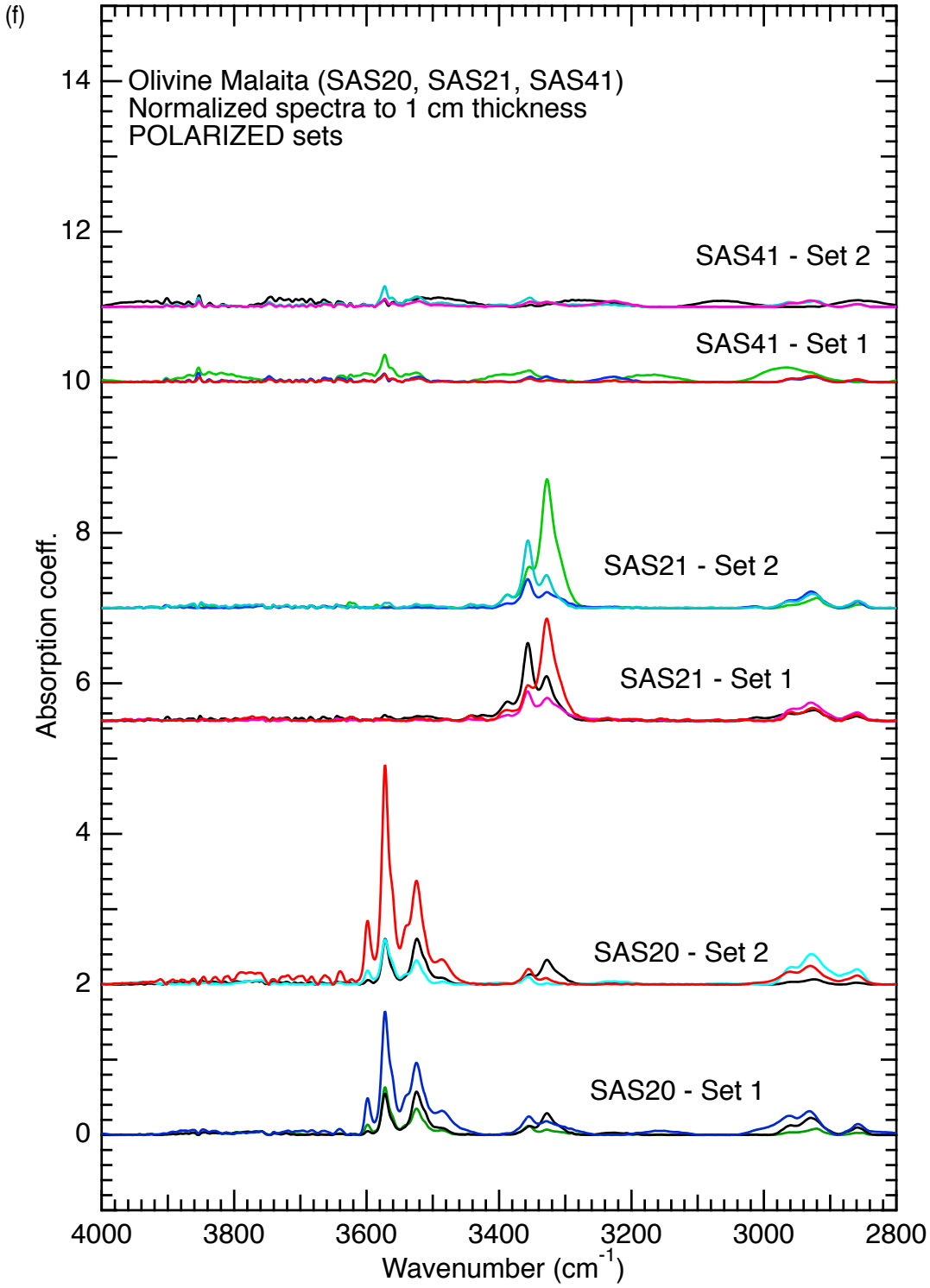

Demouchy and Alard
Fig. S1 (continued)

(g)

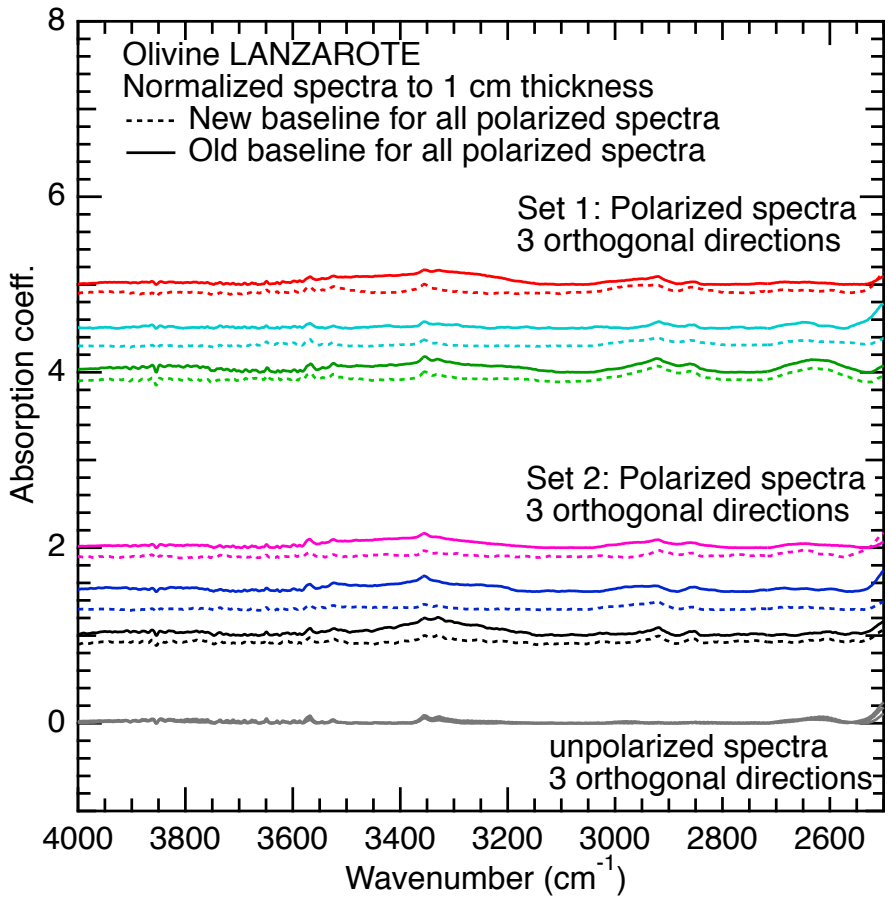

(h)

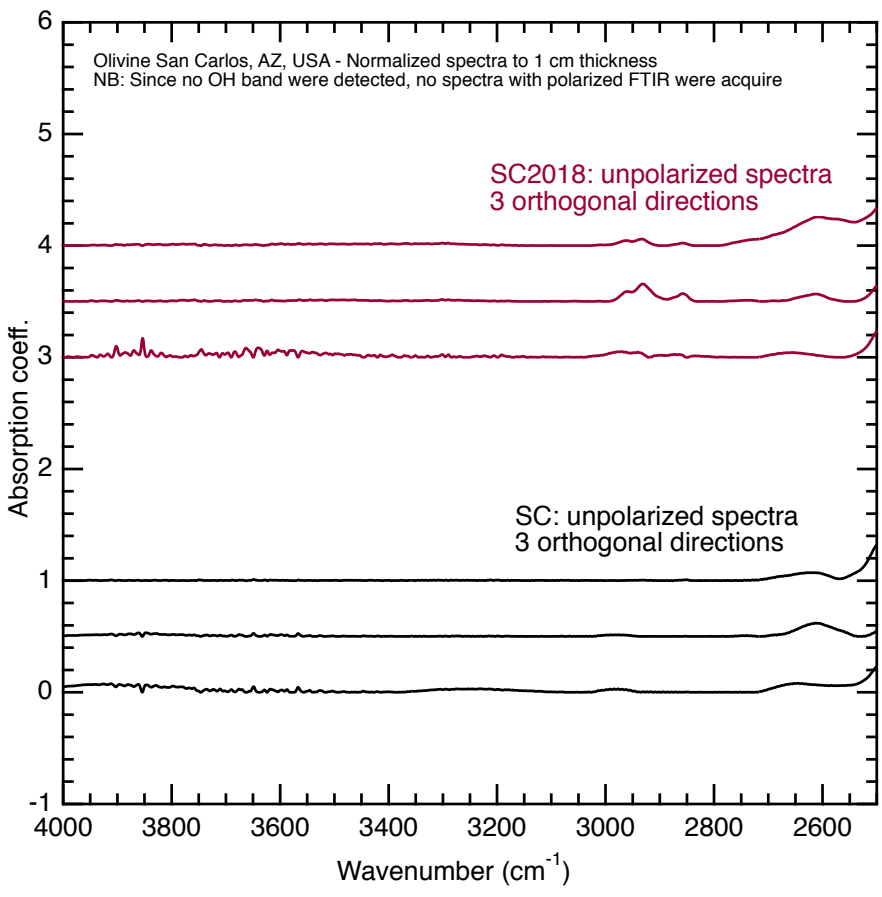

Demouchy and Alard
Fig S1. (continued)

(i)

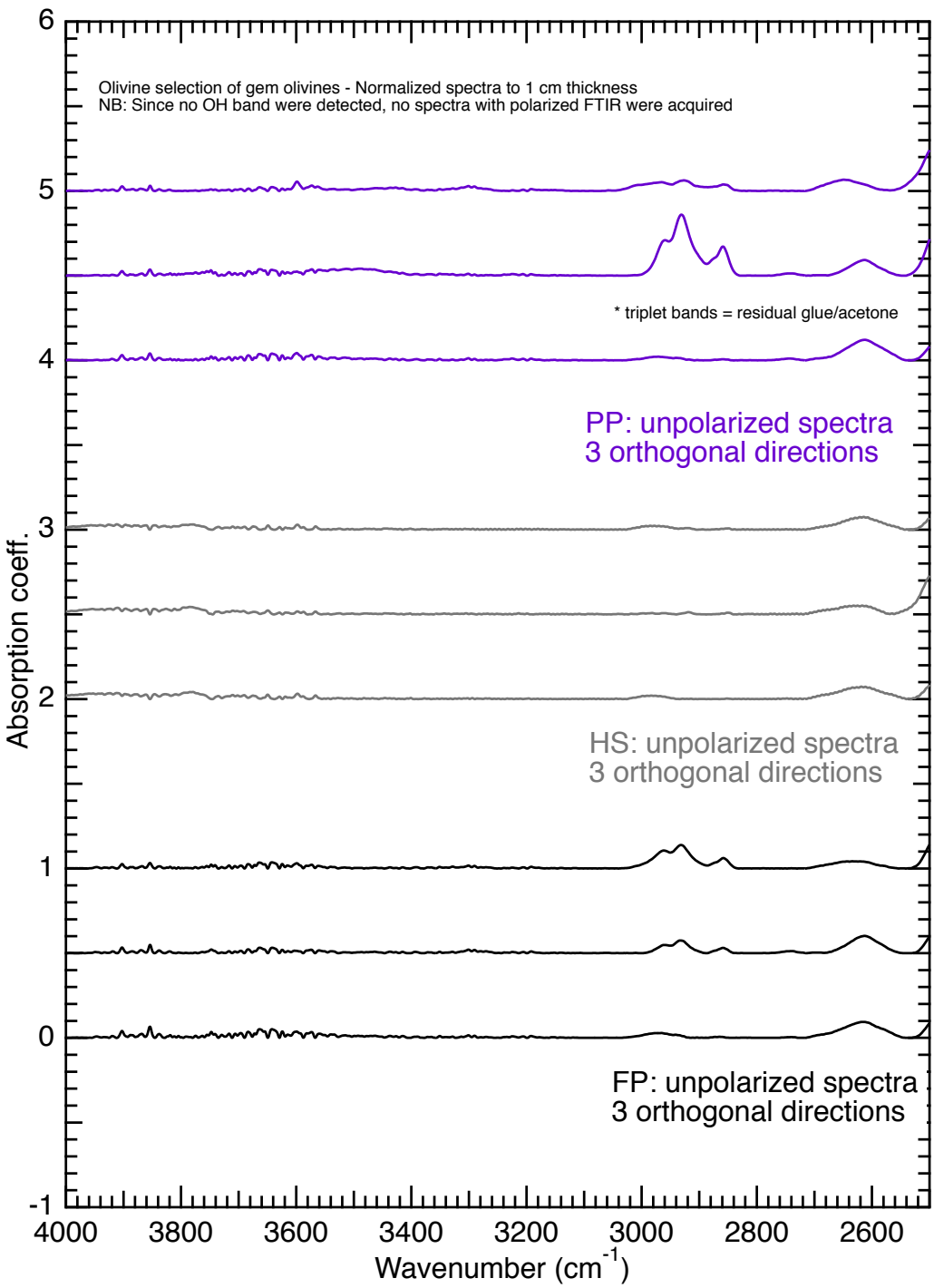

Fig. S3. Integrated absorbance distributions across (a) SAS20 and (b) NW1 as representative of the homogeneous distributions observed across all olivine specimens except Pa3.

Demouchy and Alard
Fig. S2

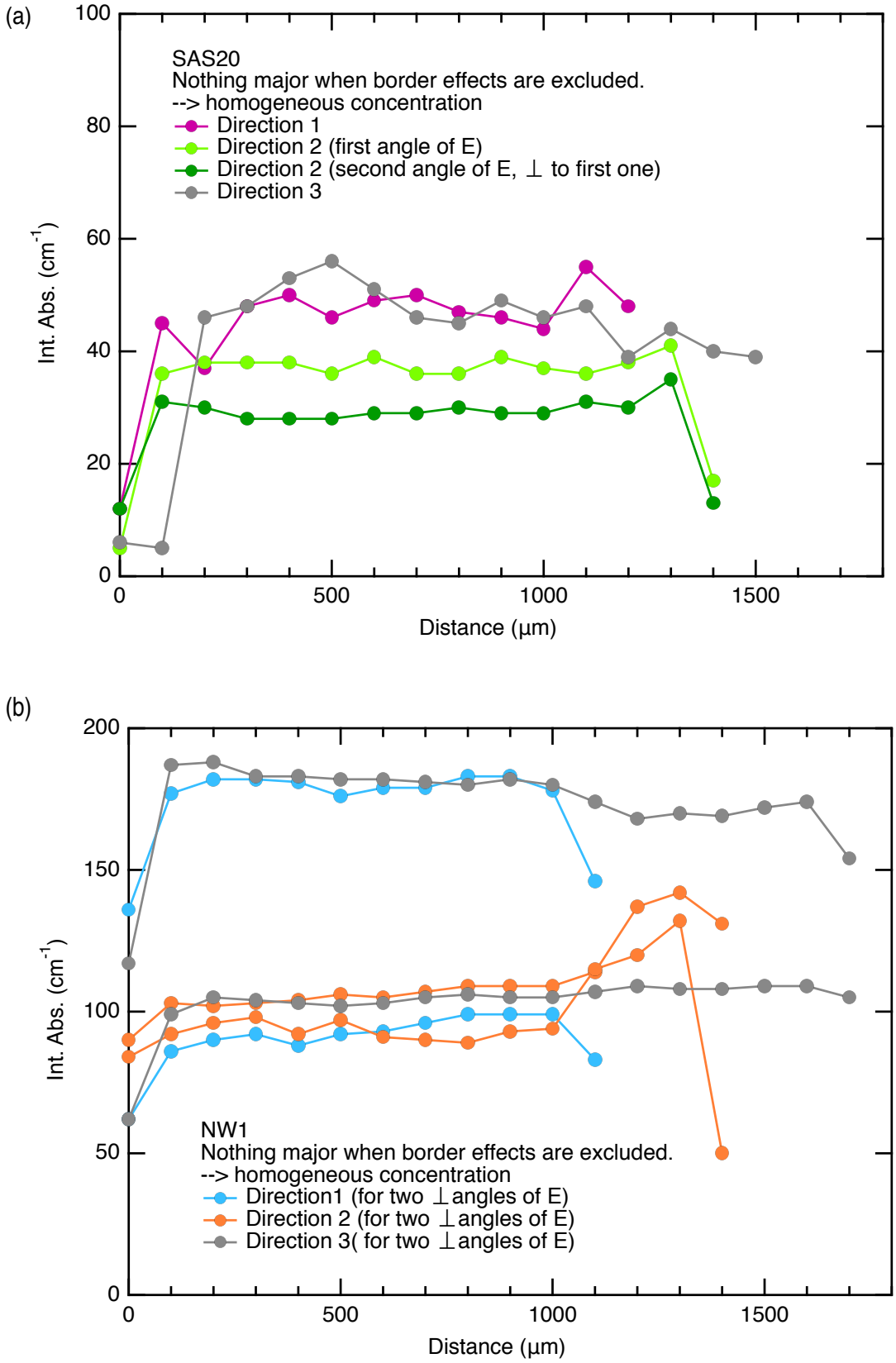

Fig. S4. Deconvolution details for the samples LR, LAZ, PA3, SAS20, SAS41, performed with the multipeak fitting package of IGOR PRO™ (https://www.wavemetrics.com/products/igorpro).

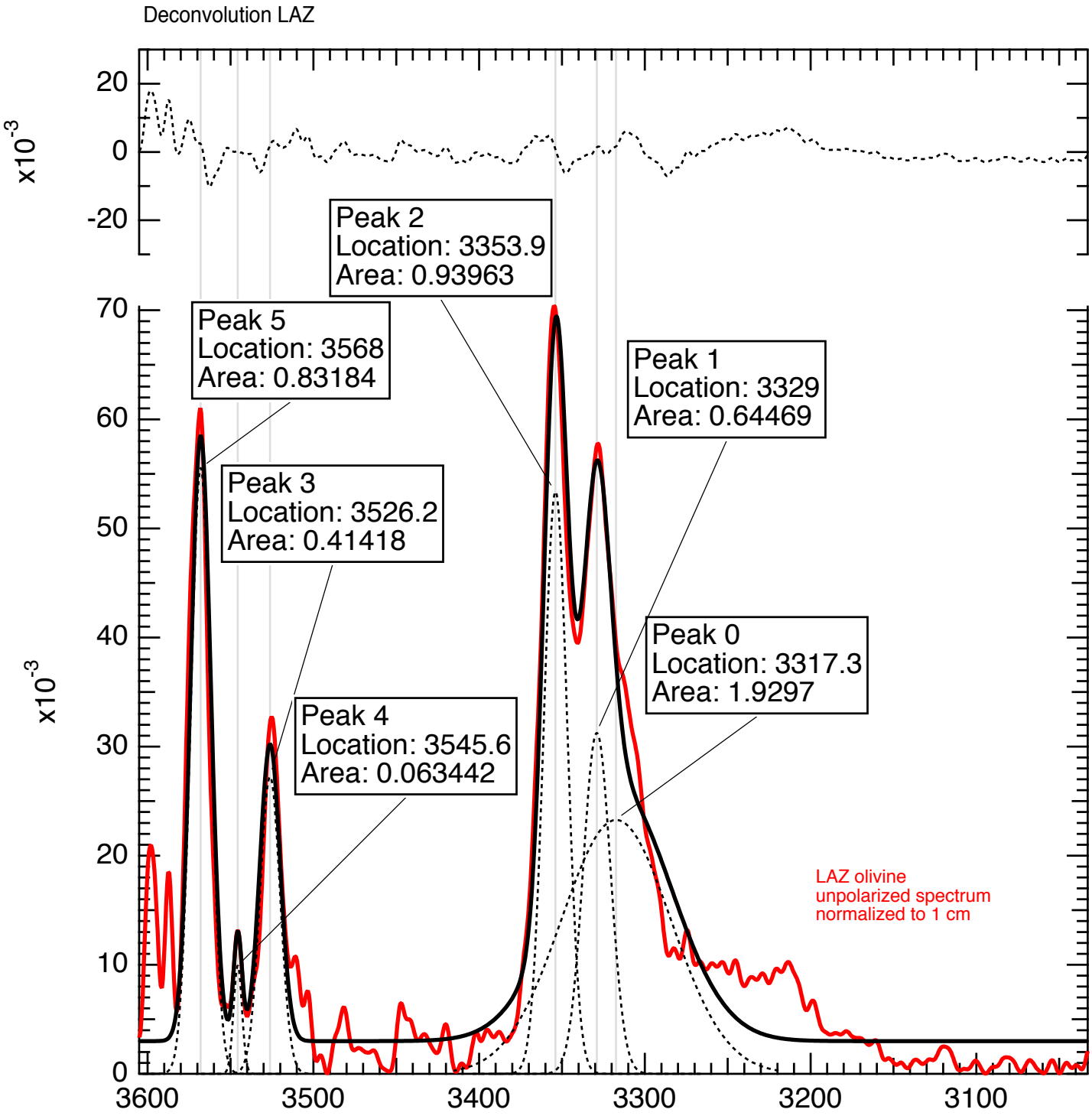
Deconvolution LAZ
x10-3
20
0
-20
Peak 2
Location: 3353.9
Area: 0.93963
Peak 5
Location: 3568
Area: 0.83184
Peak 1
Location: 3329
Area: 0.64469
Peak 3
Location: 3526.2
Area: 0.41418
Peak 0
Location: 3317.3
Area: 1.9297
Peak 4
Location: 3545.6
Area: 0.063442
x10-3
70
60
50
40
30
20
10
0
3600
3500
3400
3300
3200
3100
LAZ olivine
unpolarized spectrum
normalized to 1 cm

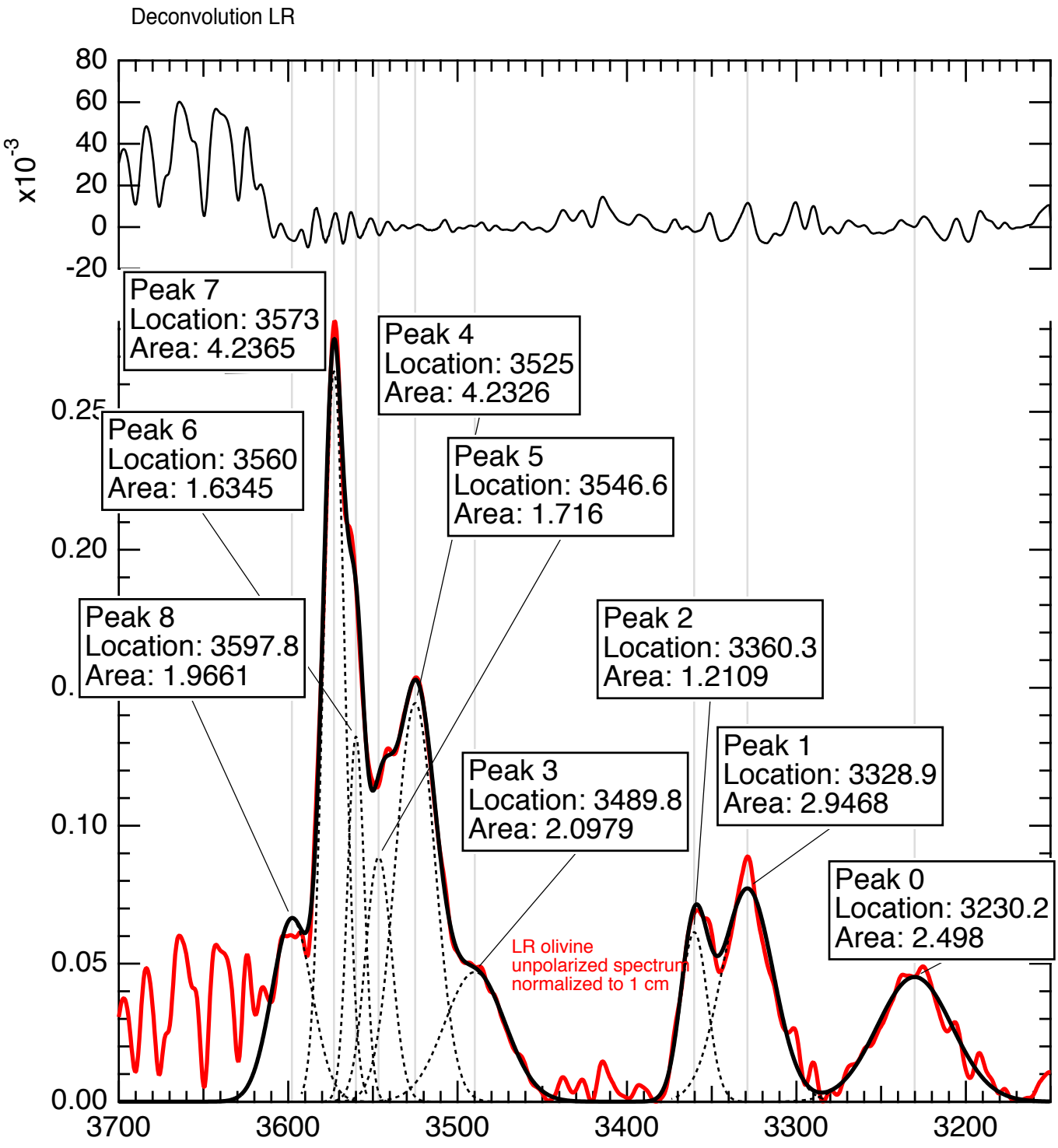
Deconvolution LR
x10-3
80
60
40
20
0
-20
0.25
0.20
0.
0.10
0.05
0.00
3700
3600
3500
3400
3300
3200
Peak 7
Location: 3573
Area: 4.2365
Peak 4
Location: 3525
Area: 4.2326
Peak 6
Location: 3560
Area: 1.6345
Peak 5
Location: 3546.6
Area: 1.716
Peak 8
Location: 3597.8
Area: 1.9661
Peak 2
Location: 3360.3
Area: 1.2109
Peak 1
Location: 3328.9
Area: 2.9468
Peak 3
Location: 3489.8
Area: 2.0979
Peak 0
Location: 3230.2
Area: 2.498
LR olivine
unpolarized spectrum
normalized to 1 cm

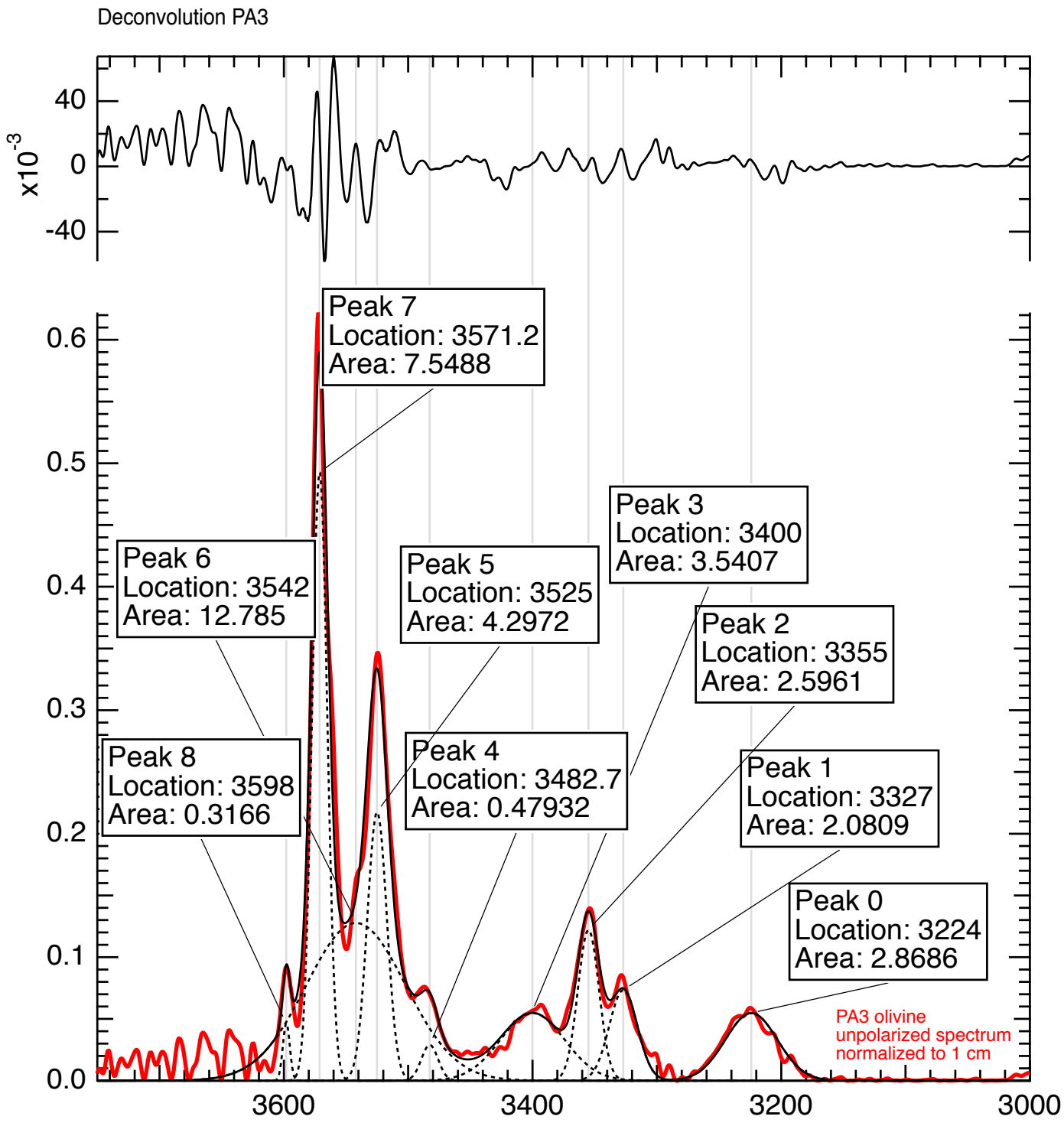
Deconvolution PA3
x10-3
40
0
-40
0.6
0.5
0.4
0.3
0.2
0.1
0.0
3600
3400
3200
3000
Peak 7
Location: 3571.2
Area: 7.5488
Peak 6
Location: 3542
Area: 12.785
Peak 5
Location: 3525
Area: 4.2972
Peak 3
Location: 3400
Area: 3.5407
Peak 2
Location: 3355
Area: 2.5961
Peak 8
Location: 3598
Area: 0.3166
Peak 4
Location: 3482.7
Area: 0.47932
Peak 1
Location: 3327
Area: 2.0809
Peak 0
Location: 3224
Area: 2.8686
PA3 olivine
unpolarized spectrum
normalized to 1 cm

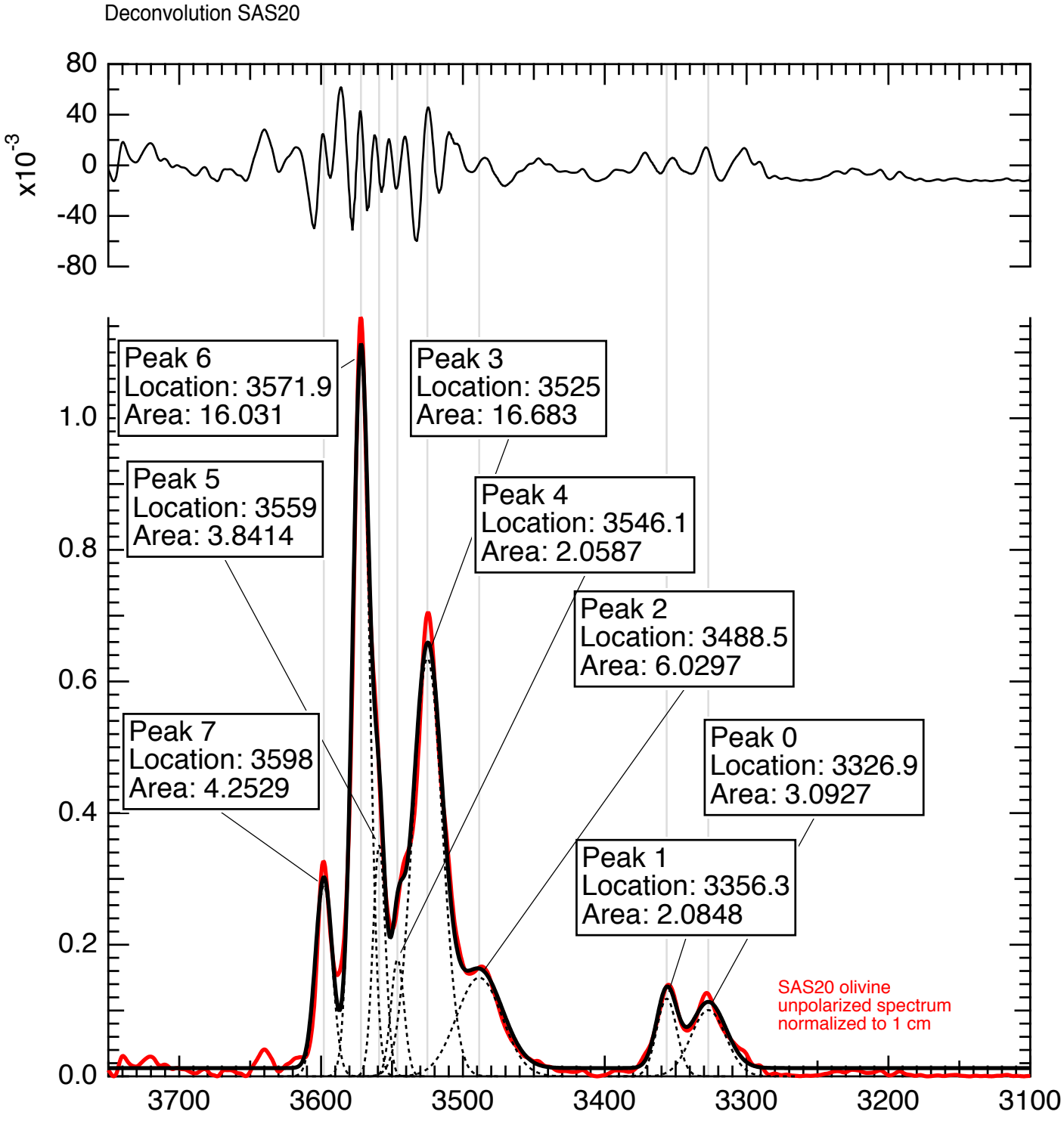
Deconvolution SAS20
80
40
0
-40
-80
x10-3
Peak 6
Location: 3571.9
Area: 16.031
Peak 3
Location: 3525
Area: 16.683
Peak 5
Location: 3559
Area: 3.8414
Peak 4
Location: 3546.1
Area: 2.0587
Peak 2
Location: 3488.5
Area: 6.0297
Peak 7
Location: 3598
Area: 4.2529
Peak 0
Location: 3326.9
Area: 3.0927
Peak 1
Location: 3356.3
Area: 2.0848
SAS20 olivine
unpolarized spectrum
normalized to 1 cm
1.0
0.8
0.6
0.4
0.2
0.0
3700
3600
3500
3400
3300
3200
3100

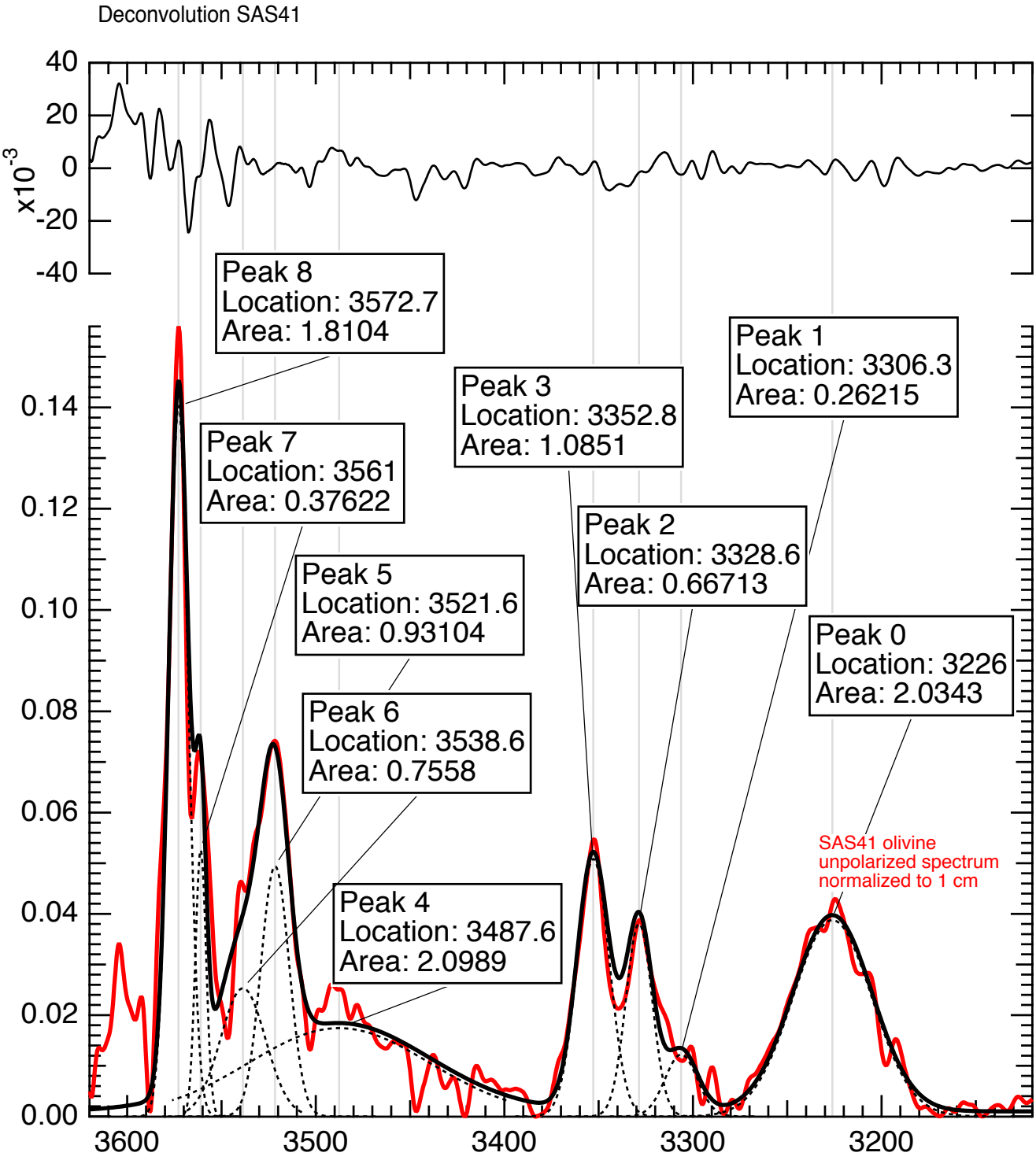
Deconvolution SAS41
40
20
0
-20
-40
x10-3
Peak 8
Location: 3572.7
Area: 1.8104
Peak 7
Location: 3561
Area: 0.37622
Peak 5
Location: 3521.6
Area: 0.93104
Peak 6
Location: 3538.6
Area: 0.7558
Peak 4
Location: 3487.6
Area: 2.0989
Peak 3
Location: 3352.8
Area: 1.0851
Peak 2
Location: 3328.6
Area: 0.66713
Peak 1
Location: 3306.3
Area: 0.26215
Peak 0
Location: 3226
Area: 2.0343
SAS41 olivine
unpolarized spectrum
normalized to 1 cm
0.14
0.12
0.10
0.08
0.06
0.04
0.02
0.00
3600
3500
3400
3300
3200

Fig. S5. Variations of Ni content (at. ppm) as a function of forsterite content (Fo% = 100 × Mg/(Mg+Fe)) in the olivines studied herein and in previous studies: garnet peridotites (Peslier et al., 2010, 2012), spinel-bearing peridotites (O'Reilly et al., 1997; Satsukawa et al., 2017), olivine phenocrysts from Aeolian island arc lavas (Zamboni et al., 2017; *NB*, the field of arc lavas extends down to 200 ppm Ni and Fo% = 60), olivine in various types of troctolites (Basch et al., 2018), and MORBs, OIBs (Hawaii), and Komatiites (Sobolev et al., 2007).

Demouchy and Alard, Fig. S5

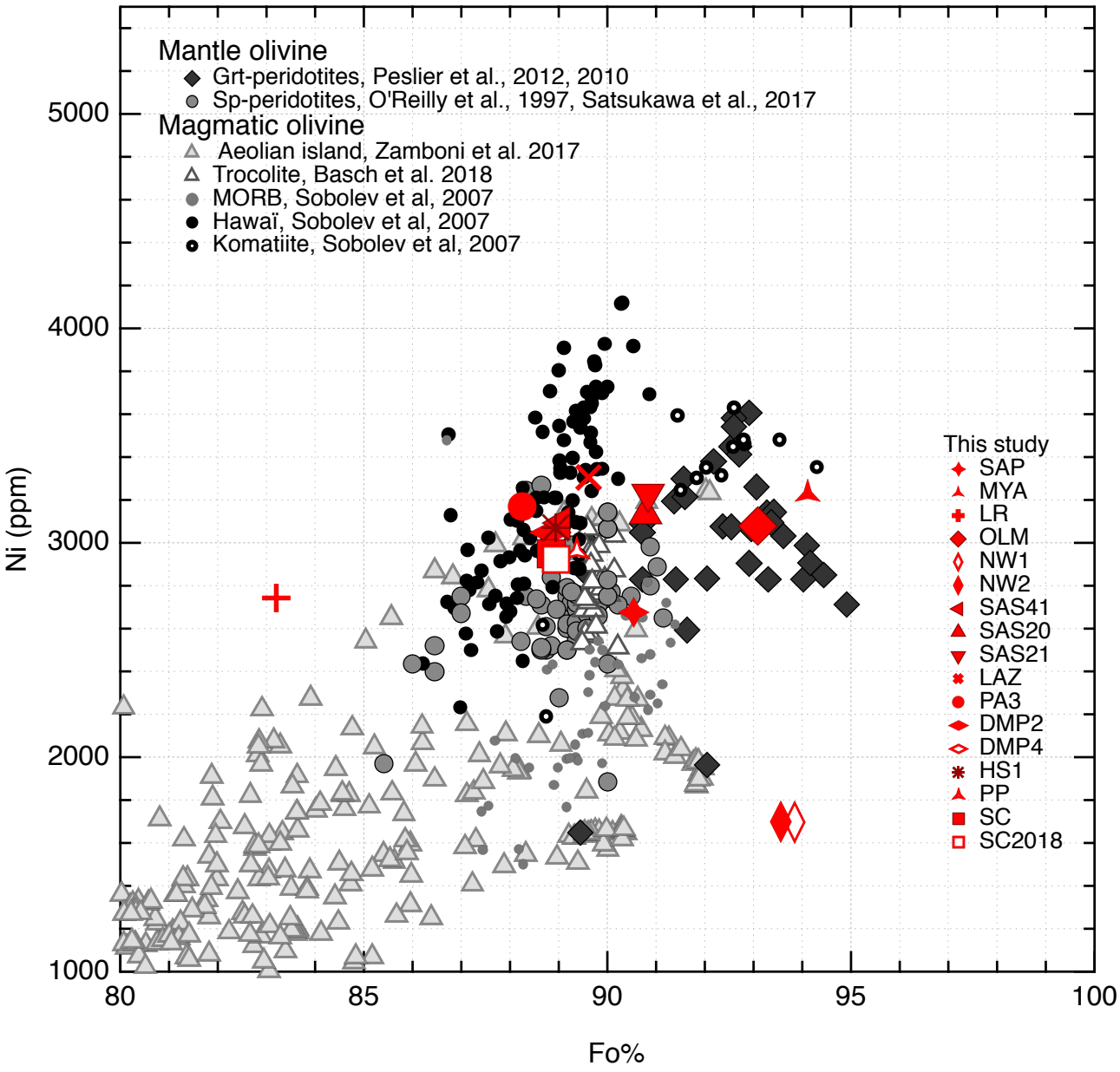

Fig. S6. Selected plots of trace element as a function of trace element concentration in micromole/g (B vs Li; Ti vs Cr/Na; Cr vs B; B vs H).

Demouchy and Alard, Fig. S6

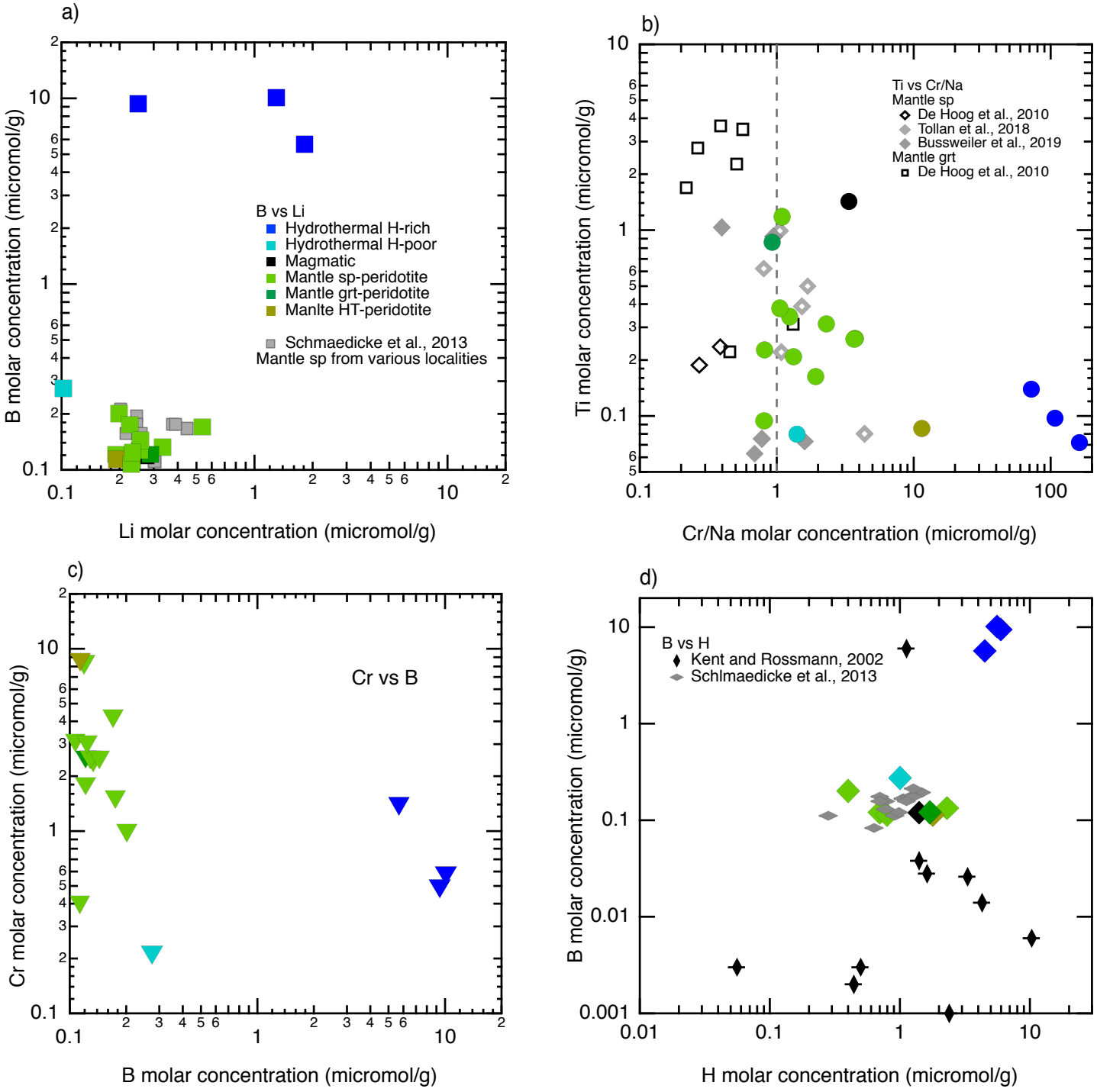

Fig. S7. Selected plots of trace element as a function of trace element concentration in micromole/g (Ti vs V; Cr vs V; Cr vs Al; Li vs B).

Demouchy and Alard, Fig. S7

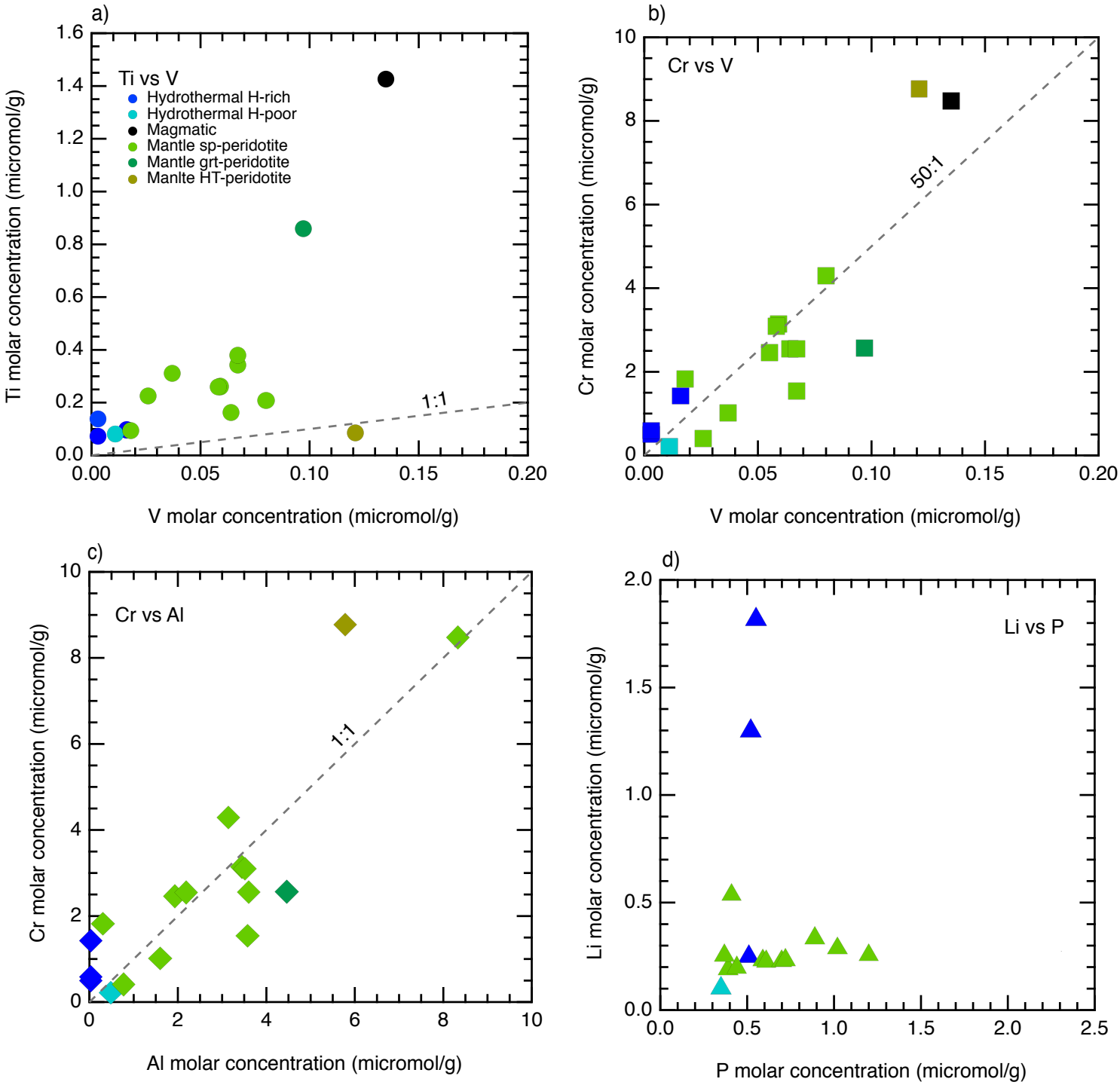

Fig. S8. Sum of mono-, di-, tri-, tetra and penta-valent elements as a function of hydrogen concentration in ppm by weight.

Demouchy and Alard
Fig. S8 Revised

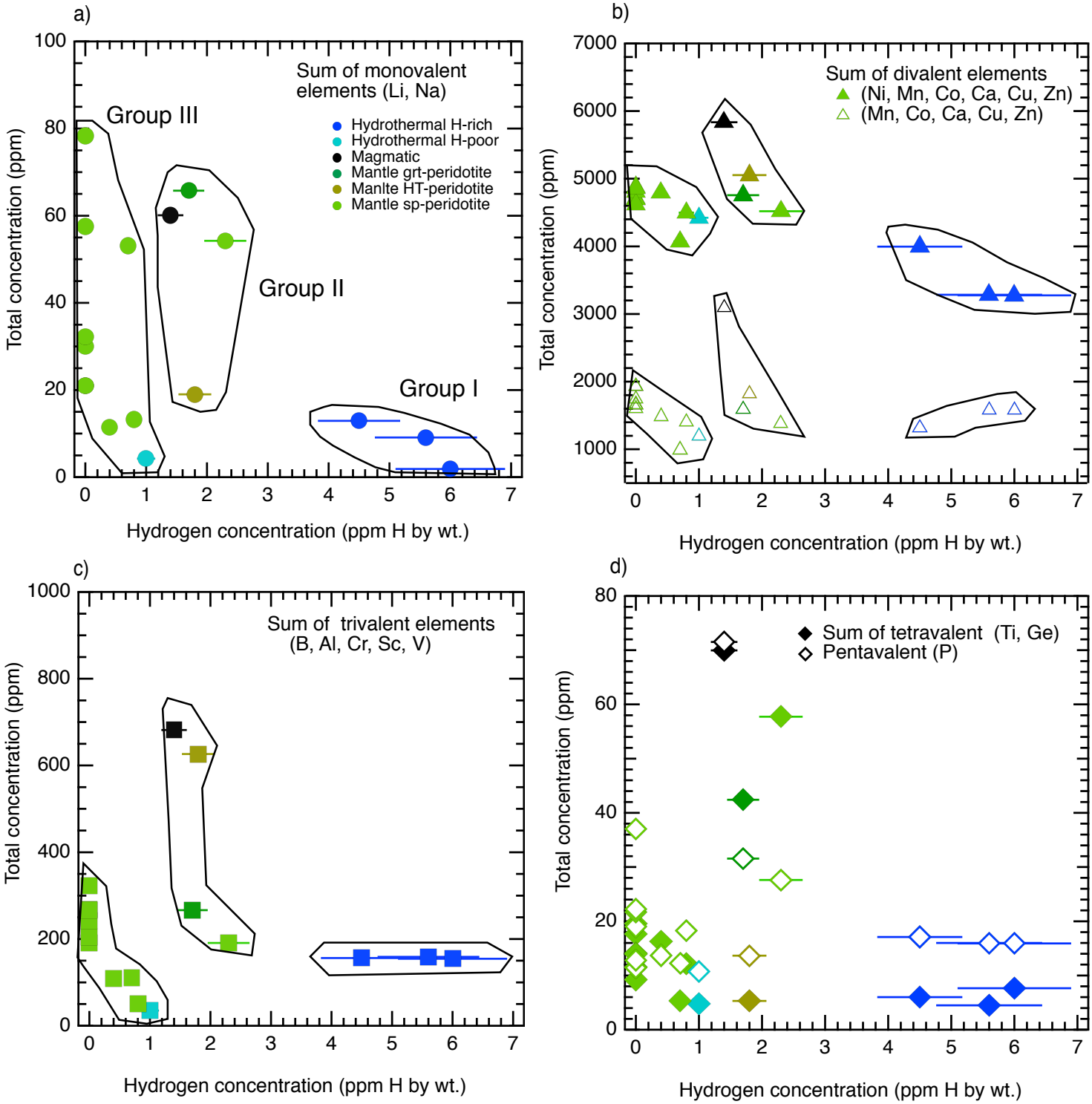

Fig. S9. (a) Sum of trivalent elements vs. sum of the monovalent elements; (b) Sum of trivalent elements vs. sum of the tetravalent elements; (c) Sum of tetravalent elements vs. sum of the monovalent elements; (d) Sum of pentavalent elements vs. sum of the monovalent elements.

Mantle sp

Demouchy and Alard, Fig. S9